UNIVERSIDADE D
COIMBRA

Todor Vuchkov

UPSCALE OF MAGNETRON SPUTTERED TMD BASED THIN FILMS FOR TRIBOLOGICAL APPLICATIONS

Doctoral Thesis in Mechanical Engineering, Surface Engineering, supervised by Professor Doctor Albano Augusto Cavaleiro Rodrigues de Carvalho, submitted to the Department of Mechanical Engineering, Faculty of Sciences and Technology of the University of Coimbra

August of 2020

Faculty of Sciences and Technology
University of Coimbra

Upscale of magnetron sputtered TMD based thin films for tribological applications

Todor Vuchkov

Doctoral Thesis in Mechanical Engineering, Surface Engineering, supervised by Professor Doctor Albano Augusto Cavaleiro Rodrigues de Carvalho, submitted to the Department of Mechanical Engineering, Faculty of Sciences and Technology of the University of Coimbra.

August of 2020

UNIVERSIDADE D
COIMBRA

Acknowledgments

This thesis is a result of a work performed between 2017-2020, work that is a part of the Innovative Traning Network SOLUTION – Solid lubrication for emerging engineering applications.

Firstly, I would like to express my gratitude to my supervisor Professor Albano Caveleiro for giving me the opportunity to perform this work. His advice and support in every aspect were extremely helpful. Moreover, he provided a unique open-minded research environment. I would also like to thank the Adjunct Director/Technical Manager of the Laboratory for Wear Testing and Materials at Instituto Pedro Nunes Eng. João Paulo as well as the Project Coordinator Eng. Ana Manaia, for all the support.

I am grateful to my colleagues: Dr. Ricardo Serra, Dr. João Carlos Oliveira, Dr. Filipe Fernandes, Dr. Nuno Figueiredo at the Surface Engineering Group at CEMMPRE for all the technical help and discussions. Special thanks to Dr. Manuel Evaristo for helping with the operation of the PVD equipment.

I would also like to thank my colleagues: Carlos Patacas, António Fonseca, João Costa, Bruno Martins, Elsa Oliveira, and Dr. Emilio Frutos at the Laboratory for Wear Testing and Materials at IPN for all the technical help and fruitful discussions. Special thanks to my colleague and friend Talha Bin Yaqub for the productive technical discussions.

Thanks to Professor Tomas Polcar for allowing me to perform part of the work at the Czech Technical University in Prague. Thanks to Dr. Kosta Simonovic for the help with the experimental work during my stay at CVUT.

I would like to thank my family for their support.

Finally, my greatest gratitude goes to my wife Emilija who accompanied and fully supported me during this time.

This work received funding from the European Union's Horizon 2020 research and innovation program under grant agreement No. 721642: SOLUTION.

Resumo

O atrito e o desgaste são processos que originam grande consumo de energia representando uma grande fatia da energia consumida a nível mundial. Numa tentativa de reduzir o atrito e o desgaste em contatos mecânicos têm surgido inúmeras soluções, desde lubrificantes líquidos desenvolvidos "à medida" até soluções complexas baseadas em engenharia de superfícies. Entre as muitas soluções de engenharia de superfícies, a utilização de revestimentos produzidos por técnicas de deposição física em fase de vapor (PVD) tem sido uma das melhores opções. A técnica de PVD permite depositar filmes relativamente finos com espessuras na gama de algumas centenas de nanómetros até dezenas de micrómetros. Embora estes revestimentos sejam relativamente finos, conseguem reduzir significativamente o atrito e aumentar o tempo de vida ao desgaste de componentes mecânicos.

Os dicalcogenetos de metais de transição (TMD) com uma estrutura lamelar são compostos com propriedades mecânicas muito anisotrópicas. Por isso, têm uma resistência mecânica ao corte muito reduzida devido às forças de ligação, tipo Van der Waals, existentes entre os planos basais da estrutura hexagonal. Esta propriedade tem sido explorada em termos de tribologia como facilitadora do deslizamento, dando origem a baixo atrito. A principal desvantagem destes compostos é o seu potencial reduzido para lubrificar em condições ambientais normais devido à oxidação e intercalação do vapor de água entre os planos basais. No primeiro processo, são formados óxidos metálicos com muito menor poder lubrificante; no segundo, há um aumento da energia de ligação secundária entre os planos com o consequente aumento da resistência ao corte. Os TMDs têm sido mais usados em componentes em deslizamento em condições extraterrestres, típicas de um meio em vácuo. Outra desvantagem é a sua dureza relativamente baixa e, por isso, a sua baixa capacidade de suportar cargas de contato. Uma solução para estes problemas pode ser providenciada pela deposição de revestimentos com estrutura nanocompósita de maior complexidade. Para tal, tem sido tentada a incorporação de elementos metálicos e não metálicos nos TMDs, tais como Ti, Cr, N, ou C. Uma solução nanocompósita muito promissora tem sido a co-deposição de TMDs com carbono, para formar uma estrutura nanocompósita consistindo de uma matriz de carbono amorfo embebida com cristais de TMD e, eventualmente, grãos de carbonetos dos metais de transição. Esta estrutura nanocompósita tem a capacidade excecional de providenciar baixo atrito e resistência ao desgaste, em condições de utilização muito diversas, tais como ar ambiente, vácuo, N_2 seco e temperaturas elevadas até 300-400 ºC. Historicamente, estes revestimentos nanocompósitos eram na maioria das vezes depositados por pulverização catódica magnetrão em equipamento com câmaras de vácuo de dimensão laboratorial. Houve muito poucas tentativas para utilizar equipamentos (semi)-industriais para depositar revestimentos nanocompósitos com matriz de carbono e cristais de TMDs. O desempenho destes revestimentos é

fortemente afetado pela composição e (micro)estrutura. Como os revestimentos são multicomponente com constituintes que têm massas atómicas diferentes, a modificação na configuração da deposição pode influencias significativamente a composição química e, consequentemente, o desempenho.

O objetivo deste trabalho é o redimensionamento do processo de deposição de revestimentos de dicalcogenetos de metais de transição ligados com carbono para uma escala industrial. Inicialmente, é estudada a deposição de revestimentos W-S-C num equipamento de pulverização catódica laboratorial. Nos capítulos seguintes, é desenvolvida a deposição dos sistemas W-S-C e Mo-Se-C num equipamento de pulverização catódica semi-industrial. Neste estudo é focada a relação entre os vários parâmetros do processo (p.ex. a distância do alvo ao substrato) e as propriedades finais dos revestimentos. A discussão recai sobre a composição química, a cristalinidade, a (micro,nano)estrutura, a ligação química, a dureza, a adesão e o desempenho tribológico. Os métodos de caraterização incluem: SEM/WDS, TEM, XRD, XPS, nanoindentação, espetroscopia Raman, indentação deslizante e testes de deslizamento realizados em condições diferentes de ensaio. Além disso, são utilizados dois programas de software para simulação baseada em métodos de Monte Carlo para compreender melhor os mecanismos de deposição responsáveis pelas variações da composição química.

O estudo sugere que os melhores resultados tribológicos só são alcançados se a composição química for devidamente otimizada. Em primeiro lugar, a razão entre os átomos de calcogeneto e de metal de transição é extremamente importante. Esta razão tem de ser superior a 1,5 para se conseguir um bom desempenho de atrito. Em segundo lugar, deve usar-se um teor em carbono de cerca de 50 % at. para conseguir uma resistência mecânica adequada e, consequentemente, uma boa resistência ao desgaste. Se estas condições forem preenchidas, o coeficiente de atrito, passível de ser atingido com estes revestimentos, situa-se nas gamas de [0.08-0.15], [0.03-0.05] e [0.01-0.05], respetivamente, para testes de deslizamento em ar ambiente, N_2 seco e temperaturas elevadas. As taxas específicas de desgaste têm valores desde 10-7 até 10-6 mm^3/Nm.

Finalmente, são desenvolvidas algumas receitas para implementar os revestimentos à escala industrial de modo a alcançar propriedades tribológicas adequadas em aplicações tendo aços como material antagonista. O conhecimento, ganho no que respeita a relação entre os parâmetros do processo e as propriedades finais, pode ser mais explorado para permitir a produção de um revestimento específico para uma dada aplicação a ser depositado num equipamento de dimensões industriais.

Palavras-Chave: Dicalcogenetos de metais; Implementação industrial; Pulverização catódica; Tribologia;

Abstract

Friction and wear as energy-consuming processes make a significant contribution towards the worldwide energy consumption. The pursue of the reduction in friction and wear leads to various engineering solutions ranging from tailored liquid lubricants to complex surface engineering solutions. Among the significant amount of surface engineering solutions for tribological applications, coatings deposited by various physical vapor deposition (PVD) processes have been one of the best options. PVD allows the deposition of relatively thin coatings with thicknesses ranging from hundreds of nanometers up to tens of micrometers. Although these coatings are relatively thin, they can significantly reduce friction and extend the wear life of the coated components.

Layered hexagonal transition metal dichalcogenides are compounds with highly anisotropic mechanical properties. They possess a very low shear strength due to the weak van der Waals forces acting between the basal planes. This property is exploited in the field of tribology as sliding in the low shear strength direction is easy. The main disadvantage of these compounds is their reduced ability to lubricate in ambient conditions due to oxidation and intercalation of water vapor between the layers. In the first process, less lubricious molybdenum oxides are formed, and the second process results in increased shear strength between the layers. Therefore, TMDs deposited as thin films are often used on components sliding in extraterrestrial conditions, typical of a vacuum environment. Another disadvantage is their relatively low hardness and, thus, their low load-bearing capacity. A solution to these issues can be provided by depositing more complex nanocomposite coatings. This can be achieved by the incorporation in TMDs of various metallic or non-metallic elements like Ti, Cr, N, or C. A very promising nanocomposite solution has been achieved by co-deposition of carbon and TMDs, during which a nanocomposite structure consisting of an amorphous carbon matrix with crystallites of TMDs, as well as transition metal carbides, can be achieved. An optimized nanocomposite coating consisting of amorphous carbon and TMDs has the exceptionable ability to provide friction and wear reduction in various operating conditions like ambient air, vacuum, dry N_2, and elevated temperatures up to 300-400°C.

Historically, these nanocomposite coatings were most often deposited by magnetron sputtering in laboratory-scale vacuum chambers. There are very rare examples of attempts to use bigger (semi)-industrial units to deposit nanocomposite coatings consisting of carbon and TMDs. The performance of the coatings is strongly affected by the composition and their microstructure. As the coatings are multicomponent with constituents having different atomic mass, the change in the deposition configuration will strongly affect the composition, and thus the performance.

In this work upscaling of the deposition process for carbon alloyed TMD coatings is presented. Firstly, the deposition of W-S-C coatings in a laboratory-scale sputtering equipment, following various routes, is studied. In the following chapters, the deposition of W-S-C and Mo-Se-C coatings in semi-industrial sputtering apparatus is developed. The emphasis is put on the relationship between various processing parameters (e.g. the target-to-substrate distance) and the properties of the coatings. The chemical composition, crystallinity, micro(nano)structure, chemical bonding, hardness, adhesion, and the tribological properties are discussed. The experimental characterization methods include: SEM/WDS, TEM, XRD, XPS, nanoindentation, Raman spectroscopy, scratch testing, and tribological testing under various conditions. Furthermore, two Monte-Carlo based simulation software packages were used to better understand the mechanisms responsible for the compositional variations.

The study suggests that the best tribological results are only achieved if the chemical composition is fully optimized. Firstly, the ratio between the chalcogen atoms and transition metal atoms is found to be extremely important. This ratio has to be over 1.5 to achieve a good friction performance. Secondly, to reach a suitable mechanical strength and, then, a good wear resistance, a carbon content of ~ 50 at. % should be used. If these conditions are fulfilled, the coefficient of friction achieved for the coatings is in the ranges [0.08-0.15], [0.03-0.05], and [0.01-0.05] during sliding in standard ambient air, dry N_2, and elevated temperature conditions, respectively. The specific wear rates are in the range of 10^{-7}-10^{-6} mm^3/Nm.

Finally, a couple of recipes for industrial implementation, yielding good tribological properties against steel-based counterparts, are developed. The knowledge gained regarding the relationship between the processing parameters and the properties can further be exploited for the deposition of coatings tailored for a specific application to be deposited in a large-scale industrial equipment.

Keywords: Magnetron sputtering; Tribology; Metal dichalcogenides; Industrial implementation

List of Publications

The work of this thesis resulted in 4 papers published in peer-reviewed journals.

1. Vuchkov, T.; Yaqub, T.B.; Evaristo, M.; Cavaleiro, A. Synthesis, Microstructural, and Mechano-Tribological Properties of Self-Lubricating W-S-C(H) Thin Films Deposited by Different RF Magnetron Sputtering Procedures. *Coatings* **2020**, *10*, 272.
2. T. Vuchkov, M. Evaristo, T. Bin Yaqub, T. Polcar, A. Cavaleiro, Synthesis, microstructure and mechanical properties of W–S–C self-lubricant thin films deposited by magnetron sputtering, Tribol. Int. 150 (2020) 106363. doi:10.1016/j.triboint.2020.106363
3. T. Vuchkov, M. Evaristo, T. Bin Yaqub, A. Cavaleiro, The effect of substrate location on the composition, microstructure and mechano-tribological properties of W-S-C coatings deposited by magnetron sputtering, Surf. Coatings Technol. 386 (2020) 125481. doi:10.1016/j.surfcoat.2020.125481
4. T. Vuchkov, T. Bin Yaqub, M. Evaristo, A. Cavaleiro, Synthesis, microstructural and mechanical properties of self-lubricating Mo-Se-C coatings deposited by closed-field unbalanced magnetron sputtering, Surf. Coatings Technol. 394 (2020) 125889. doi:https://doi.org/10.1016/j.surfcoat.2020.125889

Other papers published in peer-reviewed journals in which the author contributed are listed below:

1. H. Torres, T. Vuchkov, M. Rodríguez Ripoll, B. Prakash, Tribological behaviour of MoS2-based self-lubricating laser cladding for use in high temperature applications, Tribol. Int. 126 (2018) 153–165. doi:10.1016/J.TRIBOINT.2018.05.015.
2. H. Torres, T. Vuchkov, S. Slawik, C. Gachot, B. Prakash, M. Rodríguez Ripoll, Self-lubricating laser claddings for reducing friction and wear from room temperature to 600 °C, Wear. 408–409 (2018). doi:10.1016/j.wear.2018.05.001.
3. T. Bin Yaqub, T. Vuchkov, M. Evaristo, A. Cavaleiro, DCMS Mo-Se-C solid lubricant coatings – Synthesis, structural, mechanical and tribological property investigation, Surf. Coatings Technol. (2019) 124992. doi:10.1016/j.surfcoat.2019.124992.
4. T. Bin Yaqub, T. Vuchkov, P. Sanguino, T. Polcar, A. Cavaleiro, Comparative Study of DC and RF Sputtered MoSe2 Coatings Containing Carbon—An Approach to Optimize Stoichiometry,

Microstructure, Crystallinity and Hardness, Coatings. 10 (2020) 133. doi:10.3390/coatings10020133.

5. M. Shamshiri, A. Manaia, T. Vuchkov, A. Carvalho, G. Gaspar, A. Fernandes, S.H. Dolatabadi, F. Costa, A. Cavaleiro, Influence of laser structural patterning on the tribological performance of C-alloyed W-S coatings, Surf. Coatings Technol. 394 (2020) 125822. doi:10.1016/j.surfcoat.2020.125822.
6. T. Bin Yaqub, K. Hebbar Kannur, T. Vuchkov, C. Pupier, C. Héau, A. Cavaleiro, Molybdenum diselenide coatings as universal dry lubricants for terrestrial and aerospace applications, Mater. Lett. 275 (2020) 128035. doi:10.1016/j.matlet.2020.12803

List of conference presentations:

1. T.Vuchkov, M.Evaristo, T.B Yaqub, A.Cavaleiro, T Polcar, "Synthesis, mechanical properties, and tribological response in diverse testing environments of a W-S-C self-adaptive thin film deposited by CFUBMS", 7th European Conference on Tribology, Wien, Austria, June 12-14th. URL: https://ecotrib2019.oetg.at/startpage
2. T. Vuchkov, M. Evaristo, T.B Yaqub, A.Cavaleiro, T Polcar, "Tribological Behaviour in diverse testing environments of a self-lubricating W-S-C coating deposited by CFUBMS", accepted for presantation at the 46th Leeds-Lyon Symposium on Tribology, Lyon, France, September 2nd-4th, URL: https://leeds-lyon2019.sciencesconf.org/

List of Abbreviations

AFM	Atomic force microscopy
AISI	American Iron and Steel Institute
CFUBMS	Closed-field unbalanced magnetron sputtering
CH_4	Methane
COF	Coefficient of friction
CVD	Chemical vapour deposition
CVUT	Czech Technical University in Prague
DC	Direct current
DCMS	Direct current magnetron sputtering
DIN	Deutsches Institut für Normung, German Institute for Standardization
DLC	Diamond-like carbon
EDS	Energy dispersive spectroscopy
FESEM	Field emission scanning electron microscope
GIXRD	Grazing incidence X-ray diffraction
HIPIMS	High impulse power magnetron sputtering
ISO	International Organization for Standardization
NA	Numerical aperture
p-DC	Pulsed direct current
PTFE	Polytetrafluoroethylene
PVD	Physical vapour deposition
RF	Radio frequency
RH	Relative humidity
RT	Room temperature
SEG-CEMMPRE	Surface Engineering Group - Centre for Mechanical Engineering, Materials and Processes
SIMTRA	Simulation of metal transport
SRIM	Surface and range of ions in matter

SRV™	Schwingung Reibung Verschleiβ, german for reciprocating friction, and wear
TEM	Transmission electron microscopy
TMDs	Transition Metal Dichalcogenides
TSD	Target-to-substrate distance
UHMWPE	Ultra-high molecular weight polyethylene
WDS	Wavelength dispersive spectroscopy
XPS	X-ray photoelectron spectroscopy
YSZ	Yttria-stabilized zirconia

List of Symbols

A_c	Real area of contact	[m^2]
d	Scar diameter	[m]
E	Elastic modulus	[Pa]
E	Energy	[eV]
E_i	Incident energy	[eV]
E_{sb}	Surface binding energy	[eV]
E_t	Transferred energy	[eV]
F_f	Friction force	[N]
F_n	Normal force	[N]
H	Hardness	[Pa]
h	Height of spherical cap	[m]
k_b	Boltzmann constant	[$eV \cdot K^{-1}$]
Mi	Mass of the incident atom	[kg]
M_t	Mass of the target atom	[kg]
n_g	Gas density	[$kg \cdot m^{-3}$]
p	Pressure	[Pa]
r	Atomic radius	[m]
R_a	Arithmetical mean value of a roughness profile	[m]
r_b	Radius of ball	[m]
S	Shear strength	[Pa]
s	Sliding distance	[m]
S_a	Arithmetical mean value of the surface roughness	[m]
T	Temperature	[K]
V_w	Wear volume	[m^3]
W_r	Specific wear rate	[$mm^3 \cdot N^{-1} \cdot m^{-1}$]
η	Incident angle	[°]

λ	Mean free path	[m]
σ	Collision cross section	[m^2]

Table of Contents

List of Figures

List of Tables

Chapter 1 Introduction

Controlling friction and reducing wear is an ongoing challenge which is a subject of research for many institutions worldwide. According to one of the most recent studies on global energy, ~23 % of the total energy consumption originates from tribological contacts, of which 20% is used to overcome friction and 3% to remanufacture worn parts [1]. The most widely used methods for improving the tribological performance of mechanical components are based on surface engineering. The deposition of thin films (coatings) by gaseous state processes like physical vapor deposition (PVD) and chemical vapor deposition (CVD) has often been used for improving the tribological behavior. Some of the coatings providing improved tribological performance are of polymeric type like PTFE [2] and UHMWPE [3], Diamond-Like-Carbon (DLC) [4] and those based on transition metal dichalcogenides (TMD) like WS_2 [5] and MoS_2 [6]. Thin films based on TMD are often studied because of the lubricity they can provide, but there are not many reports of their widespread usage mostly because of the deterioration of their properties when operated in a normal humid atmosphere.

DLC coatings, as an example, are very often used for tribological applications, mainly encouraged by the reduction of friction, improvement of the wear resistance, high hardness and chemical inertness [7]. Traditional carbon-based coatings (e.g. metal-doped DLC) reduce the friction and wear through the formation of lubricious graphite-rich layers. One of the drawbacks of the graphitic layers is their reduced lubricity in dry environments (e.g. dry N_2 or vacuum), since an intercalating agent (e.g. water vapor or hydrogen) is needed for lubrication [8]. This issue can be surmounted by adding significant amounts of hydrogen to the films, but issues regarding hydrogen depletion might arise [9]. The TMDs, on the other hand, show superior performance in dry environments, and their usage in combination with carbon, for the synthesis of thin films, can significantly improve the tribological performance in diverse operating environments.

This work was mainly performed at the surface engineering group (SEG) in the Centre for Mechanical Engineering Materials and Processes (CEMMPRE) of the University of Coimbra as well as the Laboratory for Wear, Testing and Materials (Led&Mat) at Instituto Pedro Nunes. The development of thin films consisting of TMDs and carbon had been performed in the last 15 years at both units simultaneously with the resulting films showing promising properties. In the framework of the thin-film development in the

research groups, this work aims at upscaling the process, which was performed in small deposition units, in order to allow coating large mechanical components.

The thesis is based on 4 research works undertaken towards the upscaling of the deposition process, works that resulted in 4 scientific papers, published in journals in the field of surface engineering and tribology. Apart from the Introduction chapter, the work is organized in 7 additional chapters. In the 2nd chapter, a state of the art review will be presented followed by the presentation of the research gaps and, subsequently, the outlining of the main objectives of the thesis. The 3rd chapter aims at presenting the experimental methods used towards fulfilling the objectives of the thesis. The preparation of the studied coatings, as well as the characterization methods, will be presented.

The work presented in Chapter 4 is aimed at comparing different routes for the deposition of the TMD-C coatings in the laboratory-scale environment. The results obtained are used as a reference for choosing an appropriate deposition method for the semi-industrial scale deposition of the coatings.

Chapter 5 presents the initial attempt of upscaling the deposition process. W-S-C coatings are deposited by closed-field unbalanced magnetron sputtering. The objective is to establish the relationship between the process parameters and the properties of the coatings. Furthermore, a single coating with promising composition, morphology, and microstructure is studied tribologically under various testing conditions.

In Chapter 6 the properties of W-S-C coatings deposited on substrates placed at different locations in the deposition chamber are studied. The selected locations are mimicking the surfaces of big components. A recipe yielding optimal carbon content was programmed based on the work undertaken in Chapter 5. The coatings were studied in terms of chemical composition, microstructure, and morphology. The mechano-tribological properties, the hardness, adhesion, and tribological response in ambient air, dry N_2 and elevated temperature of 200°C, are studied.

In Chapter 7, molybdenum diselenide ($MoSe_2$) is used as a TMD phase instead of the previously used tungsten disulfide (WS_2). The carbon-alloyed coatings were deposited in the same equipment as the one used in Chapters 5 and 6. The properties were studied similarly to the W-S-C ones. The work demonstrates the advantages of the usage of $MoSe_2$ as a TMD phase in terms of coating synthesis. Furthermore, the tribological properties are studied and compared with the ones obtained for the W-S-C coatings.

Chapter 2 Historical background and state of the art

In this chapter, a historical background regarding the developments related to the field of tribology and the field of surface engineering will be presented. The process used for the synthesis of the coatings in the thesis will be explained more in detail. Additionally, the important findings regarding the tribological properties of sputtered coatings containing TMDs will be presented.

2.1 Tribology

Tribology is a word originating from the Greek word “tribos” which means rubbing and refers to the study of friction, wear, lubrication, and the design of bearings, the science of interacting surfaces in relative motion [10,11]. Tribology is a relatively new science, with the term origination from the United Kingdom’s Lubrication Engineering Working Group report from 1966 led by Peter Jost, a report which is well known as the “Jost Report”. The report was focused on the enormous loss caused by various tribological processes, in the UK industry, and the potential savings if the tribological problems were solved [12]. Friction as a phenomenon had been identified as early as the stone age when man-made bearings were used for stone potter’s wheels. Early scientific studies of friction were done by Leonardo da Vinci in the late fifteenth century, who studied friction forces on horizontal and inclined surfaces. His major conclusions were that friction force is proportional to the applied load and that the friction is not a function of the apparent contact area [11]. These relationships were rediscovered and published by the French inventor Amonton in 1699. Amonton formulated four laws of friction in his memoir. First, the resistance caused by friction increases/decreases in proportion to the pressure. Secondly, the resistance caused by friction is the same for iron, copper, lead, and wood as long as they are lubricated with grease. Thirdly, this resistance is roughly equal to one-third of pressure. Fourth, this resistance does not depend on the velocity and other conditions [13]. It should be noted that the last law is a very rough approximation as it is well known that, for example, in lubricated contacts, the sliding velocity can have a significant effect on the coefficient of friction.

Another discovery that is significant for the advancement of the field of tribology, especially in solid lubrication, is the Bowden and Tabor model on metallic friction, model developed during the 1950s [14]. The authors considered the interaction between the asperities of the solid bodies. The friction force (F_f) arising from the asperity-to-asperity interaction can be calculated using Eq. 1,

$$F_f = A_c \cdot S + F_p \quad (1)$$

where A_c is the contact area, S is the shear strength and F_p is the plowing force. According to this model to have low friction forces the real contact area should be as small as possible, while also having low shear strength of the asperities. This can be achieved by having a hard substrate which will govern the real area of contact and a thin easy to shear film on top of it to control the shear strength. By having a thin soft film, the plowing effect can also be ignored.

A term widely used when talking about tribology is tribosystem. Tribosystem refers to any system that contains one or more triboelements, including all mechanical, chemical and environmental factors relevant to the tribological behavior [15]. A triboelement refers to one of two or more solid bodies comprising a sliding, rolling or abrasive contact, or a body subjected to impingement [15].

Wear, as a tribological process refers to the damage to a solid surface, generally involving the progressive loss of material, due to the relative motion between the surface and a contacting substance or substances [16]. Among different wear mechanisms classifications, the DIN 50320 standard establishes four types [17]:

- Adhesive wear which is caused by the formation of interfacial adhesions ("weld") junctions by the action of molecular forces;
- Abrasive wear, grooving by a scratching action or a micro-cutting process;
- Surface fatigue, a process related to cracking at the surface due to stresses or strains varying in magnitude or direction;
- Tribochemical reaction, the formation of reaction products by a combined effect of the tribological action between the base material and the counter material and a chemical reaction with the surrounding medium

Another notable classification of wear mechanisms was done by Kato [18], who proposed differentiation between mechanical, chemical, and thermal types of wear. In this classification, mechanical wear is related to processes like deformation and fracturing. Chemical wear is correlated with the growth of chemical reaction films, and the thermal type of wear is due to localized surface melting caused by frictional heating.

Finally, it should be noted that friction and wear are not intrinsic materials properties but a system response which is a function of different variables, such as the mechanical properties of materials, environment, intermediate material, surface roughness, velocity, and temperature.

2.2 Surface Engineering

The technological advancement in various scientific fields and industrialized societies leads to an increased need for the reduction and control of friction and wear. In an attempt to tackle these issues, different approaches are being done, such as the improvement of the bulk materials or the incorporation and tailoring of the properties of lubricants. A more sophisticated and modern method for controlling the tribological properties is by changing the surface properties. This method is a result of the fact that most of the tribological processes, and especially failures related to wear, fatigue, or corrosion, are occurring at the surfaces of the materials. Other properties, like the magnetic, thermal, optical, and electrical, are also greatly influenced by the surface and further surface engineering-related studies are also encouraged.

The rapid growth of the field took place during the 1980s [19]. Bell [20] defined the surface engineering as a discipline involving the application of traditional and innovative surface technologies to engineering components and materials in order to produce composite materials with properties unattainable in either the

base or the surface material. In this field, it is important to distinguish between surface modification processes and surface-coating processes [12]. Surface modification processes are those applied directly to the bulk material altering their surface properties. These processes can further be classified into mechanical, thermal, or chemical. The surface-coating processes involve the deposition of new materials on to the surface, in the form of a single layer, composite, gradient, or multilayered arrangement. In some applications, both processes are used in synergy to achieve superior properties as, for example, the nitrided piston rings which are further coated with a CrN layer [21]. Many examples where coatings are applied can be found in the manufacturing industries, where hard coatings, like TiC, TiN, CrN, Ti-Al-N and Al_2O_3, are often used [22]. DLC (diamond-like carbon) coatings are another family of coatings that have been increasingly used for various applications ranging from magnetic storage devices [23] to automotive components [7].

Design considerations related to coatings intended for tribological applications have been identified by Holmberg and Matthews [24] as follows:

1. The friction coefficient should neither exceed a certain value during running-in, while being in the steady-state regime, nor during friction instabilities.
2. The coating and the counterbody wear should not exceed a certain design value;
3. The lifetime of the system must be longer than the required, within a specified probability.

When a coated system is considered, four different zones can be identified as depicted in Figure 2-1 which, by one reason or the other, can influence the global tribological behaviour of the system. Starting by the coating itself, to achieve an improved tribological response, a specific combination of properties must exist. Achieving low friction can be done by having a low shear strength phase on the sliding interface while having a harder phase with a good load-bearing capacity beneath it. Many times, such a requirement can be achieved by developing composite materials. Having a chemically inert surface can be achieved usually with specific elements, which often do not possess low shear strength. The interface between the substrate and the coatings should have a high shear strength and good bonding. This is usually achieved by the usage of substrate compatible interlayers and gradient layers. The substrate should also be hard enough to support the load imposed on the coating. The biggest challenge in the field of the design of the coating for tribological applications is the fact that improving some properties can deteriorate others, an example being hard materials that lack fracture toughness or chemically inert materials that do not possess low shear strength. The final design is usually a compromise between various properties of the different zones of the system.

In the next section, a coating process classification will be presented, and the further focus of the section will be on the PVD processes relevant to the thesis work.

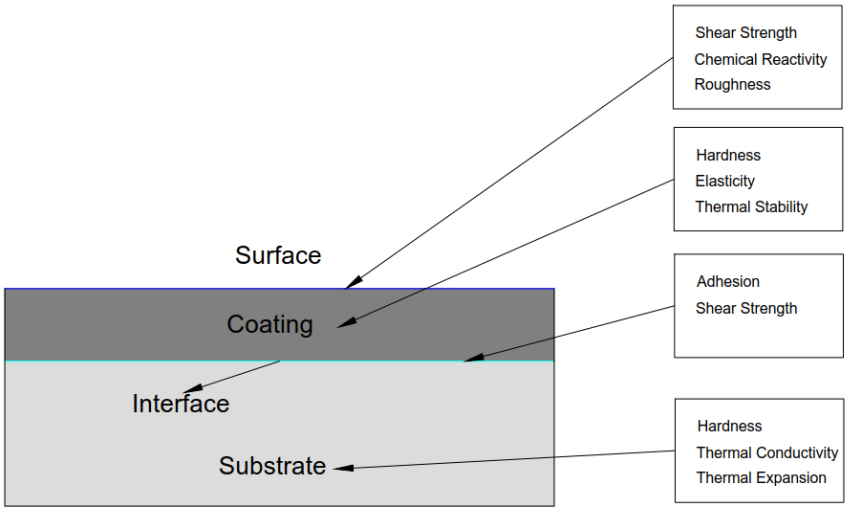

Figure 2-1 Four zones of a coated material and the properties important for the tribological performance

2.3 Surface coatings deposition processes

The need for enhancement of the surface properties by the deposition of coatings results in a wide variety of deposition processes. The motivation behind the development of various processes is the need for improving the coating properties (wear resistance, corrosion resistance, friction reduction), reducing the process costs, overcoming the problems associated with the geometry and the usage of specific materials. A classification of the surface coating processes has been done by Rickerby and Matthews [24,25]. This classification is based on the underlying mechanisms for the coating formation. The processes are divided into four categories: solid-state processes, (semi-) molten state processes, gaseous state processes, and solution-based processes. Solid-state processes include explosive welding, cold-gas dynamic spraying and friction surfacing [26]. Friction surfacing as a method is still widely used for coating deposition. Molten (liquid) state processes include traditional welding procedures with which a wear-resistant hardfacing can be deposited. Another important technique is thermal spraying which can further be divided into arc, flame, plasma spraying. The latest development of the molten state deposition processes is the usage of powerful lasers for the deposition of laser claddings. Solution-based techniques cover electrodeposition and electroless deposition. Since the process used for the deposition of coatings in the present work is a gaseous state one, the gaseous state processes will be presented with more details. Gaseous state processes involve two groups: physical vapor deposition (PVD) and chemical vapor deposition (CVD). Chemical vapor deposition is a process in which the material to be coated is placed in a gaseous phase containing reactive species. Then, a chemical reaction can occur in the gaseous phase and/or over the substrate and the coating

is formed. For the chemical reaction to occur activation energy is needed. Depending on the energy, CVD can further be classified into thermal, plasma, and photon-activated CVD. The development of differently activated processes is mainly focused on reducing the temperature of the process, allowing the deposition of coatings on thermally sensible substrate materials. For example, plasma-assisted CVD can be operated at temperatures of 400-600°C compared to the much higher temperatures (800-1200°C) used for thermally activated CVD [27].

PVD, the other gaseous state deposition process, is different since the deposited material is achieved in the gaseous phase from a solid source. The main advantage of the PVD processes over CVD is the much lower operating temperatures (100-600 °C), which allows that even plastics can be coated. The gaseous depositing species can be achieved by different methods and this is the basis for further classification of the PVD processes into thermally evaporated (evaporation) and sputtering. Evaporation is a process in which the coating material is vaporized by utilizing resistive heating, inductive heating, electric arc, electron beam, or a laser beam. Sputtering, also known as cathodic sputtering, is a frequently used process for deposition of coatings due to the following reasons: [28]:

- Possibility to deposit materials with extremely high melting points;
- The target remains relatively cold during the deposition since the process is collision-based;
- Reactive gases can be introduced to deposit compound films;
- Substrates can be sputter cleaned before coating, a step that can improve the adhesion.

In the next section, the sputtering processes with emphasis on magnetron sputtering and the major discoveries related to it will be explained in detail.

2.4 Magnetron sputtering

The early developments of sputtering as a PVD process for the deposition of thin films can be traced back to the mid-1800s. Crucial for the development of the sputtering processes is the advancements in vacuum technology and electrical power in the 1600s and 1700s [29]. The first publication related to sputtering was published in 1852 by the Welsh physicist Sir William Grove [30]. In his experiments, he obtained a vacuum using a mechanical piston pump. Power was supplied by a nitric acid battery connected to an induction coil. The electrodes located in the glass vacuum chamber were a silver-plated copper plate and a steel needle with a distance between them of around 0.25 cm. The gas used was a mixture of hydrogen and air. When connecting the steel needle to the negative terminal a dark circular stain was observed on the silver-plated substrate with yellow, orange, and blue tints. When switching the polarity between the cathodes he observed the stain from the silver plate was removed leaving a dark polished spot on the plate which was considered to be caused by “molecular disintegration”. While having the steel needle connected to the negative terminal

the author probably deposited an iron oxide layer on the silver plate, switching the polarity resulted in the removal of the oxide layer by sputtering and further sputter etching of the silver-plated substrate. Sputtering as a term was not used in this paper, and the author referred to the process as “molecular disintegration”. Another significant discovery was observed by Gassiot [31]. The author made observations on discharges contained in glass tubes evacuated by mechanical piston pumps and observed black deposits on the side of the tubes near the negative platinum wire terminal. The manipulation of the discharge using a magnetic field is also reported by the author. The early applications of sputtering for thin film deposition were for optical coatings. Wright in 1877 [32] deposited noble metal thin films on flat glass. The thicknesses of the films were estimated by measuring the weight gain after sputtering. Early successful application of the sputtering process was also reported in a paper from 1932 [33]. The process of the deposition of gold films on membranes for microphones was explained in this publication. Compared to previously used electrodeposition processes, the sputtered films had a better lifetime as they did not develop blisters and other surface defects.

The mechanisms behind sputtering were initially not well understood. Firstly it had been considered that the deposition process was a result of local evaporation of the cathode [34], a theory that existed almost 100 years after the first sputtering publication by Groves. Some authors hypothesized that atoms were sputter ejected as a result of the positive-ion bombardment of the cathode [35]. A significant leap towards a better understanding of the sputtering mechanisms was provided through the experiments done by Wehner [36]. Wehner’s experimental work consisted of the sputtering of single-crystal Ag surfaces using Hg ions. The author observed that atoms were ejected along the close-packed crystalline directions, a phenomenon that could not be related to evaporation. The sputtering process was considered to occur in 3 steps. Firstly, the incident ion collides with a surface atom and transfers its momentum and kinetic energy. The second part consists of transport of energy and momentum within the target (collision cascades), the reversal of the vector of momentum towards the outside of the target is needed for sputtering to proceed. In the final step, a surface atom is “knocked-out” of the target when the atom receives energy higher than its binding energy and is not obstructed by adjacent atoms.

Early observations on glow discharges led to the discovery of the emission of secondary electrons emission from the cathode. Goldstein [35] referred to the particles as “cathode rays” and he proved that the particles have a charge opposite to the positive ions “termed as canal rays”. Further studies on cathode rays were done by J.J Thompson [37] who further confirmed that the particles are negatively charged and did experiments on the deflection of the cathode rays by electrostatic and magnetic fields. The secondary electron emission in glow discharges was the reason for the usage of magnets to support the glow discharge during sputtering. The usage of magnets during sputtering was reported by Penning [38], a cylindrical post

was used as a cathode which was surrounded by a cylindrical anode. Both electrodes were surrounded by magnetic coils which generated a magnetic field parallel to the cathode and perpendicular to the electric field. The secondary electrons emitted during sputtering deflected by the magnetic field exhibited cycloid movement around the cathode resulting in a much higher total path traversed. This results in a much higher probability of gas ionization which could significantly increase the sputtering rate and reduce the voltages needed to initiate the glow discharge. The patent also explains a similar system with planar cathodes, but with the magnetic lines being oriented parallel to the electric field thus providing magnetically enhanced sputtering. Developments related to magnetron supported sputtering with crossed electrical and magnetic fields were reported in the 1960s; Mullaly [39] described a sputtering system with quadrupole magnets. The experiments showed that increased sputtering rates could be achieved in addition to a better uniformity of the deposited film. Another study [40] presented the effect of having a magnetically enhanced sputtering by utilizing longitudinal, transverse, and quadrupole magnetic fields. The advantages and disadvantages related to the configurations were discussed with the quadrupole magnetic field providing superior performance. The invention very much resembling the modern magnetrons can be found in the patent filed by Chapin [41]. The apparatus consisted of a planar rectangular cathode with magnetic coils located behind it. The magnetic coils provided a magnetic field resembling an arc beginning from and return to the cathode surface providing the magnetic confinement of the secondary electrons, resulting in an increased ionization of the gas molecules in the proximity of the cathode. The erosion zone in this configuration was rectangular. One disadvantage of this particular design is that the plasma is confined to the cathode region and no ion-bombardment is provided for the growing film, a process that can positively affect the film growth and its physical-mechanical properties [42]. To overcome these issues, unbalanced magnetrons can be used. Changing the balance of the magnetron can be achieved by shifting the positions of the inner and outer magnets relative to the substrates [43]. Another way of unbalancing the magnetic circuitry is to employ a Helmholtz coil externally to the permanent magnets [42]. The application of this additional magnetic field results in an increase in the field strength of the outer magnet and the subsequent opening of the plasma trap which provides a higher ratio of ion/atoms arriving at the substrate.

Operating the magnetron was initially carried out by DC power (direct current Magnetron Sputtering DCMS) since it was the simplest and cheapest way. Modern developments in the DC power supplies are generally related to arc suppression. Using DC-power to sputter insulating targets like Al_2O_3, SiO_2 is not possible due to the accumulation of positive charges at the cathode. To overcome this issue, radiofrequency power supplies are used, typically with a frequency of 13.56 MHz. During the positive half-cycle, the ions attracted from the negative half-cycle are removed, thus providing conditions for the sputtering process to continue. If the frequency of the power supply sustaining the discharge is high enough, there will be not enough time for the ions to reach the target during the negative half cycle resulting in the formation of an

ion sheath and a net negative charge on the target due to the increased mobility of electrons compared to ions. The drawback of RF-powered magnetrons is the need for a matching network to compensate for the capacitive and inductive reactances of the discharge. Additionally, sputtering rates for RF-magnetron sputtering are lower because of the periodic opening of the electromagnetic trap which allows the electrons to escape. Another way for deposition of insulating films, such as Al_2O_3, is by sputtering of metallic targets in reactive (in this case O_2) environment. During reactive sputtering, insulating films can get deposited on the target (poisoning), which can further result in charge build-up and arcing if DC-power is used. RF-power supply can be used in this case but the need for matching network and the loss of efficiency encouraged the development of mid-frequency AC and pulsed-DC power supplies [44]. In the pulsed-DC solution, the polarity of the power alternates between negative and positive, with the negative cycle having a higher magnitude and usually longer time than the positive cycle (e.g asymmetric pulsed-DC). Frequencies often used in these power supplies range between 70-350 kHz with duty cycles (negative pulse time divided by the total time of the cycle) up to 70%.

The latest development in supplying the power for sputtering was initiated by Kouznetsov with the invention of high power impulse magnetron sputtering (HiPIMS, HPPMS) [45] [46]. This method of sputtering relies on applying pulses of very high instantaneous power ranging between 0.1 kW-1 MW with a duration of 50 µs-1 ms with pulse off time of 10-1000 ms. In a study by the same author, a very high degree of ionization of the sputtered Cu particles was observed. This higher ionization resulted in a very uniform film filling the trenches having a 1:2 aspect ratio. Additionally, the authors reported that the target racetrack was broader pointing out the potential of the method for better target utilization compared to conventional sputtering procedures. This study motivated various scientific groups to study, modify and utilize the HiPIMS method in order to deposit films with superior quality. Extensive reviews related to the more recent HiPIMS studies can be found by Sarakinos et al. [47] and Andre Anders [48].

It is important to note that the DCMS is a line of sight deposition process which results in more porous films because of atomic shadowing. The thickness distribution can also be an issue while depositing films on more complex geometries with studies presented in the literature is mainly focused on cutting tools [49]. To alleviate these issues HiPIMS is often used. Depositions performed by HiPIMS show much better thickness distribution on the surface with 90° orientation relative to the target compared to DCMS [50]. A similar study was done by coating cutting inserts using DCMS and HiPIMS [49]. With the HiPIMS deposition process providing better thickness uniformity between the rake and flank surface of the insert.

2.4.1 Sputtering related processes

The process of sputtering (see Figure 2-2) is the physical vaporization of atoms caused by the bombardment of surfaces with energetic atomic-size particles.

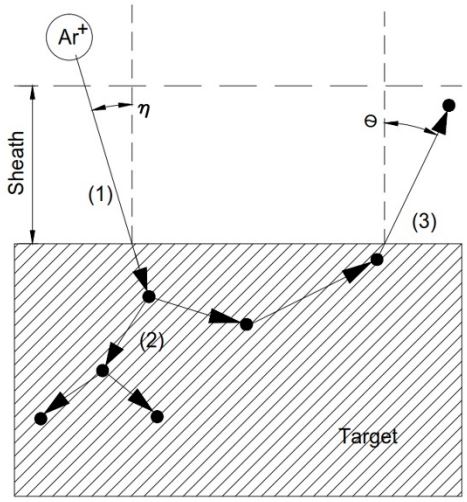

Figure 2-2 Sputtering event: (1) acceleration of an ion across the plasma sheath, (2) an atomic collision cascade in the target material and (3) ejection of a target atom, η is the incidence angle, θ is the ejection angle (adapted from [51]*)*

Since the process is based on the momentum transfer, the mass of the bombarding species is of great importance. This can be illustrated through the Laws of the Conservation of Energy and Conservation of Momentum. Based on these Laws the energy transfer during the collision of 2 hard spheres can be calculated using the following equation:

$$\frac{E_t}{E_i} = \frac{4M_tM_i}{(M_i + M_t)^2}(cos^2\eta) \tag{2.1}$$

Where E_t is the transferred energy, E_i is the incident energy M is the mass, i is for the incident particle and t is the target particle. Based on Eq. 2.1, the energy transferred is maximized when the masses of the incident and the target particle are similar ($M_t \cong M_i$), and when the incident angle is close to 0° ($\cos\eta = 1$). Therefore, sputtering materials with a higher atomic mass would be more efficient with heavier ions (e.g. Xe with amu of 131 or Kr with amu of 84). Nevertheless, the sputtering process is often performed with Ar (40 amu) due to its lower price [52].

Sputtering yield is a parameter related to the ratio of the number of sputtered atoms to the number of incident bombarding particles. The sputtering yield is affected by the: energy of the incident particles, the surface binding energy of the target material, and the angle of incidence.

The sputtering threshold energy is the minimum energy that is needed in order to cause sputtering. The threshold energy is proportional to the surface binding energy and it is affected by the masses of the bombarding and the target particles. Various empirical expressions regarding the sputtering yield and the sputtering threshold energy were proposed by Bohdansky et al. [53].

The energy distribution of the sputtered particles follows the following relationship, which is also known as the Thompson formula [54]:

$$\varphi(E)dE = \frac{E}{(E + E_{sb})^3} \tag{2.2}$$

Where E is the energy and the E_{sb} is the surface binding energy. The energy distribution has a maximum at $E_{sb}/2$ (few eV) and a tail at higher binding energies diminishing with E^{-2}.

The angular distribution of the atoms sputtered due to bombardment with energetic ions at a normal incidence generally has a cosine-type distribution [55]. A cosine distribution is illustrated in Figure 2-3.

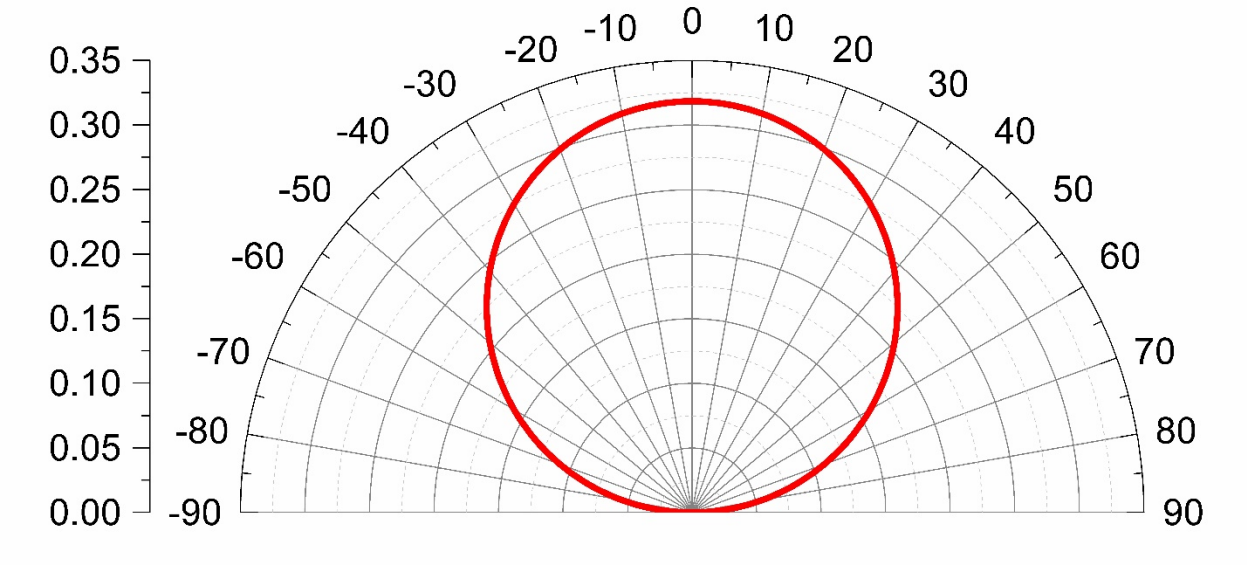

Figure 2-3 Cosine angular distribution of sputtered atoms

The angular distribution depends on the projectile mass and energy, and the angle of incidence. For low ion energies, the distribution is often "under-cosine", i.e. fewer particles are ejected in the direction of the target normal. Under-cosine and heart-shaped distributions are further promoted by the surface topography of the targets. This phenomenon is due to the fact that the atoms are ejected in a direction normal to the local surface features (hills and valleys) of the target [56].

2.4.2 Transport and condensation of the sputtered species

The sputtered species, after being ejected from the target, traverse the space between the target and the substrates in the vacuum chamber. The distance between the target and the substrate is typically between 5 cm and 30 cm. During their travel the sputtered species collide with the background gas and their energy is

reduced, a process often called thermalization. The frequency of collisions is related to the mean free path of the particles. The mean free path is the average distance a particle travels between collisions. The mean free path can be estimated using the following equation:

$$\lambda = \frac{1}{n_g \sigma} = \frac{k_b T}{p\sigma} \tag{2.3}$$

Where λ is the mean free path, n_g is the gas density, σ is the collision cross-section, p is the background pressure, k_b is the Boltzmann constant and T is the temperature. The collisional cross-section is an area that quantifies the probability that the scattering will occur during the collision of particles. The simplest approximation of the collision cross-section is the hard-sphere one where:

$$\sigma = \pi(r_s + r_g) \tag{2.4}$$

The r_s and r_g are the atomic radius of the sputtered particle and the background gas, respectively.

It is important to note that the mean free path of the sputtered species is inversely proportional to the background pressure. Therefore, increasing the pressure during the deposition will increase the scattering of the sputtered species and deposition of particles out of the line of sight of the target can occur. The typical deposition pressures during magnetron sputtering are between 0.1 and 1 Pa. In this range of pressures, the mean free path of the particles is typically in the range of few centimeters.

The sputtered species condense on the substrate and contribute to the film growth. During the condensation, they give up energy and cause heating. The film growth and its properties are affected by various factors. Some of the important factors are the energy of the condensing species, the angle of impingement, substrate temperature, deposition rate, surface roughness, surface mobility of the adsorbed atoms, and the concurrent bombardment of growing film. For example, species that arrive at the substrate at oblique angles will be captured by the hills and amplify their growth. As the hills grow, they will shadow the adjacent valleys and thus further reducing the arriving of species in the valleys. This process will cause the growth of a film with a porous columnar morphology. This process can be reduced by concurrent bombardment through the application of a negative voltage on the substrate. The concurrent bombardment can cause the re-sputtering of the growing film and subsequent re-deposition of the species in the valleys, thus, increasing the film density.

2.5 Thin films based on transition metal dichalcogenides for tribological applications-background and state of the art research

Transition Metal Dichalcogenides (TMDs) are compounds made of a transition metal atom (Mo, W, Nb or Ta) bonded to two chalcogen atoms (S, Se, or Te). The most widely studied TMD in the field of tribology is MoS_2, followed by WS_2. $MoSe_2$ and WSe_2 have also been studied but to a lesser extent. These compounds have lubricious properties due to their structure which can be depicted in Figure 2-4.

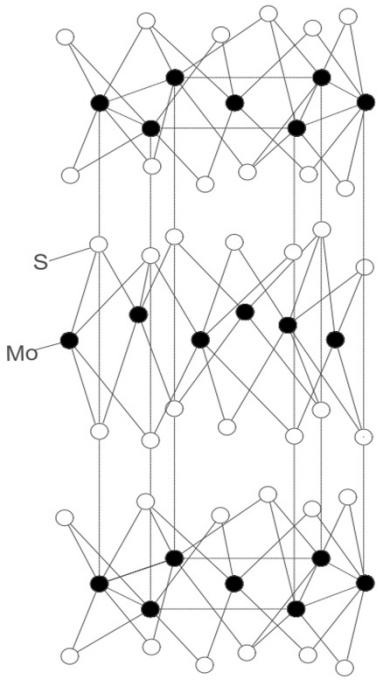

Figure 2-4 The structure of MoS_2

TMDs consist of "sandwiches" made of S-Me-S (Me-Transition Metal, S-Chalcogenide Atom) atoms which are strongly (covalently) bonded. Weak Van-der-Waals forces are holding the sandwiches together resulting in an interplanar weakness. Under shear forces, a crystalline slip will occur which can further result in the formation of transfer film during sliding [57].

Further in this section, the early usage of TMD thin films will be introduced, a small section related to metal doping of TMD materials will be presented and more extensive review on the carbon doping of TMD films will follow.

2.5.1 Early usage of TMD thin films for tribological applications

The usage of MoS_2 dates back to the mid-nineteenth century where it was used for lubricating axles of wagons by the California gold-miners [58]. The initial method for the deposition of TMD films was burnishing, a method in which sliding pressure is applied to the TMD powder (usually MoS_2) against the surface which is to be coated. A film consisting of (001) oriented MoS_2 on the top of randomly oriented MoS_2 crystals is formed [59]. The lubricity of the thin MoS_2 films has been reported in a paper by Fusaro [60] from the Nasa Lewis Research Centre. In this paper, the major drawback of the TMD films has been shown: the high sensitivity to humidity and atmospheric air. The friction in dry air and dry argon measured by a pin-on-disk apparatus (sliding against steel-based counterparts) was less than 0.02 whereas the lowest friction in humid air was 0.08, with a much shorter endurance life of 10 kilocycles compared to 100 kilocycles in dry air. Another method for the deposition of TMD coatings is by bonding. In this method, a binder is dissolved in a suitable solvent and the TMD particles are also dispersed in the solution. The solution is applied on a surface and the solvent is evaporated leaving a bonded coating with randomly oriented TMD crystallites. In a study by Bartz and Xu [61] the formation of blisters was attributed to a lower wear life during tribological testing.

Further research on TMD thin films was mostly focused on the deposition of coatings by PVD processes. PVD provides good controllability and high purity of the coating composition. Sputtered MoS_2 coatings have been reported as early as 1971 by Spalvins [62] also from the Nasa Lewis Research Centre. The coatings 200-650 nm thick were deposited by RF-diode sputtering and tribologically evaluated in a vacuum tribometer. Friction coefficients of 0.03-0.04 were reported. The good tribological behavior in vacuum environments was the reason for their usage in spacecraft and satellite moving mechanical components and assemblies [63]. Co-sputtering of metals has also been investigated in a way to improve the tribological properties of pure MoS_2 coatings [64]. The Ni addition in the range of 5-8 at% was considered as the optimum quantity with which superior tribological performance could be achieved compared to pure MoS_2 coatings. The underlying mechanisms behind the improvement were not explained by the author.

During the 1990s tribological studies of thin films based on TMD were mainly performed on coatings deposited by sputtering procedures. Grosseau-Poussard et al. [65] deposited MoS_x coatings by ion-beam assisted deposition and compared them with sputter-deposited ones. The authors reported that high energy ion beam assisted deposition could result in the inhibition of TMD crystallites orientation, with the basal planes oriented parallel to the surface, which significantly decreased the wear life. In the case of layered TMD clusters parallel to the surface, the sputter-deposited coatings had much better wear life in the argon environment. WS_2 thin films deposited by another PVD process (Pulsed Laser Deposition (PLD)) were tribologically studied by Prasad and Zabinski [66]. The focus of this study was on the transfer film

formation during sliding. The major drawback of the sensitivity to humidity, which was well known for TMDs, was confirmed and it was speculated that the formation of WO_3 hindered the lubricity in the humid air. In a study performed by Lince and Hilton [67] on RF sputtered MoS_2 thin films, the effect of oxygen on the microstructure of TMD studies was presented. In particular, the authors reported that oxygen could replace the sulfur atoms and a $MoS_{2-x}O_x$ phase was formed. The improvement of the humidity resistance of MoS_2 thin films by metal ion implantation was also attempted [68]. In this work, thin films were deposited by RF magnetron sputtering and subsequent metal ion implantation was done by using Ag^+ and Y^+ ions. It was reported that the film adherence and the wear life were improved by ion implantation; in terms of oxidation resistance, Ag^+ ions had a positive effect while Y^+ ions caused increased oxidation in humid environments. Further studies were mainly focused on controlling the microstructure of the magnetron sputtered TMD based thin films through doping with various elements. Ni and Au-Pd addition to MoS_2 solid lubricant film, but in the form of nanostructured multilayers, have also been studied [69]. The multilayered nanostructure, in this case, increases the basal orientation of the TMD film. Additionally, the films had dense and smooth morphology showing an increased wear life and friction in the range of 0.05-0.08. Doping the TMD films with an element, which could form lubricious compound at elevated temperatures, was also tried [70]. The PLD deposited WS_2-ZnO thin films had amorphous nature after deposition at RT but, after wear testing, crystalline WS_2, WO_3, and $ZnWO_4$ phases were detected. To increase the tribological performance of MoS_2 thin films, the introduction of interlayers (Cr or Cr_3Si) is also reported [71]. Various changes in the process parameters, like the target to substrate distance, power and pressure, were tried by the authors and the relationship between them and the microstructure was reported. The best tribological behavior was reported for films that had higher (002) orientation and negligible (100) and (110) reflections from the measurements done by XRD. The addition of small amounts of rare earth metal (LaF_3) to MoS_2 sputtered films were studied in terms of oxidation resistance by Yu et al. [72]. Doping with LaF_3 resulted in denser and more oxidation resistant film.

The assessment of the effect of crystal orientation on the tribological response of MoS_x in fretting tests was studied by Zhang et al. [73]. A strong influence of the crystal orientation while testing in humid air was observed which was related to the oxidation sensitivity of the randomly oriented MoS_x. It was also reported that switching from humid air to dry air, for the basal oriented films, causes recovery of the low friction characteristic for TMD thin films.

Thin films based on the $MoSe_2$ TMD are much less studied. Kubart et al. [74] deposited pure $MoSe_2$ films by DC magnetron sputtering and compared them with the well-studied MoS_2 films. Tribological studies at different relative humidity revealed that $MoSe_2$ is less affected in humid air showing better lubricity compared to MoS_2. In a dry atmosphere, MoS_2 was reported to have better performance.

2.5.2 Metal doping of TMD films

Significant improvement of MoS_2 films by Ti doping has been reported by Teer and his coworkers [75,76]. The coatings with registered trademark MoST™ were deposited in a chamber with closed-field unbalanced magnetron sputtering configuration with 4 targets. The addition of 20 at. % of Ti resulted in coatings with a friction coefficient of 0.05 in an environment with ~40 % humidity. The hardness by nanoindentation was ~15 GPa. The industrial testing was carried out with coated drills and dies in metal cutting and forming industry. The authors reported excellent results from the industrial tests.

The deposition of nanostructured multilayered MoS_2-metal (oxide) was performed by Mikhailov et al. [77] to better understand the role of metal doping in terms of the humidity resistance of sputtered TMD-coatings. Metals with different sensitivities to oxygen were incorporated in a multilayer structure with a metal layer of 3-7 nm and MoS_2 of 33 nm thicknesses. The frictional testing in humid environment showed an improvement compared to pure TMD coating which was due to the increased basal (002) orientation of the TMD phase. The authors did not observe any specific role of the type of the metal layer.

The addition of sputtered MoS_2 to hard coatings developed for cutting operations was also reported [78]. The motivation behind this type of research was to reduce the friction between the cutting tool and the workpiece and, therefore, to eliminate or reduce the use of cutting fluids. The addition of MoS_2 to TiAlN coatings resulted in the improvement of the tribological performance compared to the pure TiN or TiAlN coatings.

2.5.3 Carbon addition to TMD films

The significant improvement of the aerospace systems caused the need for a much improved tribological behavior of their sliding components. This need was in the basis of the development of nanocomposite coatings with adaptive nature in terms of the friction response related to the testing atmosphere [79]. One of thiese coatings was the WC/DLC/WS_2 nanocomposite consisting of nanograins of WC and WS_2 (with a size of 5-10 nm) embedded in an amorphous C matrix. The WC provided the mechanical strength of the coating whereas the other elements could take care of the low friction. The adaptive tribological behavior of the coating could provide lubricity by either the graphitization of the C phase during sliding in ambient environments or, on the other hand, the crystallization and reorientation of the WS_2 grains, at the sliding interface, when testing in dry and vacuum environments. These results encouraged further research of TMD-C thin films which will be covered later in this section. The concept of nanocomposite coatings with "chameleon" tribological behavior was further explored by Voevodin et al. [80] with the deposition of YSZ/Au/MoS_2/DLC coating by a combination of magnetron sputtering and magnetron assisted pulsed laser deposition. The coating consisted of an amorphous DLC phase with nanocrystalline inclusions of ZrO_2 and Au with a size of 3-8 nm. Reservoirs of amorphous MoS_2 were also present in the coating. The tribological

adaptation of the coating was observed with the TMD phase providing lubricity in the vacuum and dry nitrogen environments (COF of 0.02-0.03), the DLC phase with a lubricious role in humid air, by the formation of graphite-like transfer layers (COF of 0.1-0.15), and the Au giving rise to tribofilms (COF of 0.2-0.25) when testing at 500˚ C with laboratory air.

Several publications on C and N doping of WS_x films were prepared by Nossa and Cavaleiro [81–83]. All coatings were deposited by RF magnetron sputtering. In their first publication [81] W-S-C and W-S-N system were deposited using reactive sputtering (CH_4 and N_2 atmosphere in addition to Ar) with the addition of C up to 60 at.% and addition of N up to 20 at.%. C and N addition resulted in increased hardness and coatings with more amorphous nature when compared to pure WS_x films. Substochiometry (ratio between chalcogen atoms and transition metal atoms- X/M) in relation to WS_2 was related to the preferential sputtering of S from the growing film. Friction coefficients between 0.08 and 0.32 were reported, being the coating detachment the main failure mechanism. The second paper [82] is related to reactive magnetron sputtered films with similar composition, with the incorporation of a Ti interlayer. Significant improvements in terms of adhesion were observed with a similar frictional response. The increase in the adhesion gave rise to a much better wear resistance of the coatings. Additional characterization of the coatings was performed by X-ray photoelectron spectroscopy, XPS, in the third publication [83]. The XPS study showed the presence of W-C bonds, for the C doped films with low to moderate C contents (up to ~50%), whereas C-C bonds were mainly found for the coatings with the highest amount of C content. W-N bonds were also detected for all N doped films. To additionally explore the microstructure of the WS_2 films alloyed with C and N, a study focused on high-resolution transmission electron microscopy was performed [84]. The study revealed that the films alloyed with C contained W-S and W-C grains embedded in an amorphous C matrix. The films doped with a high amount of N showed an amorphous structure.

The same research group continued the investigation of TMD based films. Evaristo et al. [85] deposited the W-S-C system using the same deposition chamber in a co-sputtering configuration from 2 targets of WS_2 and C. The films were compared with those deposited by reactive sputtering (WS_2 and CH_4). Co-sputtered coatings were reported to have an amorphous structure and comparable adhesive strength to reactively sputtered coatings, in spite of the absence of the Ti interlayer. The S/W ratio was lower for the reactively sputtered films which was attributed to the formation of H_2S; in terms of hardness, the reactively sputtered films were superior. More tribological studies of the W-S-C films followed, namely Polcar et al. [86] explored the tribological behavior of the films using an unidirectional pin-on-disk apparatus under incaasing loads (5-47 N) in ambient air with a relative humidity of 30%. A decreasing trend was observed for the friction coefficient as the load was increased. The coatings with C content between 37-51 at. % were reported to have values as low as 0.05.

Motivated by the good tribological results for $MoSe_2$ when sliding in normal air, Polcar et al. [87] deposited Mo-Se-C films using the same RF magnetron sputtering system used in previous studies of W-S-C. The target was of composite nature, a C target with $MoSe_2$ pellets placed on top of it. The films had a Se/Mo ratio in the range 1.7-2, which was much higher compared to S/W one in the previous studies; the C content was varied between 30 and 70 %. From the microstructural analysis, the authors depicted a film consisting of amorphous carbon with embedded nano-grains of $MoSe_2$. From the XPS analysis, no Mo-C bonds were detected. The occurrence of $MoSe_2$ nano-grains was confirmed by TEM [88]. The tribological study [89] on these particular coatings confirmed their potential. The friction coefficient was 0.07-0.08 when testing in normal laboratory air under 5N load. The testing was also performed with increased temperature up to 250 °C, resulting in a drop of the friction coefficient down to values of 0.01-0.04. The testing was attempted at 300°C but no coating survived that harsh environment. From the Raman measurements, the authors depicted that the frictional behavior was mainly driven by the TMD phase with the C phase having a marginal effect. The tribological testing was also performed with increased loads at atmosphere with 35% RH [90]. A low friction coefficient of 0.05 was measured while testing the coating with 51 at. % C under a load of 33N, the wear rate was also quite low with a value of 6×10^{-7} $mm^3N^{-1}m^{-1}$. Various techniques were then employed to analyze the wear track of the tested sample. Auger Electron Spectroscopy depth profiling showed that the topmost layers are rich in Mo and Se. Lateral force microscopy was also performed on both the wear track and the as-deposited coating; the wear track showed a decreased friction force which could be attributed to low friction tribolayers. The final confirmation of the presence of thin layers of $MoSe_2$ on the contact surface was reached after high-resolution TEM study after preparing the samples by focused ion beam (FIB). From the HRTEM images, it was concluded that the randomly oriented platelets of $MoSe_2$ in the as-deposited coating were getting reoriented during sliding, aligning their basal planes parallel to the surface, thus, providing a significant friction reduction. An additional tribological study on the same coatings was focused on the wear mechanisms occurring during testing in different atmospheres [91]. It is important to note that the coatings were deposited 5 years before testing and stored in room conditions before the microstructural and tribological characterization. This gives valuable information in terms of the potential degradation of the Mo-Se-C films. A significant reduction in friction was observed in dry air, Ar and N_2 compared to the ambient air testing. The wear rates followed the same trend although with a not such a big difference between testing in humid air and in the other three more inert environments. TEM analysis on FIB prepared samples from the wear track and the transfer film on the ball counterpart showed well aligned basal oriented $MoSe_2$ crystals on the sliding interface. EELS analysis confirmed the presence of MoO_3 in the agglomerates found in the transfer film on the ball from the tests in humid air. This result pointed out that the oxidation of $MoSe_2$ is the most probable reason for the increase in the friction. The extensive surface analysis of the worn surfaces revealed that the top layers were carbon depleted and the

main function of the C phase is to increase the hardness of the films. Then, during sliding smaller contact area was provided which is crucial for the friction reduction.

WSe_2 based films deposited for potential tribological applications are much less available in the literature. Evaristo et al. [92] studied films of W-Se-C similarly as the previously RF sputtered deposited W-S-C and Mo-Se-C. The films deposited by co-sputtering had C content up to 70%, with Se/W ratio of 0.8-1.6. Reactively sputtered films had 25 and 66% C with Se/W ratio of 1.7-2.3. One issue during the deposition was the evaporation of the target with subsequent deposition of pure Se film. This issue was tackled by using much lower powers on the 100 mm WSe_2 target (40-75 W) resulting in very long deposition times (6 hours) and high oxygen contents (10 at. %). The co-sputtered coatings were harder with increasing C content, contrarily to the reactively sputtered coatings, having lower hardness and not significantly changing with C incorporation. A more detailed tribological study was done in an additional publication [93] where W-S-C and W-Se-C were compared. Friction as low as 0.05 was reported. In relation to wear, generally, adhesion-related problems were observed with the coatings suffering peeling off during testing. The maximum testing load was 200 N. Another research group deposited a W-Se-C coating on top of a thin DLC film using pulsed laser deposition [94]. The coating with 60 at. % C had the highest hardness of 9.4 GPa with the Se/W ratio close to 1.4 for all C contents. The hardness increase was due to the formation of WC and β-W spherical nanoparticles identified by TEM. An interesting feature was the formation of a W-Se phase on the edges of the β-W phase. The tribological testing was carried out in fretting mode [95] under a load of 5 N at room temperature and RH of 50 %. The lowest friction coefficient was 0.04. W-Se and W-Se-C films with tailored microstructure were grown by RF magnetron by Dominguez-Meister et al.[96]. The preferential re-sputtering of the chalcogenide atoms during film growth led to the formation of a W-rich layer which improved the adhesion of the film to the substrate. For this, a modulated pulsed-DC bias was applied to the substrate, starting with 25 W and reducing the power at a rate of 5 W per hour; the final 1 hour of the deposition was done without bias. The same study also reported W-Se-C films deposited by RF co-sputtering of WSe_2 and WC targets. Friction coefficients of 0.06 and 0.08 (laboratory air) were measured for the W-Se-C and W-Se films grown with the modulated bias approach. The structural reordering of the lubricious amorphous WSe_2 phase was assumed to be the underlying mechanism for the friction reduction. The same films were also tribologically studied varying the testing pressure [97], from 10^{-7} mbar up to atmospheric and, finally, back to 10^{-6} mbar. Surprisingly, no significant change of the friction was observed during the whole test with values staying around 0.05. HRTEM studies showed the presence of amorphous W-rich areas with platelets of WSe_2 embedded in it. The tribofilms showed crystallization of the TMD phase on the sliding interface, with the W playing a sacrificial role in terms of oxidation protection for the TMD phase.

WS_2/a-C films were also studied by Cao et al. [98], in particular the effect of the discharge pressure on the microstructural and mechanical properties. The lowest deposition pressure of 0.3 Pa resulted in films with the lowest S/W ratio of 1.3, while higher deposition pressures (around 0.75 Pa) gave rise to a better ratio of 1.7-1.8. This was explained by the reduced energy of Ar species bombarding the substrate when the pressure was increased, resulting in a reduced S resputtering from the growing film. The coatings grown at a lower pressure (lowest S/W ratio) have the highest hardness which could be related to the availability of W to form W-C bonds; the coating with 50 at. % C had a hardness value of 10.6 GPa. The tribological testing in a normal atmosphere showed a coefficient of friction of around 0.15 which is much higher compared to the previous studies of W-S-C films. The same research group also studied the effect of the substrate to target distance for the same WS_2/a-C system [99]. Higher target-to-substrate distance resulted in higher S/W ratio; then, increased hardness was achieved for the films grown at low distances. The coating deposited at higher distances showed better performance with a CoF of around 0.1 in ambient air. The Raman study of the wear tracks has shown the presence of a-C.

2.6 Summary of the review and research gaps

Because of the tribological potential of TMD materials, various studies have been performed during the last 30 years. As they have excellent performance in vacuum, initially the studies were focused on aerospace applications. There have been plenty of attempts to enable the tribological feasibility of TMD based materials in room conditions. The most successful solutions in the literature are the Ti-doped MoS_2 by Teer and his coworkers, with films having CoF of 0.04-0.05 in an ambient atmosphere. Moreover, these films were also successfully tested in industrial conditions. Another important milestone was the development of the WC/WS_2/DLC nanocomposite coatings, by Voevodin et al., for which CoF values of around 0.1-0.15 were achieved with the authors considering that the DLC phase governed the friction in humid air with the W-S phase being responsible for a suitable tribological performance by an adaptive response in other testing atmospheres. The potential of the TMD-C thin films was further explored in a series of studies by the SEG group at CEMMPRE. The studies showed a non-Amonton behavior of TMD-C films with decreased friction with increasing loads. Values between 0.04 and 0.07 were often measured during sliding in room conditions. Nitrogen-doped TMDs were also the subject of various studies but the good frictional response was only observed during sliding in inert environments (e.g. dry nitrogen). From the C alloyed TMDs, W-S-C based films appear to be the most studied material. On the other hand, $MoSe_2$ based thin films with the addition of carbon are less studied although having better performance in ambient air compared to MoS_2. It must be noted that the Mo-Se-C studied were deposited using RF sputtering with $MoSe_2$ pellets placed on the erosion zone of a graphitic target. Regarding the microstructure, the amorphous carbon (a-C) matrix with embedded randomly oriented nanosized TMD platelets is the most advantageous for tribological

applications. During sliding, the nanograins can be easily reoriented with their basal planes parallel to the surfaces, facilitating sliding, and its dangling bonds protected by the a-C matrix avoiding the oxidation. Some studies also have shown that amorphous coatings can also provide friction reduction when crystallization occurs during sliding, as a result of the mechanical work and the temperature increase.

Most of the studies in the literature related to TMD-C were performed on coatings prepared in small laboratory chambers with rare examples of the usage of bigger deposition units (e.g. four cathodes in a closed-field unbalanced magnetron sputtering configuration). The depositions were historically performed through different routes like sputtering of individual targets (graphite and TMD), sputtering composite targets, and sputtering a TMD target in carbon-containing gas (e.g. methane). Substrate bias was rarely used. The substrates were often cylindrical coupons with the planar surface being coated for tribological testing with standard pin-on-disk devices. No studies have shown the use of more complex substrates, such as those involved in sliding during operation in real service conditions. The research related to films based on $MoSe_2$ and WSe_2 types of TMD is also lacking in spite of their possible advantage for applications in room conditions. Another benefit of the films including TMDs with the chalcogen atom being Se is the reduced resputtering of the chalcogen atoms during film growth. Biasing the substrate during film growth was often evaded as it leads to a very poor ratio between the chalcogen atoms and the transition metal atoms of the TMD phase which hinders the lubricity. Bias usage can greatly improve the mechanical properties of the Mo-Se-C coatings as found, for example, in DLC coatings often having superior performance when appropriate substrate bias is used.

2.7 Challenges regarding the upscaling of the deposition process.

Lab-scale deposition of TMD containing thin films was often performed by RF magnetron sputtering, very likely due to the reduced conductivity of the TMD materials and thus having more stable discharges (e.g. less arcing) with RF voltages as compared to DC voltages. Utilizing RF power supplies in industrial-scale deposition units is often evaded due to the increased costs. The increased costs are because of the additional instrumentation needed, like the matching networks used for matching the capacitive and inductive reactances. The costs are further increased because of the generally lower deposition rates.

The lab-scale chambers often have much shorter target-to-substrate distance (TSD of e.g. 5-10 cm), which is usually fixed. Additionally, the substrates are often continuously exposed to the flux of sputtered species. Deposition on an industrial scale can be performed at a wide range of TSD, typically ranging from 10-30 cm, a distance governed by the size of the part to be coated and its geometry. Moreover, the parts in industrial units are often fixed on rotating carousels and their surfaces are intermittently exposed to the targets (the flux of sputtered species).

In the context of the difference in the TSD, the scattering of the sputtered species is expected to be increasingly important in the industrial scale deposition compared to the lab-scale deposition. The importance of the scattering of the sputtered species is further amplified by the fact that there can be a significant difference in the atomic mass of the constituents of the TMDs (e.g. S and W). This will cause a significantly different scattering behavior during the collision of the S and W atoms with the background Ar gas. On one hand, the lighter S atoms will be scattered more, increasing the probability of condensation of S atoms on the chamber walls. On the other hand, the heavier W atoms are expected to have more straight traversing paths, and thus, deposition out of the light of sight of the target is not expected.

The intermittent exposure of the surfaces to the targets will facilitate the shadowing effects, i.e. the coated surfaces will be exposed to the flux of species at various angles to the substrate normal which increases the shadowing effects and the columnar growth. Another issue that might arise during the deposition of the coatings in bigger units is the temperature. Due to the bigger mass of the parts as well as the fixtures used, the temperature can be significantly lower. The lower temperature will affect the adatom mobility, and thus, the morphology of the film.

Improving the density of the films synthesized by sputtering techniques is often performed through the bombardment of the films with energetic species. The bombardment is usually performed by applying a negative voltage on the substrate holder. Application of substrate bias on a component with more complex geometry (e.g. component that contains sharp edges) can cause increased ion bombardment on the edges. This process can significantly alter the composition and the properties of films composed of multiple elements due to preferential sputtering of some of the atoms (typically the atoms with lower atomic mass).

2.8 Main objectives

PVD techniques have greatly evolved in the last 2-3 decades with an increasing amount of coatings being used in various industries such as the metalworking and automotive industries. The research towards friction reduction in several industries has resulted in a significant amount of surface engineering-based solutions for friction and wear reduction. Properly tailored lab-scale deposited TMD-C coatings perform rather well for friction reduction which is a good enough reason to perform further studies in attempting to upscale the deposition process for the cases providing the most promising results. A strong advantage of the nanocomposite TMD-C coatings is their unique ability to provide friction and wear reduction in various operating environments.

Therefore, the main objective of this project will be to upscale the magnetron sputtering deposition processes for TMD-C thin films. Currently, the most promising solutions are W-S-C and Mo-Se-C coatings; then, these two coatings will be studied.

The specific objectives of the thesis are as follows:

- Studying the relationships between the properties of W-S-C coatings and the different routes for coatings deposited in lab-scale equipment.
- Preparation of W-S-C and Mo-Se-C coatings in semi-industrial scale equipment
- Understanding the relationships between the placement of the samples at various locations in the chamber and the composition of the coatings
- Evaluation of the crystallinity, morphology, microstructure, adhesion and mechanical properties as a function of the composition and, thus, the processing parameters
- Tribological evaluation of the synthesized coatings in various operating environments, like ambient air, dry N_2, elevated temperature and vacuum

The ultimate goal of the thesis is to obtain recipes for a consistent deposition of self-lubricant carbon alloyed TMD coatings in a semi-industrial deposition unit. The coatings should provide friction and wear reduction in a wide range of operating conditions like vacuum, ambient air, and elevated temperature up to 300-400°.

Chapter 3 Experimental methods

In this chapter, the magnetron sputtering deposition equipment used for the synthesis of the coatings as well as the processing parameters will be presented. Detailed information regarding the methods, the equipment, and the parameters for the characterization of the coatings will also be presented.

3.1 Preparation of the coatings

3.1.1 Lab-scale depositions

The W-S-C(H) coatings prepared in the lab-scale deposition equipment were deposited by RF magnetron sputtering (Edwards E306A) in a unit equipped with 2 magnetrons. A schematic of the configuration can be seen in Figure 3-1 a).

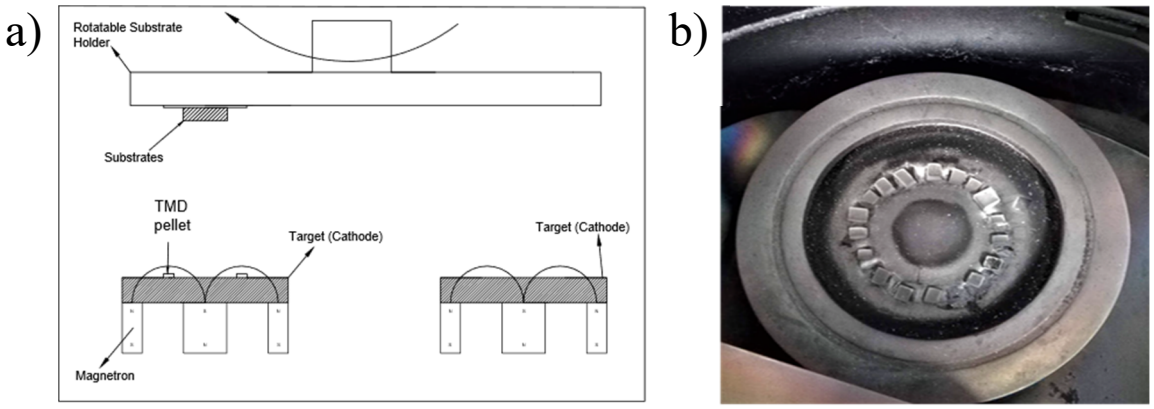

Figure 3-1 a) schematics of the deposition unit b) a carbon target with WS_2 pellets placed in the erosion zone

The targets mounted on the magnetrons have a diameter of 100 mm and are connected to RF (13.56 MHz) power supplies with a maximum power output of 1000 W (Huttinger PFG 1000) and 500 W (ENI OEM 6), respectively. The substrate holder was also connected to an RF power supply with a maximum power output of 1200 W (ENI OEM 12a). The power supplies were connected with the magnetrons through matching networks. The base pressure before the deposition was less than 10^{-3} Pa attained by a turbomolecular pump backed by a rotary vane vacuum pump. The distance between the targets and the rotatable substrate holder is fixed at ~6 cm. The depositions were carried out using Ar gas with a pressure of 0.75 Pa, except for the reactive sputtering where a gas mixture of Ar/CH_4 with a total pressure of 1 Pa was used. The substrate holder can rotate or be stationary over the targets. During rotation, the substrate holder intermittently passes over both targets. The direct position of the substrate holder over one of the targets is also possible.

Different deposition routes were chosen for coating: co-sputtering of 2 separate graphite (Testbourne Ltd, 99.9 % purity) and WS_2 (Testbourne Ltd, 99.9 % purity) targets, co-sputtering a composite target composed of a graphite target with pellets placed in the erosion zone (see Figure 3-1 b)) and sputtering of a WS_2 target in reactive methane (CH_4) gas. The sputtering of the composite target was also performed with the substrate holder being stationary and rotating over the target.

For co-sputtered films from separate WS_2 and graphite target, the power density to the WS_2 target was set to 2 W/cm^2 while the power to the C target was varied between 3.8 W/cm^2 and 7.6 W/cm^2 (300-600 W), to deposit films with C content between 40 and 50 % since, in previous studies, these compositions showed the best tribological results. The films co-sputtered from a composite target were deposited by placing WS_2 pellets (5 mm × 4 mm × 2 mm) in the erosion zone of the C target. To reach similar C contents as the other co-sputtered coatings, the number of pellets was changed between 21 and 13. In this particular route, the thin films were deposited by having the substrate holder rotating or in the stationary position. The number of pellets was kept the same for both modes. The power density was set to 7.6 W/cm^2 and 3.8 W/cm^2 for the rotating and stationary mode respectively. Magnetron sputtering in reactive mode was performed by sputtering a WS_2 target in a gas mixture of Ar and methane (CH_4). The depositions were performed only by having the substrate holder rotating. The power density was 3.8 W/cm^2. The partial pressure of the CH_4 gas (p_{CH4}/p_{total}) was set to 28-48 %, by adjusting the flow of the CH_4 gas.

Three films were deposited per route resulting in a total of 12 films. The coatings will be referred to as Dx-y where x=1,2,3,4 refers to; 1 - co-sputtering of 2 targets; 2 - sputtering a composite target with the substrate rotating; 3 - sputtering a composite target with the substrate being stationary and 4 for reactive sputtering. The number y refers to the power (W) to the C target used for the co-sputtered films, the number of pellets for the sputtering of a composite target, or partial pressure (%) of the CH_4 gas during reactive sputtering. For example, D3-17 is the film deposited by sputtering a composite target with 17 pellets placed in the erosion zone and a stationary substrate holder. Before deposition, the targets were sputter cleaned for 10 min. each, while the substrates were sputter cleaned for 20 min. For improving the adhesion to the metallic substrates, a Cr interlayer with a thickness of ~200 nm was deposited for the films deposited by sputtering a composite target and reactive sputtering (D2, D3, and D4 coatings). For the D1 case, Cr interlayer could not be deposited as both cathodes were used for the deposition of W-S-C coatings. The substrates were silicon wafers and AISI M2 steel coupons. Steel substrates were polished to R_a ~ 20 nm using diamond suspension and they were mainly used for the scratch testing and tribological evaluation. The substrates were not biased during deposition and no intentional substrate heating was used.

3.1.2 Semi-industrial scale deposition

The coatings deposited in the semi-industrial deposition unit were W-S-C and Mo-Se-C. The unit is equipped with 4 unbalanced magnetrons in a closed-field configuration (Teer Coatings Ltd UDP 650/4). A schematic and a picture of the equipment can be seen in Figures 3-2 and 3-3, respectively. The neighboring unbalanced magnetrons have the outer magnetic assembly with opposite polarity, producing a closed magnetic ring. The closed magnetic field lines are in the zone where the substrates are located, entrapping the secondary electrons emitted from the target, and thus ionizing the gas in the proximity of the substrates.

The enhanced plasma, present close to the substrates can be used for sputter cleaning of the substrates before deposition and/or bombardment of the growing film with Ar^+ ions during deposition [100]. The diameter and height of the chamber are 650 mm. The chamber is pumped using a diffusion pump backed by a rotary vane pump. The vacuum achieved before the deposition is below 3 x 10^{-4} Pa. The ultimate vacuum pressure is measured by an active inverted ionization gauge whilst the deposition pressure is measured by a capacitance manometer. The deposition was performed in an Ar atmosphere. The rectangular planar targets, vertically aligned on the chamber walls, have a dimension of 380 x 175 mm^2 with a nominal thickness of 10 mm. For achieving a broad range of carbon contents, 2 graphite targets (Testbourne Ltd. 99.99 % purity) and a single TMD (WS_2 or $MoSe_2$, Testbourne Ltd, 99.9 % purity) were used. The graphite and the TMD targets were bonded to a copper backing plate (thickness of 4 mm) with conductive silver-filled epoxy. The placement of the targets on the respective magnetrons can be seen in Figure 3-2. The configuration is the same for the Mo-Se-C coatings, only the WS_2 target was exchanged for a $MoSe_2$ target.

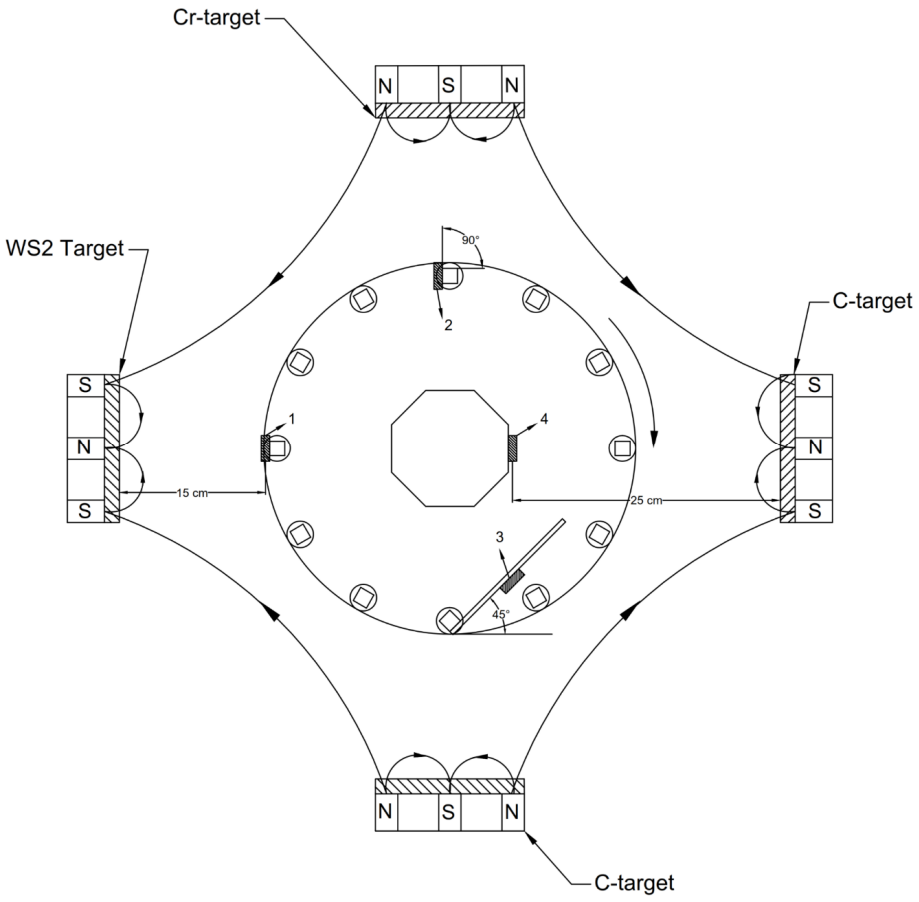

Figure 3-2 Schematic of the target configuration used for the deposition of W-S-C coatings in the semi-industrial deposition unit

Figure 3-3 Teer UDP 650/4 deposition unit

The targets were connected to DC power supplies (Advanced Energy Pinnacle) with a maximum power output of 6 kW. The carousel is connected to a pulsed-DC power supply (Advanced Energy Pinnacle Plus) with a maximum power output of 5 kW.

The substrates are placed on a carrousel that is subjected to a rotation with a speed of ~10 rpm, which is the maximum. The substrates were subjected to a single rotation. Before deposition, the substrates were sputter cleaned for 40 min using a p-DC voltage of 600 V, at a frequency of 250 kHz, and a reverse time of 1.6 µs. The targets were simultaneously sputter cleaned for 20 min, with a shutter placed in front of them to prevent cross-contamination. Target cleaning was performed in pairs (for example, C and WS_2 are sputter cleaned first, and then, C and Cr are sputter cleaned), with the opposite targets being cleaned together. This procedure allows plasma enhancement in the substrate region (from the unbalanced magnetrons) and high ion current can be drawn on the substrates, resulting in efficient sputter cleaning of the substrates. No additional substrate heating was used. The substrates were polished single crystal silicon wafers, AISI M2

tool steel, and DIN 100Cr6 bearing steel. The steel substrates were polished down to roughness of R_a < 20 nm using SiC papers and diamond suspension subsequently, with a minimum particle size of 3 µm. Thin coatings (30-50 nm) were also deposited on carbon-coated transmission electron microscopy (TEM) grids (Mesh 400).

An adhesion improving Cr interlayer was used as Cr can establish strong metallic bonding with the steel substrates. The deposition of the Cr interlayer was performed for 10 min at a power density of 3 W/cm^2 and a negative substrate bias voltage of 110 V. Afterwards, a gradient Cr/TMD-C was deposited by ramping down the power applied to the Cr target whilst ramping up the power applied to the C and TMD targets to the setpoint used for deposition. The substrate bias was also ramped down to the setpoint value used for the deposition of the TMD-C coatings. The gradient layer provides a smoother transition in chemical composition. The total deposition time was 120 min. The deposition sequence is illustrated in Figure 3-4.

The first depositions in the semi-industrial scale were W-S-C coatings (Chapter 5). Variation of the chemical composition was performed by setting the power density to the WS_2 fixed at a value of 2.1 W/cm2 and changing the power density applied to the graphite targets. The power density applied on each graphite target was set to 2.6 and 3.2 W/cm^2, to achieve C contents in the range of ~40-50 at. %. Additionally, a set of coatings was deposited by having the power density to each graphite target set to 2.6 W/cm^2 with 50 V bias applied to the substrate. The substrates were placed at three target-to-substrate distances (TSD) of 10, 15, and 25 cm. The total number of coatings deposited was 9. An additional study was performed on W-S-C coatings by placing the substrates at different locations in the chamber (Chapter 6). The first location (see Figure 3-2) was at a target-to-substrate distance of 15 cm with the surface to be coated facing the targets. The second location was at a target to substrate distance of 15 cm with the surface to be coated positioned at an angle of 90° relative to the target surface. For the third location, a copper plate with a width of 16 cm, a height of 23 cm and 3 mm thickness was fixed on the carrousel and rotated at 45° relative to the target surface (position 3 in Figure 3-2), the substrates were fixed at the center of the stationary plate. The final substrates (position 4) were placed on an octagonal block positioned at the center of the chamber, at a target-to-substrate distance of 25 cm. The coatings will be further referred to as WSC-x, with x (1,2,3,4) being the position of the substrate as shown in Figure 3-2. During the deposition, only the carousel is rotated while the samples to be coated are being stationary at their respective positions. To achieve a carbon content of ~ 50 at. %. the power density applied to each graphite targets was set to 3.2 W/cm^2 whilst the power density applied to the WS_2 target was set to 2.1 W/cm^2.

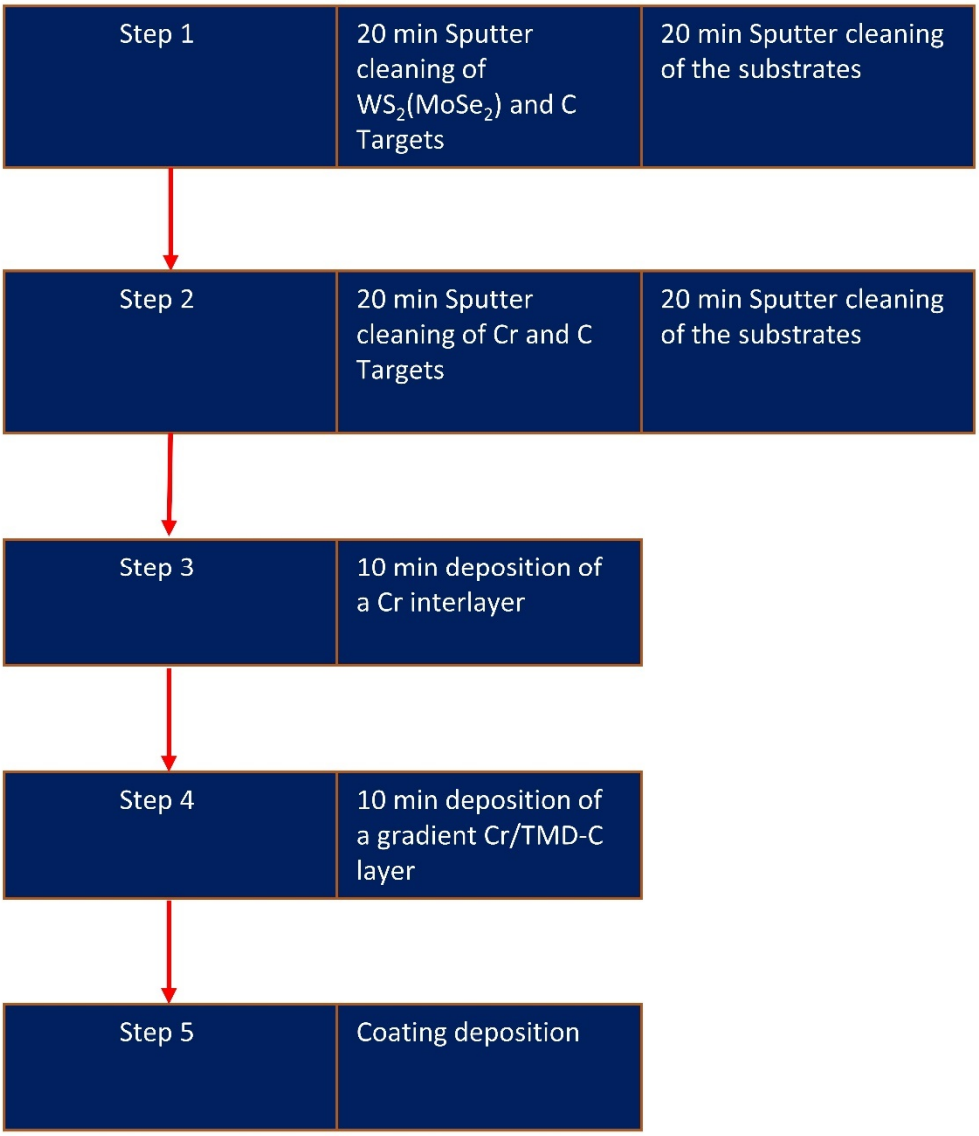

Figure 3-4 The sequence of steps during the deposition of the coatings in the semi-industrial equipment

For the deposition of the Mo-Se-C (Chapter 7), the power supplies were operated in current control mode due to unstable operation (large fluctuation of voltage and current) when power control mode was used. The current density applied to the $MoSe_2$ target was 3.6 mA/cm^2. For the carbon alloyed coatings, the current density applied to both graphite targets was 5.3 mA/cm^2. Pure $MoSe_2$ coatings were also deposited, without applying any current on the graphite targets, these coatings will be further referred to as MoSe. The carbon alloyed coatings were deposited without (referred to as MoSeC0V) and with the application of DC substrate bias (named MoSeC50V). When used, the negative substrate bias voltage was set to 50 V. The deposition was performed in Ar atmosphere at a pressure of ~0.4 Pa. No additional substrate heating was

used. Furthermore, 2 deposition distances were used: 15 and 25 cm, resulting in a total of 6 coatings deposited. The number written after the name of the coating is related to the target-to-substrate distance (e.g. MoSe-15 is pure $MoSe_2$ coating deposited at a target-to-substrate distance of 15 cm). It should be noted that the deposition conditions were very similar to the ones used for the deposition of W-S-C coatings.

3.2 Process simulation

The origins of the compositional variations during the deposition of W-S-C on substrates placed at different locations in the deposition unit are: (i) the different scattering behavior of the sputtered species and, (ii) the preferential re-sputtering of the light sulfur atoms from the growing film. For better understanding, the scattering behavior of the sputtered species (W and S) and the level of the bombardment of the substrate with Ar neutrals were studied using two Monte-Carlo based software packages. The sputtering of the WS_2 target with Ar^+ ions was simulated using the SRIM (Surface and Range of Ions in Matter) 2013 software package [101]. The data from the SRIM software (angular and energy distribution) was used as an input for the SIMTRA software package [102], which simulates the transport of the sputtered species towards the substrates. The scattering behavior of the S and W atoms was simulated to obtain their flux at the different substrate locations used for deposition. For that purpose, 2 separate SRIM simulations were performed for getting the angular and energy distribution of W and S. The number of Ar^+ ions used was 10^6 and the incident energy was set to 600 eV (based on the typical target voltage during deposition of the coatings). The incident angle used was 0° (perpendicular to the target surface). The experimental chamber geometry used for the deposition was modeled in the SIMTRA software. In the simulation, the substrates have fixed positions while, during deposition, the substrates are passing in front of the targets. For a more realistic representation of the deposition process, 5 positions of every substrate location were modeled. The positions chosen are representing the approach and departure of the substrates in front of the target. The cylindrical substrates (diameter of 24 mm and a thickness of 8 mm) were modeled in the software. Only neutral Ar (p=0.4 Pa) was considered as background gas. For obtaining the arriving flux of S and W atoms, 10^6 and 5 x 10^5 atoms were used for the simulations, respectively. The geometry of the racetrack was also used as an input. A Molierre screened Coulomb interacting potential was used. The behavior of the Ar neutrals backscattered from the target was also simulated. For that purpose, the energy and angular distribution of the backscattered neutrals were obtained using the SRIM software package using Ar^+ ions interacting with an amorphous WS_2 target. The SIMTRA software package was used for analyzing the flux and the average energy of the backscattered Ar neutrals at the selected substrate locations. It is worth mentioning that the SIMTRA software package follows the particle trajectories until their energy drops to 0.0385 eV, after which the particles diffuse towards the surfaces. For the analysis, all particles that arrive at the substrates with the energy of 0.0385 eV are considered thermalized. Due to the different total number of particles

arriving at different locations, the results presented are a weighted average. The weighing was performed based on the total number of particles arriving at the respective positions. It should be noted that the software considers completely flat targets and substrates while, in reality, there is always roughness which can affect the deposition process. Additionally, a potential difference in the sticking coefficient of the arriving species was not taken into consideration.

3.3 Characterization of the coatings

3.3.1 Morphology

The morphological features were assessed using a field-emission scanning electron microscope (FESEM, Zeiss Merlin). Cross-sectional imaging was performed on a freshly cleaved coated Si wafer. The top surface was also observed on coated Si wafers. Secondary electron imaging was performed using an accelerating voltage of 2 kV. The typical magnification was 25-50 kx. The thickness of the coatings was also measured on the cross-sectional images. The wear tracks and the scratch tracks were imaged with the same FESEM, although higher accelerating voltages of 15 kV were used for performing simultaneous chemical analysis.

3.3.2 Chemical composition

The composition of the coatings was assessed using a wavelength dispersive spectroscopy detector (WDS, Oxford Instruments) attached to the FESEM. The analyses of the samples were performed after a suitable calibration using standards with known composition (from Micro Analysis Consultants). The INCA software by Oxford Instruments was used for the analysis. The accelerating voltage was 15 kV. Energy dispersive spectroscopy (EDS, Oxford Instruments X-Max) was used for the chemical analysis of the wear tracks as well as the scratch tracks. An EDS detector was also attached to the FESEM. The accelerating voltage was 15 kV and the data were obtained through the AZtec software (Oxford Instruments).

3.3.3 Crystal structure

The crystal structure was analyzed using grazing incidence X-ray diffraction (GIXRD). The experiments were performed on a Malvern Panalytical X'Pert MRD diffractometer (Figure 3-5) with Cu K_α (λ=1.5406 Å) radiation (voltage of 40 kV, current of 45 mA). The incidence angle was set to 3°. The scan range was from 10 to 90°, the step size was 0.025°, with a time per step of 3 seconds. The identification of the phases was performed through a comparison of the peaks with the International Center for Diffraction Data (ICDD) database.

Figure 3-5 Malvern Panalytical X'Pert MRD diffractometer

3.3.4 Microstructure

The microstructure was further analyzed using transmission electron microscopy, using either a JEOL JEM 2010 or a FEI Tecnai G2 equipment. Both microscopes use a LaB_6 electron emitter operating at an accelerating voltage of 200 kV. The samples were thin coatings (30-50 nm) deposited directly on carbon coated TEM grids.

3.3.5 Atomic force microscopy

The top surface morphology of the coatings studied in Chapter 7 was also evaluated using a Bruker Innova atomic force microscope. The measurements were performed in tapping mode using a Si tip (AppNano Acta) having a radius of < 10 nm, with a resonance frequency of 200-400 kHz and a spring constant of 13-77 N/m. The area of scanning was 2 x 2 µm. A 2D and 3D topographical images obtained from Mo-Se-C coatings are shown in Figure 3-6 a) and b), respectively. The average areal surface roughness (S_a) was obtained through the analysis. The data was processed using the Gwyddion 2.53 software [103].

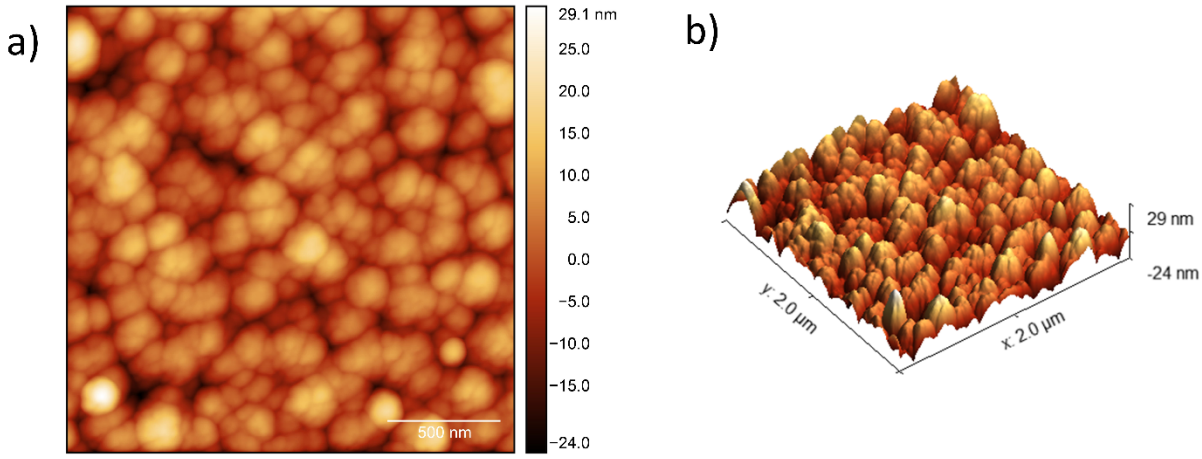

Figure 3-6 a) 2D topographical map and b) 3D topographical map from a Mo-Se-C coating

3.3.6 Raman spectroscopy

Raman spectroscopy was performed on either a Horiba XpLoRa or a Horiba LabRam HR800 spectrometer. The first one was utilized only for the studies reported in Chapters 4 and 5, while the latter was used for the studies in Chapters 6 and 7. In both cases an Olympus 100x objective was used (NA = 0.9), resulting in a spot size of ~1-2 µm. The XpLora device was equipped with a diode-pumped solid-state laser (532 nm) while for the LabRam device a He-Cd laser (441.6 nm) was used. The laser intensity was adjusted with the usage of appropriate filters, being the choice of the filter based on generating minimal damage to the coatings and the tribofilms, whilst, having a good signal-to-noise ratio. Fitting of the spectra related to the D and G bands of the carbon phase was performed using a Lorentzian lineshape for the D band and an asymmetric Breit-Wigner-Fano (BWF) lineshape for the G band, following the recommendations by Ferrari and Robertson [104].

3.3.7 X-ray photoelectron spectroscopy

To study the chemical bonding, X-ray photoelectron spectroscopy was performed, only on the coatings deposited in the lab-scale equipment (Chapter 4). A Kratos Axis Ultra HAS device utilizing monochromatic Al Kα X-rays (hν= 1486.6 eV) was used. The power of the X-ray source was set to 90W and a charge neutralizer was used during the acquisition. Survey spectra were obtained by setting the pass energy at 80 eV, with a step of 1 eV and a dwell time of 200 ms. For the high-resolution spectra of the regions of interest a pass energy of 40 eV, with a step of 0.1 eV and a dwell time of 600ms, was used. For removing native surface contamination, sputter etching was performed for 10 minutes using Ar ion gun operated at 2.2 keV and current density of 2.2 µA/cm2. The data acquisition was performed at pressures lower than 10^{-6} Pa.

Because of the presence of C in the films, charge correction for the binding energies was performed using the oxygen O1s peak (BE=530.6 ± 0.1 eV), from the high-resolution oxygen spectrum. Data fitting was performed using the CasaXPS software. The baselines of the spectra were achieved using the Shirley method and peak fitting was applied with Gaussian-Lorentzian functions.

3.3.8 Mechanical properties

The mechanical properties, namely the hardness, and the reduced Young modulus were measured by nanoindentation. A nanoindenter (NanoTest from Micromaterials) equipped with a Berkovich type indenter was used. The indentation was performed in load-control mode. The typical loads for the carbon alloyed coatings were 3-5 mN, resulting in an indentation depth within 10 % of the coatings, a depth at which no significant influence from the substrate is expected. Due to the very low hardness of the pure TMD coatings, the indentation was performed with 1 mN load, resulting in indentation depths of ~15 % of the coating thickness. For statistical analysis, 16 indentations were performed in 2 different zones. The results reported are the average. The reduced modulus was obtained through the analysis of the load-displacement curves following the method proposed by Oliver and Pharr [105]. A typical indentation curve is shown in Figure 3-7.

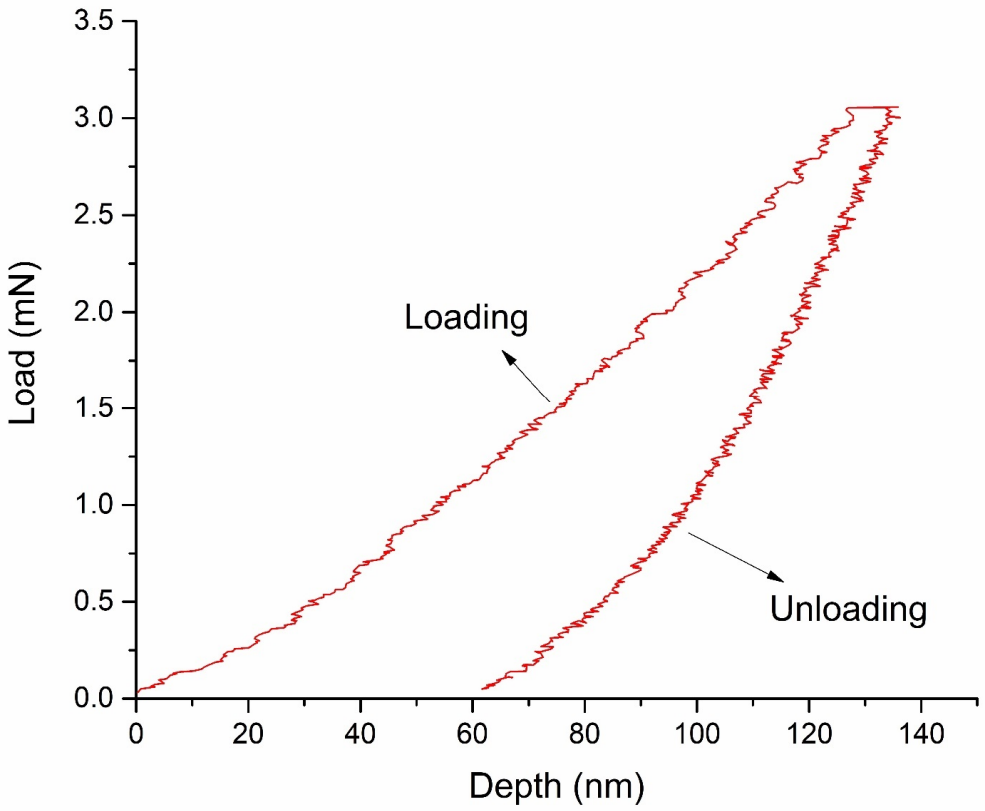

Figure 3-7 Indentation curve from a W-S-C coating

3.3.9 Adhesion

The adhesion of the coatings was analyzed using scratch testing (CSM Revetest, see Figure 3-8) and Rockwell C indentation, the latter also known as "Mercedes test". The latter method was only used for the Mo-Se-C coatings (Chapter 7). For the scratch testing, a Rockwell C indenter with a radius of 0.2 mm was used with the scratch speed set to 10 mm/min and a loading rate of 100 N/min (ISO 20502:2005 standard [106]). The scratch tracks were analyzed through optical microscopy with either a Leica DM4000 M LED microscope or a non-contact optical profilometer (Alicona Infinite Focus^{TM} G4). The three critical loads Lc_1, Lc_2, and Lc_3 are related to the first appearance of cracks, the initiation of chipping and spallation at the borders of the scratch track, and full delamination of the coatings, respectively. The occurrence of these critical events was also evaluated using SEM/EDS. The Rockwell C indentation followed the VDI 3198 standard [107]. The coatings were tested with a diamond Rockwell C indenter with a 150 kg of force (1471 N), and a dwell time of 15 s. The imprints were analyzed using SEM/EDS and an adhesion class was assigned to the coatings (HF1-HF6). HF1 class represents the best adhesion. The coatings having adhesion classes of HF1-HF4 are considered to have acceptable adhesion to the substrate.

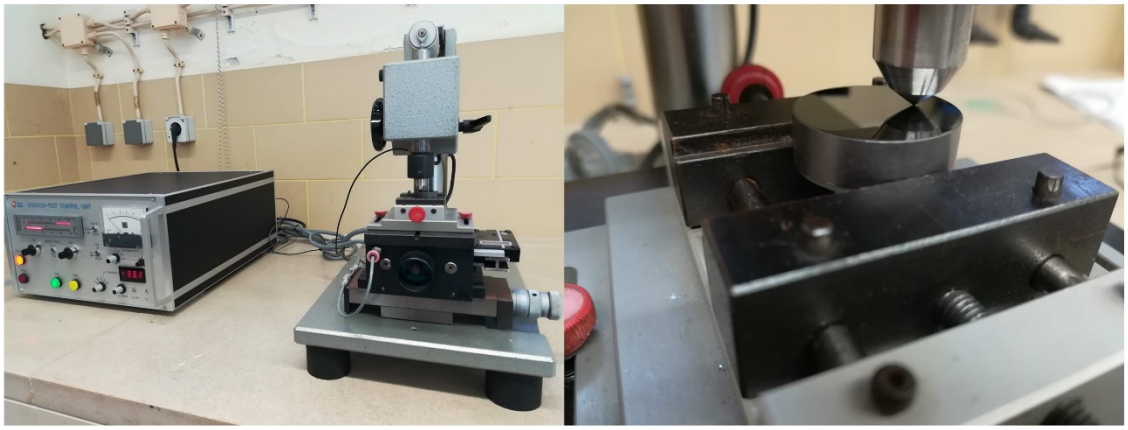

Figure 3-8 The CSM Revetest scratch tester (left) and close-up view of the sample and the indenter (right)

3.3.10 Tribological investigation

The lab-scale deposited W-S-C coatings (Chapter 4) were assessed on an in-house (CEMMPRE) developed unidirectional pin-on-disk tester. A DIN 100Cr6 bearing steel ball with a diameter of 10 mm was used as a counterbody. The normal load of 10 N was applied with calibrated dead weights. The sliding speed was set to 0.1 m/s. It should be noted that this sliding speed was always the same for the tribological testing, whatever the tribometer used. The duration of the test was limited to 2500 sliding cycles.

The tribological investigation performed on the W-S-C studied in Chapter 5 was performed at the Czech Technical University in Prague. The ambient, vacuum and dry N_2 tests were performed on a unidirectional pin-on-disk tester placed in a vacuum chamber (see Figure 3-9)

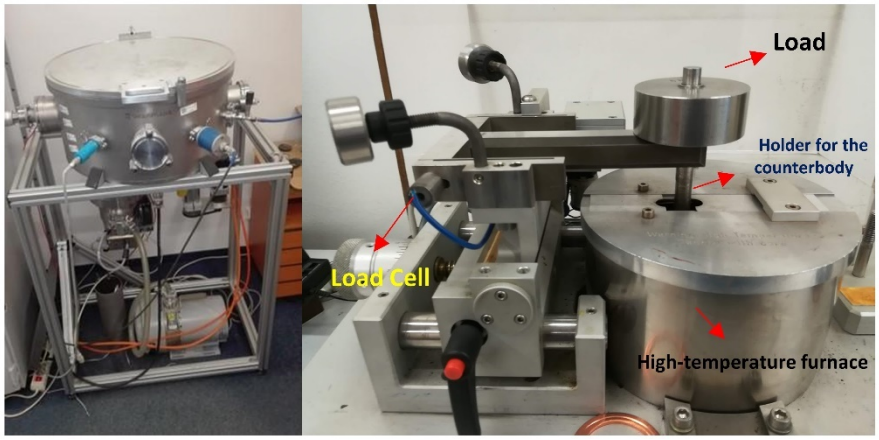

Figure 3-9 Vacuum tribometer (left) and the CSM high-temperature tribometer (right)

The ambient air tests (RT, T=23-25°C, relative humidity RH~30-45%) were performed with 2 different loads of 5 (initial maximum contact pressure of ~820 MPa) and 35 N (initial maximum contact pressure of ~1570 MPa).

The vacuum chamber was pumped by a turbomolecular pump backed by a dry scroll vacuum pump. Vacuum tests were performed at pressures lower than 10^{-3} Pa. Tests in nitrogen were performed by pumping the vacuum chamber to a pressure of ~10^{-3} Pa, and then, filling the chamber with high purity (99.999%) nitrogen to a pressure of 10^4 Pa. Vacuum and dry nitrogen testing were performed against uncoated and W-S-C coated 10 mm DIN 100Cr6 balls under a load of 2 N (initial maximum contact pressure of 605 MPa). Testing was performed for 10^4 sliding cycles unless otherwise noted.

Tribological tests at elevated temperatures (ambient air) were performed using a high temperature unidirectional pin-on-disk tester (CSM Instruments) shown in Figure 3-9. The dry sliding tribological testing was performed with a normal load of 5 N (initial maximum contact pressure of ~1154 MPa, at RT) with a 6 mm 100Cr6 ball used as counterbody. The testing temperature was set to 100, 200, 300, and 400°C. The maximum temperature was set at 400°C since previous studies have shown that coatings with similar composition and microstructure can only provide lubrication up to 400 °C. Steel based material, instead of a more thermally stable ceramic-based material, was chosen as counterbody, because it can better mimic the materials encountered in real applications (parts in combustion engines, workpieces in metal forming, sliding components in injection molding machines and sliding components in the aerospace industry).

Additionally, there is more data regarding the performance of self-lubricating thin films tested against bearing steel counterbodies, hence a comparison of the performance can be performed more easily. At 400°C, the hardness of the steel is still ~50 HRC. The duration of the test was limited to 5000 cycles. A test was also performed at room temperature with the other testing conditions kept the same to have a better comparison between RT testing and high-temperature testing. In both cases, the load was applied with dead weights. All the testing parameters are summarized in Table 3-1.

Table 3.1 Testing parameters for the tribological study performed in Chapter 5

Test parameters	Room temperature testing
Load [N]	5 N, 35 N
Speed [m/s]	0.1m/s
Duration [Number of cycles]	10000, 50000[a]
Counterbody	10 mm DIN 100Cr6 balls
Test parameters	High temperature testing
Load [N]	5 N
Temperature [°C]	RT, 100, 200, 300, 400°C
Speed [m/s]	0.1m/s
Duration [Number of cycles]	5000
Counterbody	6 mm DIN 100Cr6 balls
Test parameters	Vacuum and dry N_2 testing
Load [N]	2 N
Speed [m/s]	0.1m/s
Duration-Number of cycles	10000
Counterbody	Uncoated[b] and W-S-C coated 10 mm DIN 100Cr6 balls

[a] Tested only with 5 N

[b] Only in vacuum

The tribological tests for the W-S-C and Mo-Se-C coatings studied in Chapters 6 and 7 were performed using a reciprocating pin-on-disk tribometer (SRV™ 2, Optimol Instruments). The upper counterbody was a commercially available DIN 100Cr6 bearing steel ball with a 10 mm diameter. It was pressed against the coated disk with a load of 20N, resulting in initial maximum contact pressure of ~1.3 GPa. The bearing steel ball was oscillated at a frequency of 25 Hz, with a stroke of 2 mm, resulting in an average sliding

speed of 0.1 m/s. The oscillation of the upper counterbody is performed by an electromechanical drive. The load is applied through a spring deflection arrangement. The friction force is measured using a pair of piezoelectric load cells. The test duration was limited to 10 min (30000 cycles, one cycle being a single pass of the ball over the coating), or until a catastrophic failure occurs, indicated by a rapid increase of the coefficient of friction with values up to 0.5, accompanied by unusual noise and vibration (indicators for seizure proposed in the standard ISO 19291 [108]). The tests were performed at room temperature (23-25°C) with relative humidity (RH) of 30-45 %. Additional tests were performed under a continuous flow of dry N_2. It should be noted that the testing chamber is not hermetically sealed, and the RH during the testing under a continuous flow of dry N_2 measured by a precise hygrometer (Easy Log EL-USB-2, Lascar Electronics) was <7 %. Nevertheless, the RH in the proximity of the tribological contact should be lower as the flow of nitrogen is directed into the contact. Finally, tests were performed at an elevated temperature of 200°C, by heating the block on which the coated disk rests. To facilitate uniformity, the heating was performed while both counterbodies are in contact.

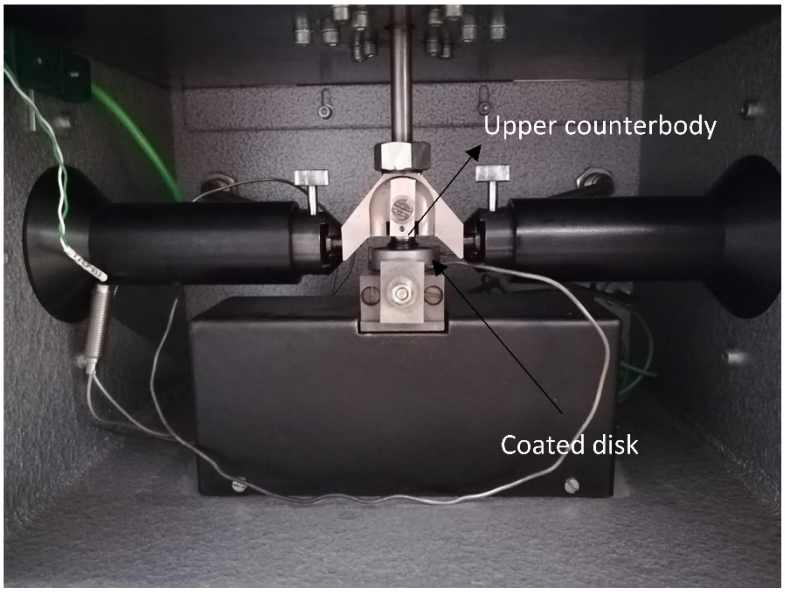

Figure 3-10 Optimol SRV 2 tribometer

The specific wear rate (mm^3/Nm) was calculated as the wear volume (V_w) divided by the normal load (F_n) and the sliding distance (s), see (Eq 3.1) [109].

$$W_r = \frac{V_w}{F_n \cdot s} \tag{3.1}$$

The wear volume of the spherical counterbodies was considered to be a spherical cap and it was calculated using the following expression:

$$V = \left(\frac{\pi h}{6}\right)\left(\frac{3d^2}{4} + h^2\right) \quad (3.2)$$

Where h is the height of the cap calculated as:

$$h = r - \sqrt{r^2 - \frac{d^2}{4}} \quad (3.3)$$

Where d is the scar diameter and r is the radius of the ball.

The wear volume of the coatings studied in Chapter 4 was evaluated using a 2D profilometer (Mahr Perthometer S4P) with an optical head (Focodyn). Four cross-sectional profiles were acquired from different areas across the circumference of the wear track, the area under the profiles was calculated and multiplied with the circumference of the wear track.

The wear volumes of the coating studied in Chapter 5 were obtained using a Zygo NewView ™ 7300 scanning white light interferometer.

The wear rates for the coatings assessed in Chapters 6 and 7 were obtained using an Alicona InfiniteFocus™ 3D profilometer. A 100x objective was used, resulting in a vertical resolution of ~20 nm. Three profiles were acquired from three different zones of the wear scars, the areas under the profile were calculated and multiplied with the stroke length to obtain the wear volume.

The scar diameter of the spherical counterbodies was measure using the Alicona 3D profilometer, except for the studies in Chapter 5 where the Zygo device was used

Chapter 4 The effect of the deposition procedure on the compositional, structural and mechanical properties of W-S-C(H) coatings deposited by RF magnetron sputtering

In this chapter, W-S-C(H) coatings deposited by 4 different procedures were studied in terms of their composition, structure, mechanical and tribological properties. This study was undertaken since it was not clear how various deposition routes affect the properties of the deposited coatings. The results will be further used to choose the best route for the deposition of self-lubricant TMD-C coatings in semi-industrial conditions. This work resulted in the publication of the following paper:

Vuchkov, T.; Yaqub, T.B.; Evaristo, M.; Cavaleiro, A. Synthesis, Microstructural, and Mechano-Tribological Properties of Self-Lubricating W-S-C(H) Thin Films Deposited by Different RF Magnetron Sputtering Procedures. *Coatings* **2020**, *10*, 272.

4.1 Chemical composition, morphology, and structure

The elemental composition of the deposited films is shown in Table 4.1. The hydrogen content of the reactively sputtered films was not considered; the results presented for the hydrogenated coatings show the sum of C, W, S, and O being 100 at. %. Changing the power applied to the carbon target, the number of pellets, or the partial pressure of the CH_4 gas affected the C contents of the coatings. The oxygen content is up to 12 at. %, and the highest values for the co-sputtered coatings are probably a result of the target contamination, residual oxygen present in the chamber, and longer deposition times (3 h compared to 1–2 h used for the other methods).

The sulfur to tungsten ratio (S/W) is of great importance in these films as it can affect the tribological performance [80]. The values (1.6–1.7) for the co-sputtered coatings are in agreement with previous studies performed on co-sputtered W-S-C coatings deposited by separate targets using the same equipment [85]. The S/W ratio for the coatings deposited by sputtering a composite target ranged between 1 and 1.7, depending on whether the deposition was carried out in stationary or intermittent mode. Reactively sputtered films (D4) also showed a lower S/W ratio, with values between 1.23 and 1.5.

Table 4.1 List of coatings deposited, chemical composition and deposition rate

Type of Coating	Chemical Composition (at. %)				S/W Ratio	Thickness (µm)	Deposition Rate (nm/min)
	C	S	W	O			
D1-300W	37.6 ± 0.2	31.4 ± 0.3	19 ± 0.2	12 ± 0.3	1.62	1.6	9
D1-450W	42.5 ± 0.4	29.5 ± 0.1	20 ± 0.2	8 ± 0.2	1.48	1.4	7
D1-600W	47.1 ± 0.1	26.9 ± 0.6	16 ± 0.1	10 ± 0.1	1.68	1.9	11
D2-21p	22 ± 0.1	47 ± 0.1	26.9 ± 0.2	4.1 ± 0.1	1.74	2.8	24
D2-17p	25.5 ± 0.1	44.8 ± 0.3	26.3 ± 0.1	3.4 ± 0.1	1.72	2.6	22
D2-13p	34.4 ± 0.1	37.6 ± 0.5	24.5 ± 0.1	3.5 ± 0.3	1.54	2.2	18
D3-21p	31.3 ± 0.7	37 ± 0.4	26 ± 0.5	5.7 ± 0.1	1.42	1.6	27
D3-17p	38.5 ± 0.3	31.4 ± 0.1	25 ± 0.2	5.1 ± 0.1	1.25	1	17
D3-13p	49 ± 0.3	22.9 ± 0.1	23.3 ± 0.1	4.8 ± 0.2	0.98	0.7	12
D4-28%	47.9 ± 0.1	28 ± 0.1	18.8 ± 0.6	5.3 ± 0.2	1.50	0.5	8
D4-38%	51.4 ± 0.1	24.9 ± 0.2	19.1 ± 0.1	4.6 ± 0.3	1.30	1.1	9
D4-48%	58.8 ± 0.3	19.5 ± 0.1	15.8 ± 0.1	5.9 ± 0.5	1.23	0.7	11

Three mechanisms are generally cited for understanding the compositional variations obtained during magnetron sputtering of TMDs:

- Different scattering behaviors of sputtered atoms during their travel towards the substrate [110];
- Preferential re-sputtering of the sulfur atoms from the growing film as a result of energetic particle bombardment [111];

- The reaction of the sputtered species with the process gas and subsequent pump-out [85].

A significant S deficiency was observed for the D3 and D4 families of coatings. The low S/W ratio is, very likely, due to both the difference in scattering behavior as well as the bombardment with backscattered Ar neutrals. The sputtered species, C, S, and W will have different scattering behaviors during their travel towards the substrates. The lighter elements, C and S, will be deflected to a greater extent as a result of collisions with the Ar gas in the chamber. The W atoms, which are much heavier, will have straight traversing paths towards the substrates. In this context, it is expected that the D2 coatings will be richer in the lighter elements, as the probability of arrival of the species that scatter more will be higher when the substrate holder is rotating. On one hand, this was observed for S, as the S/W ratio was higher for the D2 coatings compared to the D3 coatings. On the other hand, the C content was lower, indicating that the mechanism of preferential re-sputtering should also be considered. The energy of the backscattered Ar neutrals is proportional to the target voltage. The target voltage for the D2 coatings was higher (~800 V) compared to the D3 ones (~500 V), indicating that the energy of the backscattered Ar neutrals will be higher in the D2 case. Although the energy of the backscattered Ar neutrals is higher for the D2 coatings, these coatings still had a higher S/W ratio. Considering the lower S/W ratio and the higher carbon content of the D3 coatings, it is very likely that they are subjected to a higher flux of backscattered Ar neutrals with high energy. One of the parameters that should also be considered in this case is the substrate location. As the target-to-substrate (TSD) distance is constantly changing for the D2 case, when the substrates are further away from the target there will be the arrival of the lighter sputtered species that scatter more in the chamber (C and S), while the energetic argon neutrals will have significantly lower energy due to an increased number of collisions. In this context, it is expected that D2 coatings will have higher S contents. The increased carbon content for the D3 coatings is very likely because of the lower sputtering yield of carbon.

The lower S/W ratio for the D4 coatings (deposited in reactive mode) may be further caused by the reaction of the sputtered S atoms with the H present in the chamber, and formation of H_2S gas and, subsequently pumped-out. The bombardment with backscattered Ar neutrals was also amplified since the introduction of the reactive gas causes target poisoning, evident from the observed increase in the target voltage. The target voltage values varied between 1100 and 1200 V, with increasing partial pressure of methane. For higher target voltage, the generation of backscattered Ar neutrals with much higher energy is enhanced.

Cross-sectional and top-view SEM micrographs for selected thin films are shown in Figure 4-1. The films generally have a compact morphology. Some porosity and signs of columnar growth can be observed for the D2-17 coating, which has a rather low amount of C (26 at. %). All the other cross-sectional micrographs present compact and featureless morphologies. Top-view micrographs show cauliflower-like structures. This morphology is typical for films deposited by magnetron sputtering under the influence of the atomic

shadowing effect. It should be mentioned that the cauliflower features are not evident for the coating deposited in reactive mode (see Figure 4-1h), and the micrographs reveal a smoother morphology. The smoothening is very likely due to the increased bombardment of the growing film with reflected Ar neutrals since the energy (proportional to the target voltage) of the backscattered Ar neutrals is the highest in this case. Bombardment of the growing film with energetic species increases the adatom mobility and thus reduces the atomic shadowing effect [112].

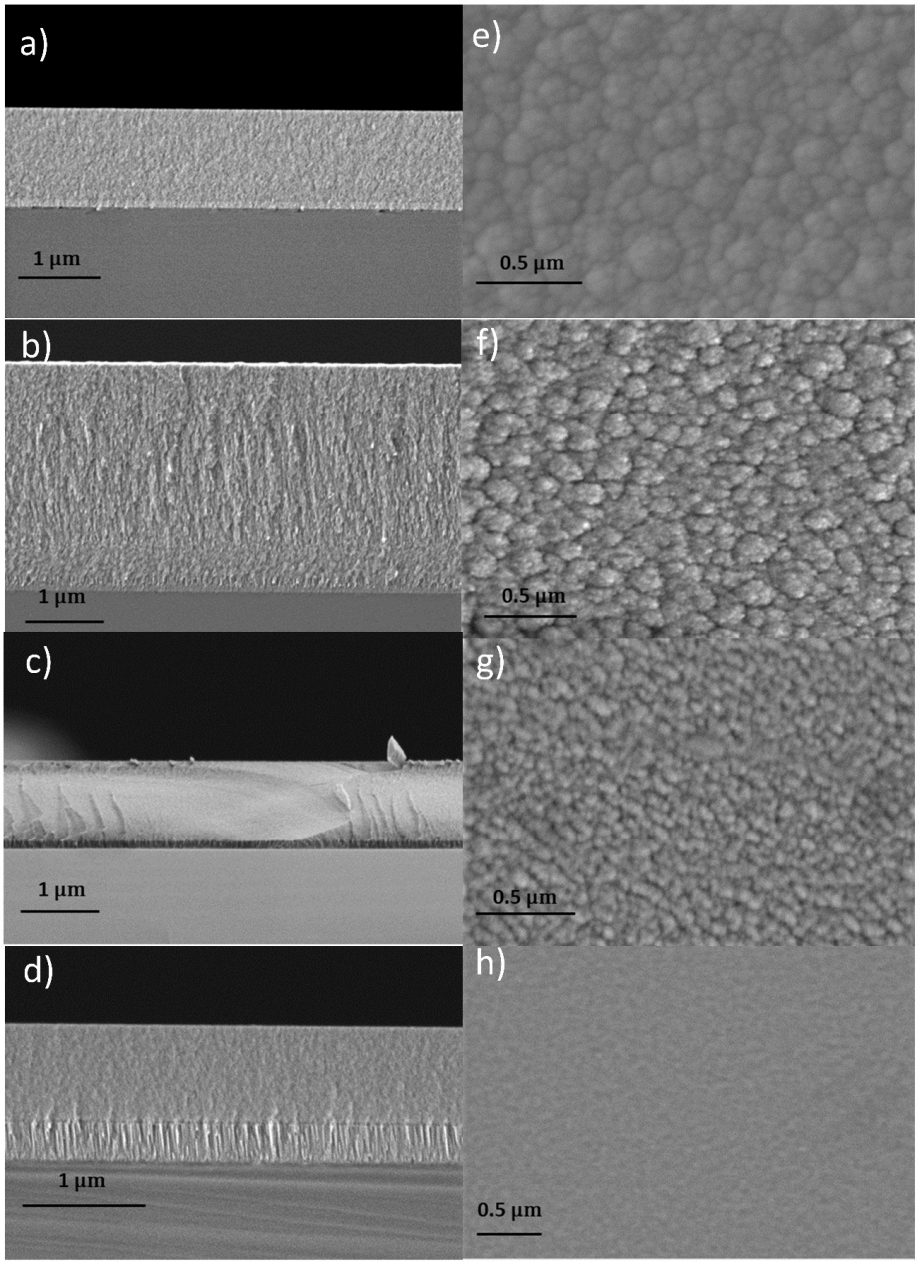

Figure 4-1 Cross-sectional SEM micrographs of: (a) D1-450; (b) D2-17; (c) D3-17; (d) D4-38; and their respective top-surface morphologies (e) D1-450; (f) D2-17; (g) D3-17; (h) D4-38

GIXRD results are shown in Figure 4-2. Common to all patterns is the presence of a broad peak starting at 2θ~33°, which is associated with the (100) peak of WS_2 (ICDD card no. 00-008-0237), with a tail towards higher angles representing a turbostratic stacking of the (10l) family of WS_2 planes with l = 1.2.3 [113]. Only the D2 films with low carbon contents have a sharper (100) peak and an additional (110) peak at 2θ = 59°. A small contribution of the (20l) family of planes with l = 0, 1, 2, 3 at 2θ~70° is also detected for these coatings. The small (002) reflection from the WS_2 phase (indicating the presence of basal planes closely parallel to the substrate) at 2θ~14° can only be seen on the pattern of the D2-21 film. The Cr peak observed in the D3 and D4 films stems from the interlayer. The presence of tungsten carbides is difficult to detect from the XRD patterns as there are several W_2C and WC_{1-x} related peaks in the region of 2θ = 34.5–39° (ICDD card numbers: 00-035-0776, 00-020-1316) overlapping with the (10l) family of planes for WS_2. Some of the peaks often observed for magnetron-sputtered WC/a-C films are W_2C (100) at 2θ = 34.5°, W_2C (002) at 2θ = 38°, and WC_{1-x} at 2θ = 37° (see ref. [114,115]), with the authors of these previous studies reporting a broad peak in the range of 2θ = 34.5–39°.

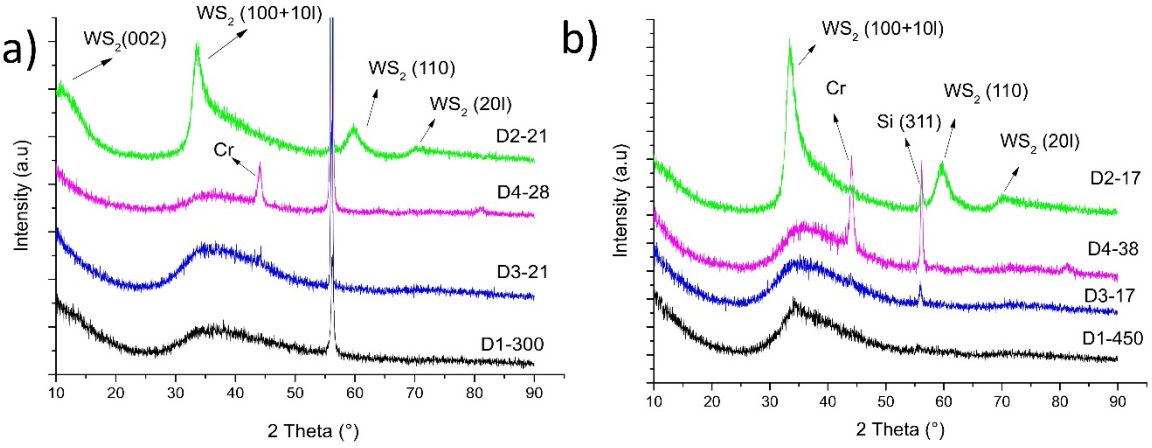

Figure 4-2 GIXRD diffractograms for the coatings deposited by each deposition route: (a) lowest C content; (b) intermediate C content

4.2 Chemical bonding

To reach a better understanding of the chemical bonding in the coatings, XPS and Raman spectroscopy were performed on selected coatings from every deposition route. XPS spectra from the carbon region of interest, after sputter cleaning of the samples, are shown in Figure 4-3. Spectra before etching (not shown) generally consisted of the main carbon peak at binding energy (BE) of 284.5 eV, which was identified as a C-C bond originating from the presence of adventitious carbon. The presence of adventitious carbon was

confirmed by the presence of C-O bonds at a BE of 286 eV and C=O bonds at 288 eV. A small contribution from C-W bonding was also observed at the typical location of ~283–283.3 eV [116]. Fitting of the spectra obtained after etching (see Figure 4-3) is performed using two peaks, except for the spectrum obtained for the D4-48 coating, for which an additional peak was added at higher binding energy to complete the fitting, which was identified as C-O bonding. Fitting was constrained by setting the maximum values of the full width at half maximum (FWHM) to 1.2 eV, with the location of the C-C bonding originating from the a-C phase being positioned at a BE location higher than 284.4 eV, and with the C-W bonding set to a BE location lower than 283.3 eV [115,117]. This fitting procedure resulted in a low standard deviation of the residuals. Bonding of C-W type was observed for all coatings. A major trend observed in the spectra is the dominance of the C-W bonding type for the coatings with low amounts of C (e.g., D2, D3-21). Increasing the C contents of the coatings results in larger areas for the peak related to C-C bonding (e.g., D1-450, D4-38), indicating the existence of increasing amounts of a-C. These trends were also observed for WC/C [117] and TMD-C [118] coatings in previous studies.

The spectra acquired from the W4f region of interest can be seen in Figure 4-4. The spectra before sputter cleaning were quite similar, and only one is shown as a reference (Figure 4-4 a)). For the spectra after sputter cleaning, a representative one of a coating from each deposition route is shown in each case. Spectra acquired before sputter cleaning of the samples show strong features at higher binding energies, indicating the presence of tungsten oxides. The fitting was performed by setting the separation between the energy of the $W4f_{7/2}$-$W4f_{5/2}$ doublet to 2.18 eV, with the peak area ratios between $W4f_{7/2}$ and $W4f_{5/2}$ peaks set to 4/3 [119]. A total of four doublets were used to fit the spectra acquired before sputter cleaning. The location of the doublets is further indicated by the location of the $W4f_{7/2}$ peak. The location of the first doublet is at a BE of 32 ± 0.1 eV for all coatings, a value which is lower than the typical one of W-S bonding in WS_2, often reported at 32.6–32.8 eV [120,121]. Considering this location, this peak is identified as W-C bonding. The second peak at a BE of 32.6 ± 0.1 eV originates from W-S bonds in WS_2. The peak at 33.6 ± 0.2 eV is associated with W-O bonds in a sub-stoichiometric WO_x compound. The final doublet with the $W4f_{7/2}$ at 35.6 ± 0.1 eV is in excellent agreement with the reference values for WO_3 [116,119,121,122]. A single peak was also used at BE 37–38 eV, which represents the $W5p_{3/2}$ peak. Spectra obtained after sputter cleaning were fitted using three doublets. The main doublets are shifted towards lower binding energies compared to the spectra obtained before sputter cleaning. The location of the first doublet is at a BE of 31.7 ± 0.1 eV, which is in the typical range (31.5–32 eV) for W-C bonds presented in the literature [115,117]; the identification of C-W bonds in the C1s spectra confirms the W-C bonding assignment from the W4f spectrum obtained after sputter cleaning. The second doublet at a higher binding energy of 32.1 ± 0.1 eV was identified as W-S bonds in a sub-stoichiometric WS_x compound. A shift towards lower binding energy of the W4f peak representing W-S bonding is expected, which is a result of the preferential sputtering of

the chalcogen atom (S in this case) during sputter cleaning of the samples [123]. The third doublet added at a BE of 33-33.2 eV represents W-O bonding in WO_2. To finalize the fitting, a broad $W5p_{3/2}$ peak was added at a BE of 37–38 eV. The intensity of the third doublet might be exaggerated as the fitting of W-S bonding and W-C bonding should be performed by asymmetric lineshapes, with asymmetry towards higher binding energy. As a result of the interaction between the core-hole and conduction electrons, XPS core-level spectra of metals are often fitted with asymmetric lineshapes, with pronounced asymmetry towards higher binding energies (e.g., Doniach–Sunjic lineshape) [116,124–126]. In a recent XPS study on tungsten carbide nanopowders, Krasovskii et al. [116] reached a good fit on the W4f core-level spectra using asymmetric lineshapes representative of W-C bonds, with asymmetry towards higher binding energy. The high-resolution core-level W4f XPS spectra of WS_2 powder performed by Morgan [120] were also fitted using asymmetric lineshapes representative of W-S bonding. The introduction of asymmetric lineshapes for fitting the spectra will significantly increase the complexity of the fitting procedure because of the additional fitting parameters; therefore, fitting was performed using symmetric Gaussian–Lorentzian lineshapes.

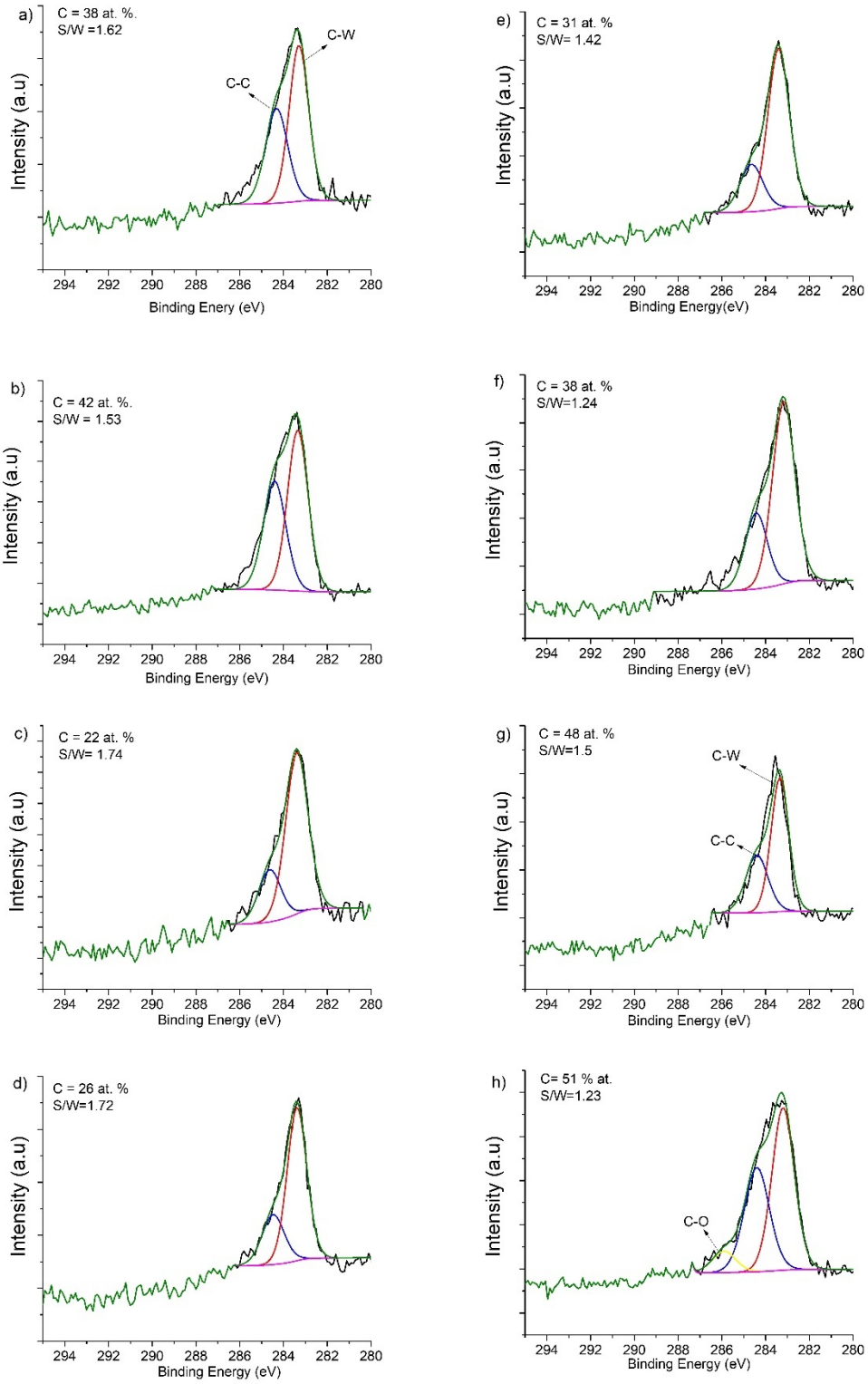

Figure 4-3 XPS spectra acquired in the C1s region of interest after sputter cleaning: (a) D1-300; (b) D1-450; (c) D2-21; (d) D2-17; (e) D3-21; (f) D3-21; (g) D4-28; (h) D4-38.

Raman spectra of selected coatings representing each route of deposition in the range 100–2000 cm^{-1} are presented in Figure 4-5. Magnetron-sputtered TMD-C films generally have two regions, with features representing different phases in the film. The first region at Raman shift values of 300-450 cm^{-1} represents the TMD phase. For WS_2, there are two distinct peaks, the peak at 350 cm^{-1} related to the in-plane phonon mode $E^1_{2g}(\Gamma)$, while the peak at 412 cm^{-1} represents the out-of-plane phonon mode $A^1_g(\Gamma)$ [127]. Distinct peaks related to the WS_2 phase can be observed for the D2-17 coatings. These features are in agreement with the XRD results. The coatings with higher carbon contents (representative spectra are shown from the D1-450 and D4-38 coatings) show more featureless spectra in the WS_2 region of interest, confirming the poor crystallinity of the WS_2 phase.

The second region between 1100 and 1800 cm^{-1} contains the D and G bands of carbon. These peaks were fitted using a Breit–Wigner–Fano lineshape for the G peak and a Lorentzian lineshape for the D peak, as proposed by Ferrari and Robertson [104]. The fitting resulted in ratios of the intensity of the D and G peaks (I_D/I_G) having values in the range 0.8–1.1. The location of the G band was typically below 1580 cm^{-1}. Considering these values, and according to the four-stage model proposed by Ferrari and Robertson, the carbon phase is in the second stage as amorphous carbon with predominant sp^2 bonds and a minor presence of sp^3 bonds.

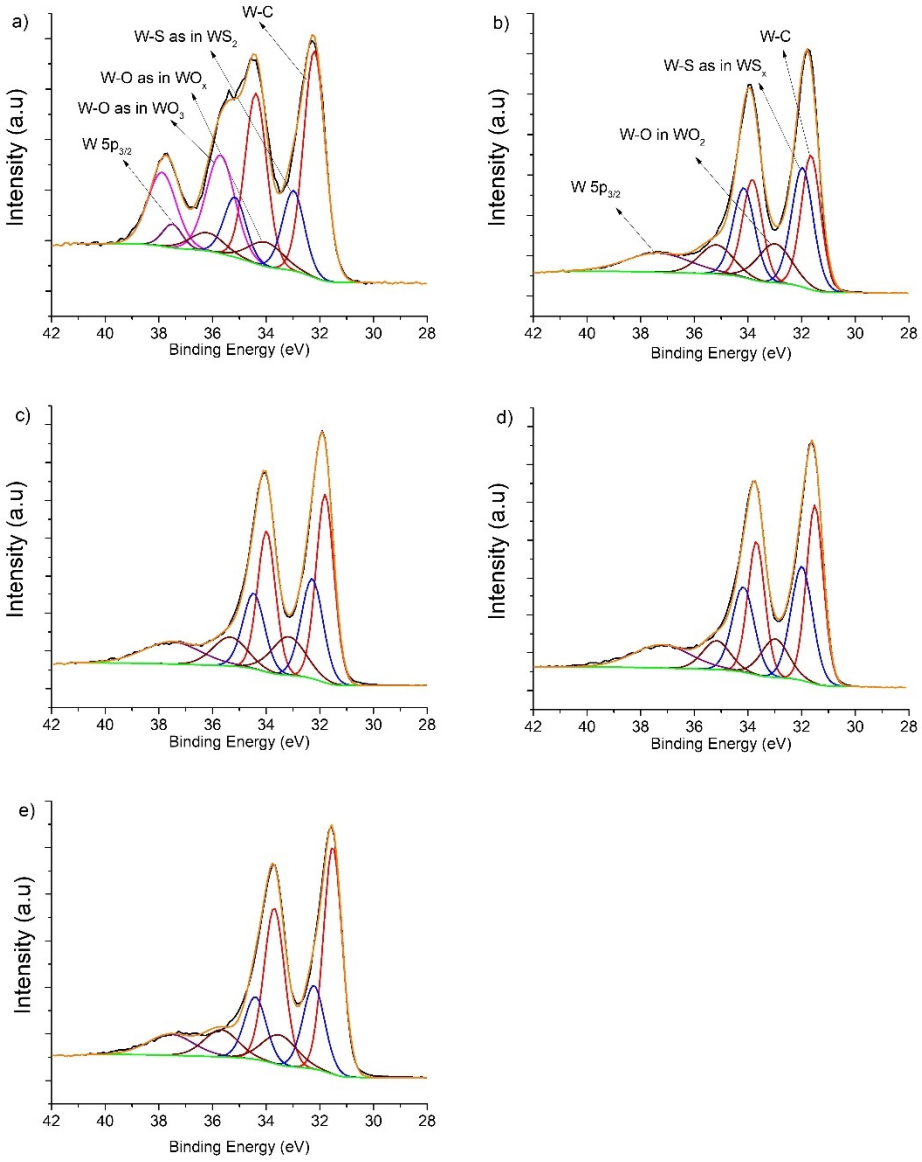

Figure 4-4 XPS spectra obtained in the W4f region of interest: (a) D1-450 before etching; (b) D1-450 after etching; (c) D2-17 after etching; (d) D3-17 after etching; (e) D4-38 after etching.

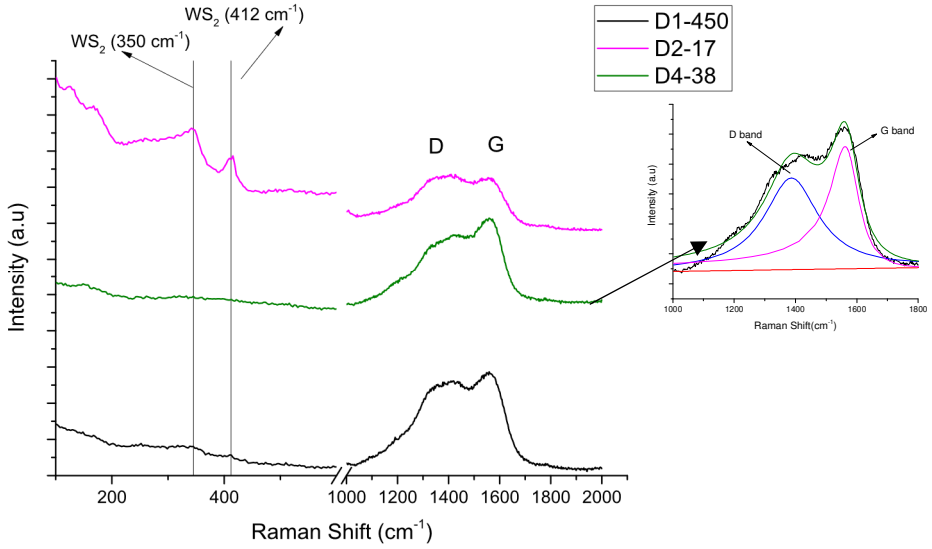

Figure 4-5 Raman spectra acquired from representative coatings.

4.3 Mechanical Properties

The hardness results from nanoindentation experiments are shown in Figure 4-6 and Table 4.2. The horizontal axis shows the power to the carbon target, the number of pellets used for deposition, or the partial pressure of the CH_4 gas, depending on the deposition procedure.

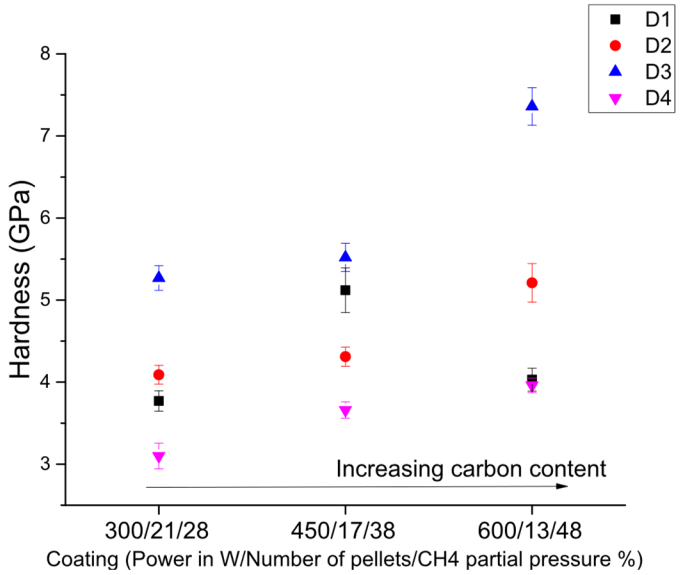

Figure 4-6 The hardness of the coatings.

The highest hardness was measured for the coatings deposited by sputtering a composite target in the stationary mode (D3), followed by the films deposited by co-sputtering (D1), and sputtering a composite

target in intermittent mode (D2). The coatings deposited in reactive mode generally showed lower hardness. The D3 coatings are harder compared to the D1 coatings, although they contain lesser amounts of carbon. The higher hardness is very likely because of the lower S/W ratio, which can be indicative of increased amounts of harder WC inclusions. The increased presence of WC is further supported by the higher peak area ratio between the C-W and C-C peaks in the C1s spectra for the D3 coatings as compared to the D1 ones (for example, compare Figure 4-3 e) and Figure 4-3 a)). Additionally, these coatings deposited with the stationary holder in front of the target are subjected to higher bombardment with reflected Ar neutrals. In this context, it is expected that these coatings are more compact and, hence, harder. The lower hardness for the reactively sputtered coatings can be related to the hydrogenation of the a-C phase, as hydrogenated carbon coatings are often softer compared to their hydrogen-free counterparts [128]. The hardness values generally follow increasing trends concerning the C content, except for the co-sputtered coating (D1-600) with the highest C content (~48 at. %), which has a lower value compared to the coating with 42 at. % C (D1-450). The presence of higher C contents improves the compactness of the coatings, resulting in higher hardness. A pure carbon coating deposited using the same equipment has a hardness of ~8 GPa [129]. The higher hardness of D1-450 compared to its counterpart (D1-600), with a higher C content, can be associated with its lower S/W ratio. The lower S/W ratio can be related to an increased presence of harder WC inclusions.

Scratch scar optical micrographs are shown in Figure 4-7. The scratch testing was performed starting at 5 N of load up to a maximum load of 40 N. A single scar from each deposition route is shown since the features observed were quite similar between the coatings deposited by the same deposition route. The results associated with the critical load are presented in Table 4.2. Lc_1 corresponds to the first appearance of cracks on the edge of the scratch scar. The critical load of the Lc_2 type corresponds to the first delamination (chipping) occurring at the sides of the scratch scar, while the Lc_3 critical load is the load at which the coating is removed from the surface [130]. Coatings of D1 and D2 types showed adhesion failures with Lc_3 critical loads of 14 N (for D1-450) and 13 N (for D2-17). Lc_1 and Lc_2 loads were not detected (no cracking or chipping on the sides of the scar was observed) in these cases. As soon as loads of 13-14 N were achieved, gross spallation was observed. The failure mode for these coatings was identified as wedge spallation.

The D3 and D4 coatings showed an improved adhesion. Cracking was observed for the D3 coatings as well as for the D4 coating deposited under the lowest partial pressure of CH_4. The Lc_1 loads were in the range of 12–19 N for the D3 coatings and ~11 N for the D4-28 coating. A representative detail regarding the cracking observed is shown in Figure 4-7e. The Lc_2 loads (a representative detail is shown in Figure 4-7f)

were between 20 and 28 N for D3 coatings, and 19 and 21 N for the D4 ones. It should be noted that no complete removal of the coating occurred in the current load range for the D3 and D4 coatings.

The deteriorated behavior for D1 coatings can be related to the absence of an interlayer. Delamination of the coating from the substrate, in this case, is very likely due to the bonding type mismatch between the coating and the substrate. As for D2 coatings, the spallation is most probably due to the columnar morphology, which is more porous by nature, with the presence of columnar boundaries. Columnar boundaries are unfavorable in terms of crack initiation and propagation and, hence, the films are more prone to spallation. The improved behavior for D3 and D4 films is associated with the compact featureless morphology and the presence of the Cr interlayer.

Table 4.2 Mechanical properties and adhesion of the coatings

Coating	Hardness [GPa]	Reduced Modulus [GPa]	Critical Load Lc1 [N]	Critical Load Lc2 [N]	Critical Load Lc3 [N]
D1-300	3.8 ± 0.1	63.1 ± 1.3			19 ± 1
D1-450	5.1 ± 0.3	60 ± 1.6			14 ± 2
D1-600	4.0 ± 0.1	44.63 ± 1.2			13 ± 2
D2-21	4.2 ± 0.1	55.9 ± 2.1			7 ± 1
D2-17	4.3 ± 0.1	60.8 ± 1.1			13 ± 1
D2-13	5.2 ± 0.2	62.3 ± 1.4			7 ± 1
D3-21	5.3 ± 0.1	86 ± 1.6	12 ± 1	22 ± 1	> 40
D3-17	5.5 ± 0.2	88 ± 1.2	21 ± 1	28 ± 3	> 40
D3-13	7.4 ± 0.2	97 ± 2.6	16 ± 1	20 ± 1	> 40
D4-28	3.1 ± 0.2	61.7 ± 2.7	11 ± 1	21 ± 1	> 40
D4-38	3.7 ± 0.1	61 ± 1		20 ± 1	> 40
D4-48	4 ± 0.1	84.3 ± 2		19 ± 1	> 40

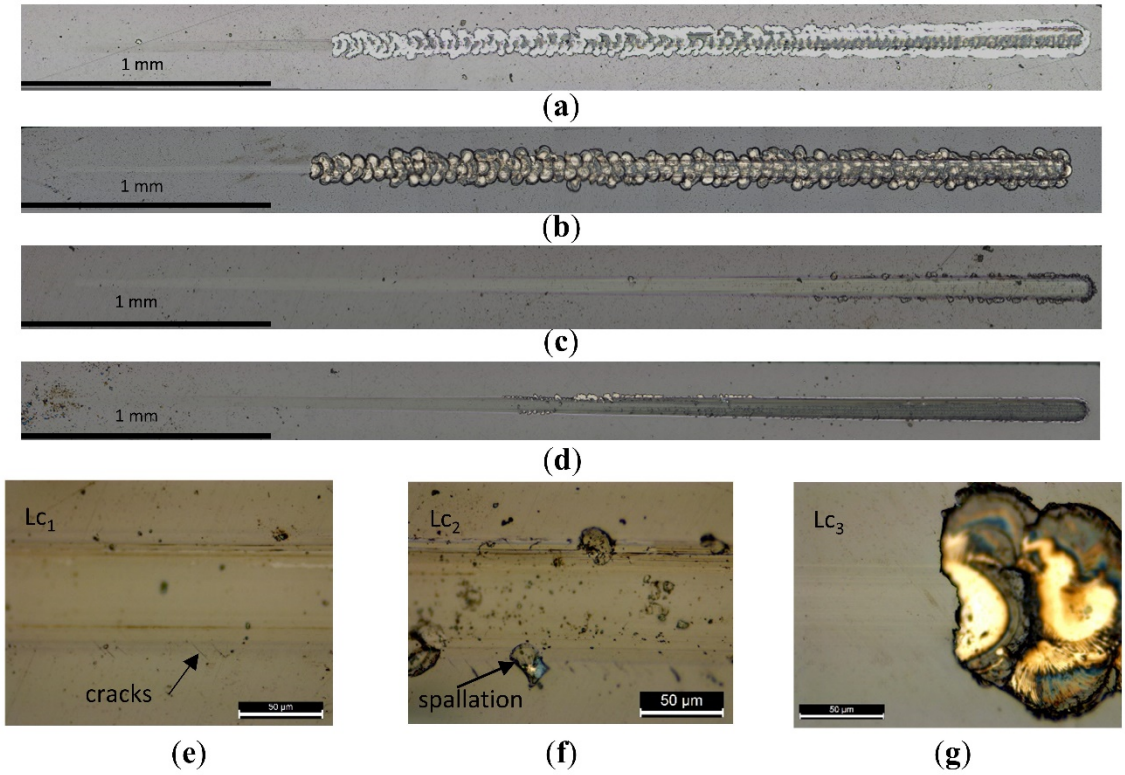

Figure 4-7 Scratch scars optical micrographs: (a) D1-450; (b) D2-17; (c) D3-17; (d) D4-38; (e) Lc1 detail acquired from the D3-17 scratch scar; (f) Lc2 detail from the D3-13 scar; (g) Lc3 detail from the D2-17 scar.

4.4 Tribological properties

Results from the tribological tests are shown in Figure 4-8. A coating with intermediate carbon content was selected from each deposition process.

The coating deposited by co-sputtering (D1-450) showed a running-in period with a drop of friction coefficient to ~0.06 at ~800 cycles; furthermore, fluctuations at values around 0.06–0.08 are observed for ~500 cycles, followed by an increase in friction, indicating a potential failure of the coating. The 2D profilometry presented wear depths of ~1.5 µm, a value which is close to the thickness of the coating. The optical micrograph obtained for the wear scars displayed large delaminated areas (see Figure 4-9 a)). The wear rate of the coating was the highest, with a value of 1.5×10^{-5} mm^3/Nm. The drop of the friction down to 0.06 indicates a potential presence of a TMD tribofilm at the sliding interface, but the inability to deposit an interlayer is probably crucial as rapid wear of the coating occurs, which can be related to its poor adhesion to the substrate (large delaminated areas are observed on the wear scar). The behavior of the D2-17 coating is slightly different, with a short running-in period, after which the friction coefficient dropped to 0.09-0.1, followed by a small increase and stabilization of the friction coefficient at a value of ~0.11–0.12. The specific wear rate was ~ 5×10^{-6} mm^3/Nm, a much better value compared to the D1-450 coating.

The optical micrograph (see Figure 4-8c) showed areas on the wear scars in which the coating is worn through, but not to the same extent as the D1-450 coating. The coating D3-17 shows the best performance as the coefficient of friction was quite low, dropping to ~0.06 in the first ~700 cycles, with fluctuations between 0.06 and 0.08 for the remaining time of the test. This coating also outperformed the other coatings in terms of wear resistance, with a specific wear rate of 3×10^{-6} mm^3/Nm. The optical micrograph (Figure 4-8e) of the wear scar does not show any signs of delamination. The reactive sputtered coating (D4-38) had a higher friction coefficient compared to the other coatings, with a starting value of 0.16, a value that steadily dropped to ~0.12 by the end of the duration of the test. The integrity of the coating was preserved during testing (see Figure 5-8g), with a specific wear rate of ~ 4×10^{-6} mm^3/Nm.

In terms of ball wear, higher values were observed for the D1 and D3 coatings (~ 1×10^{-8} mm^3/Nm). The higher wear for the ball counterpart sliding against the D1 coating is very likely due to the increased interaction of the ball with the harder steel counterpart, further resulting in the generation of an iron-rich third body, which can cause three-body abrasion. This process will result in an increased coefficient of friction as the iron-rich debris does not possess low shear strength. As for the ball sliding against the D3 coating, the increased wear may be due to the increased hardness of the D3 coating. The harder D3-17 coating most probably contains more WC inclusions, which are very hard and can cause abrasive wear on the steel counterpart. In the case of the D2 and D4 coatings, the formation of a protective transfer film results in reduced wear of the counterbody.

Considering the low value observed for the friction coefficient (~0.06–0.08) in the D1-450 and D3-17 coatings, it can be assumed that the friction is at least partially governed by a WS_2 phase. It should be noted that pure carbon films deposited using the same equipment, sliding against a steel counterbody, under similar conditions, show a coefficient of friction of ~0.2 (see Ref [129]). The D2-17 coatings, despite having a significant amount of WS_2, showed a higher coefficient of friction, which may be related to the partial interaction between the steel counterbody and the steel disk due to the presence of areas on the wear track where the W-S-C coating was delaminated. In the case of the reactively sputtered coatings, the friction was slightly higher but stable. Considering the high amount of C in the coating, and the higher overall friction coefficient, it is very likely that the carbon phase plays the main role in governing the friction.

In summary, the best performance was observed for the coating deposited by sputtering a composite target with the substrate holder being stationary (D3). Its good performance may be related to the compact morphology resulting from the optimal carbon content and a suitable S/W ratio. Moreover, the coating responded well to scratch testing, with the highest value of the Lc_2 load and no gross delamination.

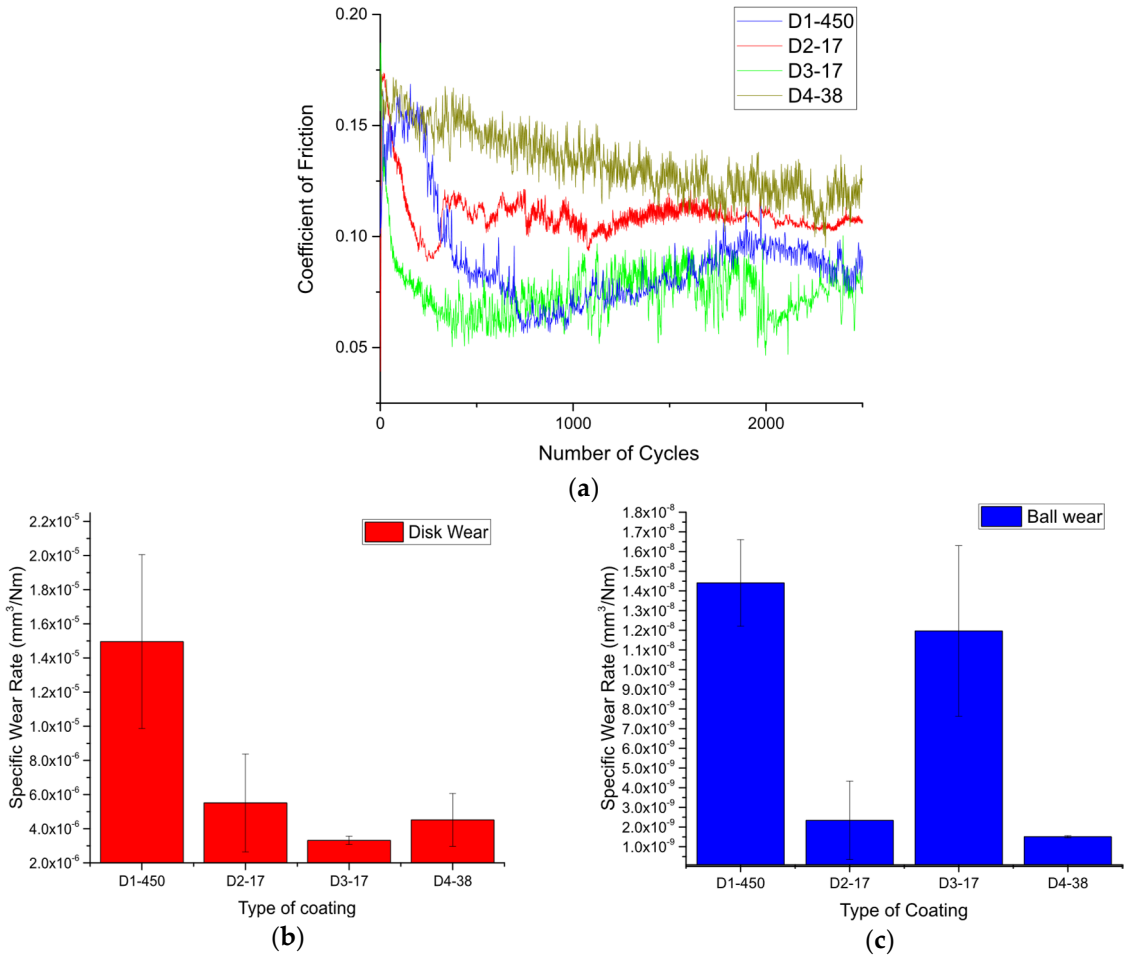

Figure 4-8 Tribological properties of selected coatings: (a) friction coefficient; (b) specific wear rate of the coated disks; (c) specific wear rate of the balls.

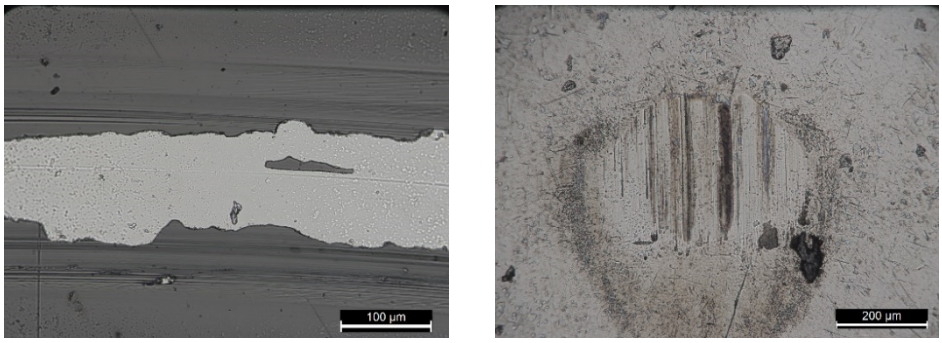

(**a**) (**b**)

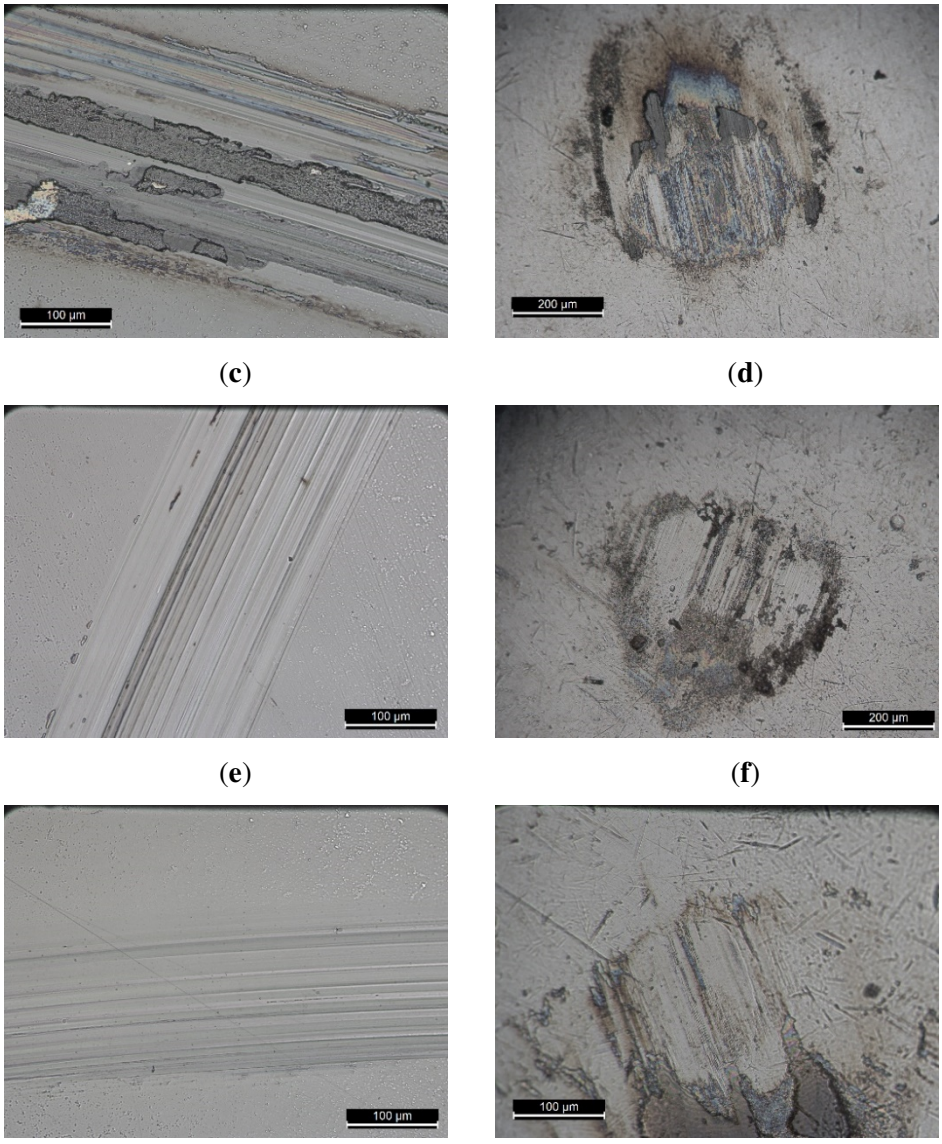

(**c**) (**d**)

(**e**) (**f**)

(**g**) (**h**)

Figure 4-9 Optical micrographs of the wear tracks on the disk and the wear scars on counterbodies: (a) D1-450 disk; (b) D1-450 ball; (c) D2-17 disk; (d) D2-17 ball; (e) D3-17-disk; (f) D3-17-ball; (g) D4-38 disk; (h) D4-38 ball

4.5 Conclusions

W-S-C(H) coatings were deposited by RF magnetron sputtering using four different procedures. The chemical composition of the coatings varied depending on the power at the targets, the number of pellets, and the partial pressure of the CH_4 gas. The S/W ratio was the lowest for the reactively sputtered coatings and those deposited from a composite target with the substrate being stationary. The difference in the S/W ratio was attributed to the different levels of bombardment with backscattered Ar neutrals. Cross-sectional micrographs showed dense and featureless morphologies, except for the films with the lowest C contents, where columnar growth was observed. In terms of crystallinity, only the coatings with low C contents (<30

at. %) and high overall amounts of S (>35 at.%) showed well-defined peaks related to planes of WS_2. The coatings with higher C contents (>30%) or low amounts of S (<30 at.%) had an X-ray diffraction amorphous structure, with the diffractograms showing a broad peak at $2\theta = 33–50°$. The XPS study revealed the presence of W-S and W-C bonds, in addition to C-C bonding. Raman spectroscopy revealed the presence of WS_2 crystals for the coatings with the highest amounts of S. The presence of a-C was also confirmed since the location and intensity of the D and G peaks were in the typical range for a-C. The hardness of the coatings increased for higher C contents and the lower S/W ratios. The hardness increase was attributed to the higher content of the harder a-C and W-C phases, as well as the overall densification of the coatings. Reactive-sputtered coatings showed the lowest hardness. The introduction of a Cr interlayer proved to be crucial for the adhesion since the coatings with the best adhesion were those where Cr interlayer was deposited. The tribological properties were related to the composition of the coatings as well as the overall mechanical properties. A coefficient of friction as low as ~0.06 could be achieved during dry sliding in ambient air for the hydrogen-free coatings with compact morphology and a C content of ~40 at.%.

For the upscaling of the W-S-C coatings, magnetron sputtering in non-reactive mode should be considered. Sputtering of a composite target (C with WS_2 pellets) and co-sputtering of individual WS_2 and C targets have the potential for providing tribologically viable coatings. To achieve compact morphologies with good mechanical properties, C contents should be higher than 30 at.%. The S/W ratio should be assessed carefully, as it can provide valuable information regarding the tribological properties of the coatings. The deposition of a metallic interlayer should be performed to improve the adhesion of the coatings on metallic substrates.

Chapter 5 Synthesis, microstructure and mechanical properties of W-S-C self-lubricant thin films deposited by closed-field unbalanced magnetron sputtering

Considering the results from the lab-scale study presented in Chapter 4, it was decided to proceed with the synthesis of W-S-C in the semi-industrial unit using a non-reactive process. Although the use of a composite target showed the best result, the use of separate TMD and graphite targets has some advantages. The decision for this approach was taken since the coatings deposited with separate TMD and graphite targets also showed promising results, if adhesion issues are neglected, a problem easily solved in the multi-cathode semi-industrial unit, allowing the extra deposition of adhesion interlayers. Moreover, the usage of separate targets allows the flexible control of the currents and voltages applied to the targets and, therefore, the control of the composition of the coatings. This chapter aims to provide the relationship between the process parameters and the composition, morphology, microstructure, and selected mechanical properties of the coatings deposited in a semi-industrial machine. A single coating was selected for tribological studies in various operating environments. The work was performed at CEMMPRE (University of Coimbra), the laboratory Led&Mat at Instituto Pedro Nunes in Coimbra, Portugal, as well as the Czech Technical University in Prague, Czech Republic.

This work resulted in the following publication:

T. Vuchkov, M. Evaristo, T. Bin Yaqub, T. Polcar, A. Cavaleiro, Synthesis, microstructure and mechanical properties of W–S–C self-lubricant thin films deposited by magnetron sputtering, Tribol. Int. 150 (2020) 106363. doi:10.1016/j.triboint.2020.106363.

5.1 Elemental chemical composition

The list of coatings, as well as their elemental composition, thickness, and deposition rate, are summarized in Table 5.1. The carbon contents were in the range of 38-55 at. % and compositional variations were observed depending on the target-to-substrate distance (TSD), bias voltage and power applied to the graphite targets. The thickness of the coatings deposited without substrate bias was ~2 µm for deposition distances up to 15 cm, with a reduction to ~1.6 µm for the coatings deposited at a distance of 25 cm. The application of substrate bias resulted in lower thicknesses, at constant TSD, which can be a result of the material removal caused by the continuous Ar^+ ion bombardment of the substrates during deposition and overall densification of the coatings [112].

Table 5.1 List of coatings deposited, deposition parameters and elemental composition

Coating	Target to substrate distance (cm)	Substrate bias (V)	Power applied to targets (W/cm^2)		Elemental composition (at. %)				S/W ratio	Thickness (µm)/Deposition Rate (nm/min)
			WS_2	C (x2)	C	S	O	W		
WSC1-10	10	0	2.1	2.6	44.0	28.5	4.9	22.6	1.26	2 / 16.7
WSC1-15	15	0	2.1	2.6	40.2	32.5	5.2	22.1	1.47	2.3 / 19.2
WSC1-25	25	0	2.1	2.6	38.1	35.1	5.8	21.1	1.66	1.6 / 13.3
WSC2-10	10	50	2.1	2.6	45.8	25.1	3.1	26.0	0.96	1.8 / 15
WSC2-15	15	50	2.1	2.6	48.2	24.0	2.8	25.0	0.96	1.7 / 14.2
WSC2-25	25	50	2.1	2.6	40.8	32.7	2.8	23.7	1.38	1 / 8.3
WSC3-10	10	0	2.1	3.2	57.6	20.1	2.4	20.0	1.01	2 / 16.4
WSC3-15	15	0	2.1	3.2	52.2	26.1	1.5	20.2	1.29	2 / 16.3
WSC3-25	25	0	2.1	3.2	53.0	27.5	2.4	17.1	1.61	1.6 / 13.1

The S/W ratio shows an increasing trend as the TSD is increased (see Figure 5-1). Similar trends were also observed by Cao et al. [99], where a similar deposition unit was used. However, they reported lower values of S/W ratio (below 1) for distances up to 15 cm. During the synthesis of TMD containing coatings by sputtering techniques, the sub-stoichiometry concerning sulfur (S/W < 2) is generally a result of 2 processes: (i) gas-phase scattering of the sputtered atoms, during their travel towards the substrate and, (ii) preferential sputtering of the chalcogen atom from the growing film [110]. At small TSD distances, the preferential resputtering of the chalcogen atoms from the growing film seems to have a major effect on the composition. In fact, for the discharge pressure used in the deposition (0.6 Pa), the mean free path of the particles is still very high, only being expected a few collisions during the interelectrode sputtered atoms trajectories; preferential re-sputtering should be, then, responsible for the lower S/W ratios.

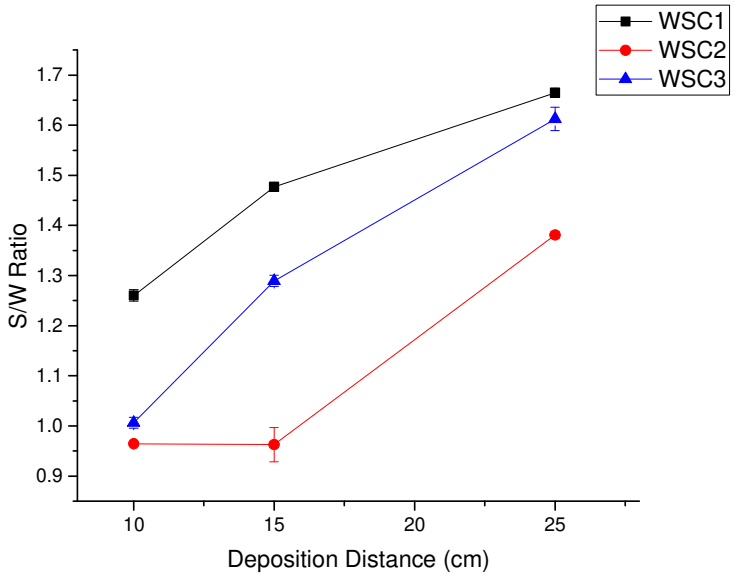

Figure 5-1 S/W ratio as a function of the deposition distance

The reduction of the S/W ratio as a result of negative substrate bias is a well-known phenomenon; by using p-DC bias on the substrates, the substrates are continuously bombarded by Ar^+ ions. Therefore, preferential resputtering of the lighter element, S, in relation to W occurs, which is often reported in the literature [131], resulting in a reduction of the S content in relation to the W content. A similar trend is observed with the increase of the power to the graphite targets, which resulted in increased target voltage and current. Such effects will contribute to the increase of the energy and number of neutral Ar atoms reflected on the target, produced by charge exchange collisions in the discharge cathode sheath. Reflected neutrals will bombard the growing film promoting the preferential resputtering of S in relation to W, which explains either the lower S/W ratios (S/W < 2) of all the deposited films or the lower S/W ratio when the C target power was increased.

The increase of the TSD has a marked influence on the S/W ratio due to the increasing importance of the particle collisions in the interelectrode space. On the one hand, reflected neutrals will be progressively thermalized having less and less influence on the re-sputtering effect of the growing film. Consequently, S will be preferentially sputtered from the growing film in a lesser amount, leading to a higher S/W ratio. On the other hand, the increasing number of collisions will make the deflection in the trajectories of both W and S sputtered atoms less different. For the low TSD, as the number of collisions is low, W atoms being much heavier will not be scattered as a result of collisions with the Ar atoms present in the chamber, resulting in more straight traversing paths and subsequent W enrichment. S atoms are much lighter and will scatter more during their travel resulting in S depletion. However, when that distance increases, a higher

number of collisions occur, with a consequent loss of energy of the sputtered atoms, being the diffusion mechanism in the transportation process more and more important. Therefore, the transport of sputtered species becomes similar, independently of their mass. As a consequence, the arrival rate of both W and S atoms to the growing film does not differ so much in relation to the sputtering rates in the target, giving rise to higher S/W ratios as the substrate to the target distance increases.

The effect of the increase of the target-to-substrate distance on the S/W ratio for coatings deposited using substrate bias was not so strong as in unbiased coatings (see Figure 5-1). From the two effects above described for unbiased coatings, the attenuation of the re-sputtering effect should not be considered in the analysis since, in this case, bombarding species are the Ar ions extracted from the discharge and accelerated by the negative bias potential applied to the substrate. Although challenging to analyze, small variations can be expected since the number of bombarding ions can vary with the position of substrates inside the deposition chamber. As the system works in unbalanced mode, magnetic field lines between cathodes can originate zones of higher density plasma in the discharge, affecting the ion current to the substrate. This is a possible explanation for the same values found for S/W ratio for positions at a substrate to target distances of 10 and 15 cm. As for the other coatings, a small increase in the S/W ratio would be expected for the 15 cm of TSD. This can only be understood if a slightly higher bombardment occurs at that substrate position, which is possible if a higher plasma density exists nearby.

Considering the elemental composition achieved for the deposited films, several factors were found to affect the composition of the films, with the TSD playing a major role. The total amount of power applied to the targets also resulted in compositional variation. The usage of substrate bias for the deposition of thin films is an excellent alternative to improve the overall tribo-mechanical properties, but, for this particular type of coatings, it will significantly hinder the lubrication properties as the coating will be depleted of sulfur.

5.2 Morphology and crystallinity

Carbon addition to TMD based coatings results in the densification of the morphology compared to the typical porous one of pure sputtered TMD based coatings [132]. All cross-sections presented in Figure 5-2 show dense morphologies, although a slight decrease in the compactness can be perceived when TSD increases, particularly for the 25 cm value, the coating having the lowest amount of C (38 % at.) and the highest S/W ratio (~1.6) for which some porosity and signs of columnar growth can be observed (Figure 5-2 c)). As explained above, these coatings deposited with increasing TSD are submitted to lower bombardment with its consequent detrimental effect on their density.

The top surface morphology of the coatings showed a cauliflower structure, which is typical of magnetron sputtered TMD thin films containing carbon.

The GIXRD patterns shown in Figure 5-3 indicate X-ray amorphous structures with a broad peak at 2θ ~ 30-40° with a tail towards higher angles. This broad peak is often related to a (100) reflection of WS_2 at 33° with the tail representing the turbostratic stacking of (10L) planes [132]. However, the peaks related to tungsten carbide are positioned in this region, too (see ref. [114,115]), making the interpretation of the pattern difficult. Although we cannot exclude the presence of WS_2 or WC crystals, their grain size would be below the detection limit of XRD (i.e., lower than 3-4 nm).

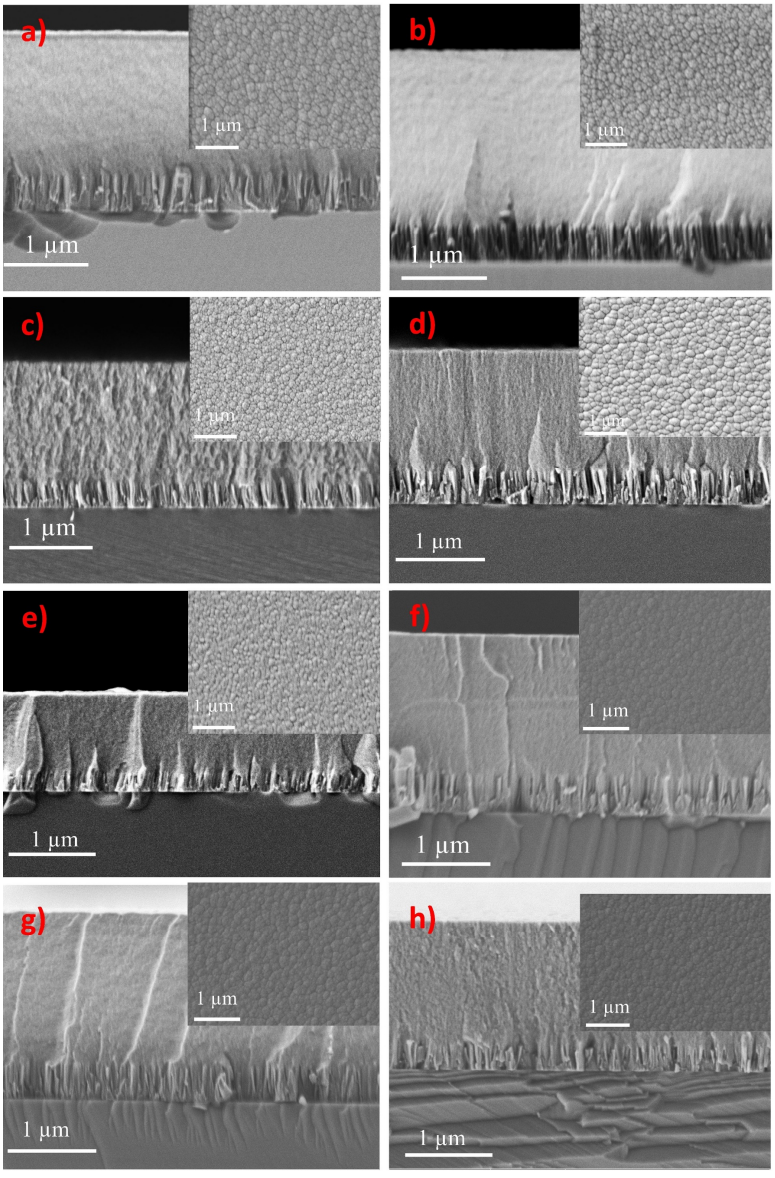

Figure 5-2 SEM micrographs of the cross-sections of as deposited coatings with the insets showing the top surface morphologies a) WSC1-10, b) WSC1-15, c)WSC1-25, d)WSC2-15, e)WSC2-25, f) WSC3-10, g) WSC3-15, h) WSC3-25

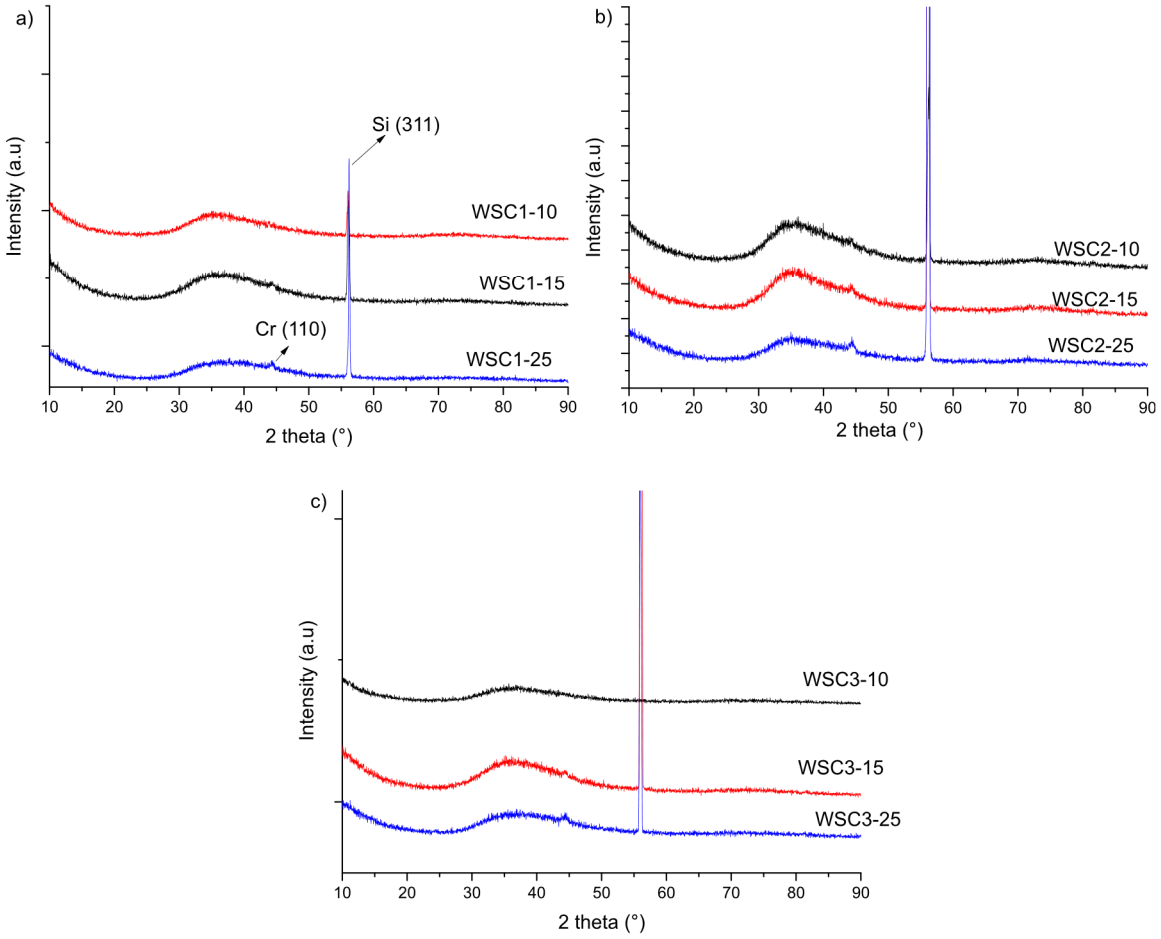

Figure 5-3 GIXRD patterns for: a) WSC1, b) WSC2, c) WSC3

5.3 Mechanical properties

Hardness (H) and reduced modulus of elasticity (E*) values from nanoindentation experiments are shown in Figure 5-4 a) and b), respectively. The hardness is reduced when the target to substrate distance is higher. It is worth mention that non-hydrogenated DLC coating deposited in this equipment at the target to substrate distance of 15 cm, with similar power applied to the graphite targets and substrate bias of 50 V, yielded a hardness of ~13-15 GPa [133]. Therefore, an increase in hardness with higher carbon content is expected. The presence of tungsten carbides could further enhance the hardness [134] and, for the films with a lower S/W ratio, there is more W available for the formation of W-C phases. On the other hand, the high content of sulfur in amorphous films or nanocrystalline WS_2 phases leads to hardness reduction. Finally, more compact films achieved at the lower substrate to target distances are expected to be more resistant to the indenter penetration, which would increase the hardness.

As expected, the softer coating is the one deposited without substrate bias and lower carbon content for the same substrate to target distance. The factors influencing the hardness have already been discussed; the films deposited with substrate bias are more compact and have lower S/W ratios resulting in hardness increase. Similarly, the films deposited with a higher power in the C targets have a higher content of the harder a:C phase. Thus, their hardness exceeds the ones prepared with substrate bias and lower C content.

Reduced elastic modulus values follow the trends observed for hardness values. The values of H/E*, representative of elastic strain to failure [135], and H^3/E^{*2}, which is proportional to the resistance to plastic deformation, are often related to the wear behavior of the coatings with lower values for reduced modulus of elasticity desirable [136]. H/E* ratios are in the range of 0.054-0.081 with lower values for a longer target to distance; as an example, WSC1 coating deposited at 10, 15, and 25 cm has values of 0.08, 0.081 and 0.069 respectively. The values of H^3/E^{*2} are in the range of 0.018-0.057 and similar trends are observed as for the H/E* ratio.

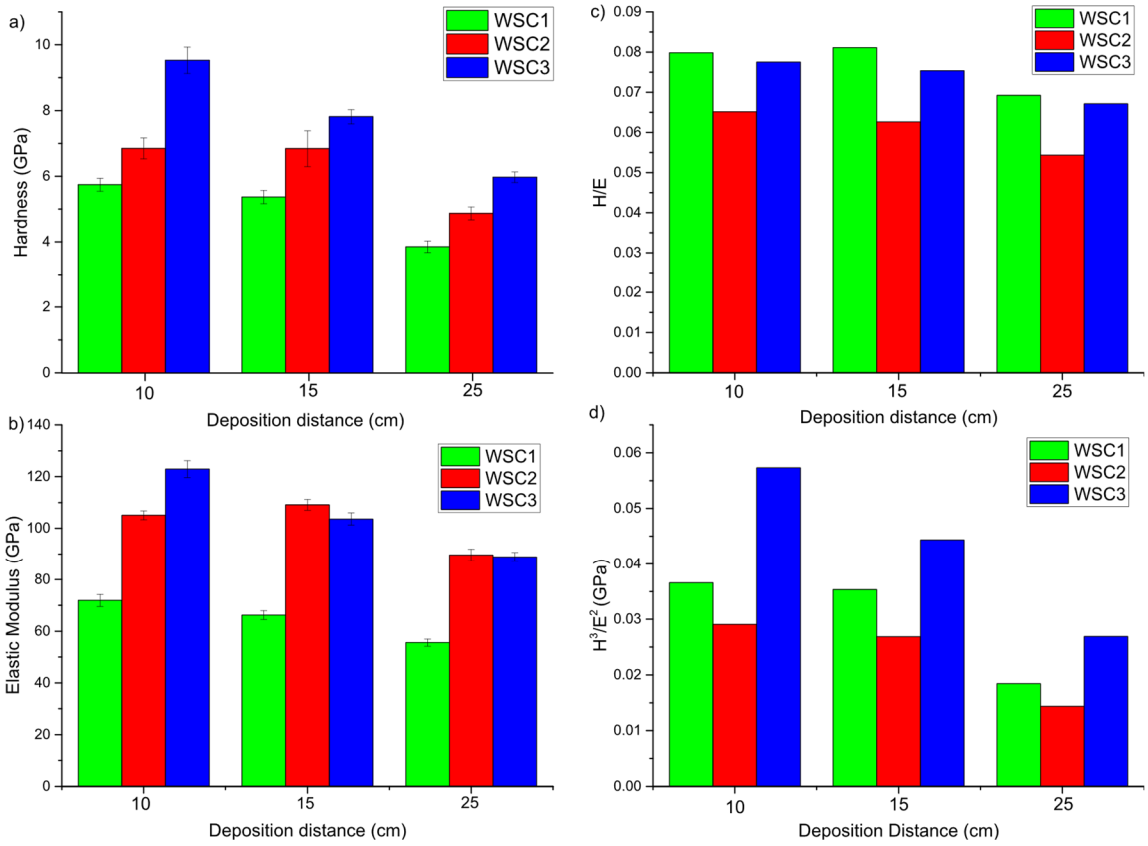

Figure 5-4 a) Hardness, b) Elastic Modulus, c) H/E and d) H^3/E^{*2} of the coatings*

5.4 Tribological properties

The selection of the coating for the tribological testing was based on the best compromise among various relevant parameters, such as overall S content, S/W ratio, hardness, cross-sectional morphology, H/E* and target-to-substrate distance. For tribological testing, the WSC1-15 was selected due to moderate hardness (~5.7 GPa), a moderate S/W ratio (1.47), a high amount of the lubricious WS_2 phase (only 40 at. % of C and a total of ~32 % of S) and among the highest value for H/E* parameter, which is known to be related with the tribological performance. Moreover, this TSD is generally used for the deposition of coatings in this deposition equipment.

5.4.1 Influence of the normal load

The evolution of the friction coefficient can be seen in Figure 5-5 a). The test performed under a 5 N load showed a friction coefficient of ~0.15 at the start of the test, followed by a decrease to ~0.1 in the initial 2500 cycles. After an initial testing phase, an increase of friction is observed with value as high as 0.25 after 40000 cycles, followed by a drop to a value of ~0.17. Testing under higher load (35N) resulted in a much lower coefficient of friction, starting at 0.05 with a steady increase towards a final value of ~0.07, with an average value of 0.06. Similar trends (non-Amonton behavior) were also observed in previous studies [132]. Specific wear rates calculated after the tribological tests can be seen in Figure 5-5 b). The coating tested with 5 N of load (5 x 10^4 cycles) showed an average value of ~3 x 10^{-7} mm^3 N^{-1} m^{-1}. Testing with 35 N resulted in lower wear rates for the disk with a value of ~1.0 x 10^{-7} mm^3 N^{-1} m^{-1}. Higher counterbody wear was observed for the 100Cr6 balls from the tests under the load 35 N (~10^{-8} mm^3 N^{-1} m^{-1}) compared to the ones tested with 5 N load (~8 x 10^{-9} mm^3 N^{-1} m^{-1}).

Raman spectroscopy was performed on the wear scars of the disks as well as on the counterbodies. For the coating tested under 5 N load, the analysis was performed after the test with 5 x 10^4 cycles. The as-deposited coating does not show any peaks related to WS_2, with the most prominent peaks being D and G peaks with location and intensity typical for amorphous carbon. Raman spectra on the disk track after testing with 5 N of load does not show any significant changes, the main feature observed was the D and G peaks related to the a-C phase with very similar intensities compared to the as-deposited coating. The Raman spectroscopy performed on the tribolayers formed on the bearing steel ball show strong intensities related to graphitic carbon (see Figure 5-5 c)). The Raman spectroscopy performed on the wear debris revealed the presence of tungsten oxides (Raman shift values of ~800 and ~970 cm^{-1}) and graphitic carbon. On the other hand, the analysis performed on the tribolayers formed on the disk track, and the ball scar, after testing with 35 N load, shows intensities at Raman shift values of ~350 and ~417 cm^{-1}. Tungsten disulfide has two distinct Raman peaks in this region; the first one is at 350 cm^{-1} (representing the in-plane phonon mode $E^1_{2g}(\Gamma)$) while the second peak is located at 417 cm^{-1} (related to the out of plane phonon mode $A_{1g}(\Gamma)$) [127]. As a

reference, a Raman spectrum from pure sputtered WS_2 was also plotted. These changes in the Raman spectra can be attributed to the presence of crystalline WS_2 on both surfaces in the sliding contact. The presence of crystalline WS_2 on the sliding surfaces can be associated with the observed reduction in friction [137]. The drop in friction as the load is increased can be associated with the presence of a low shear strength tribolayer rich in WS_2; increasing loads facilitate the formation of this tribolayer. Furthermore, TMD containing coatings are known to provide a lower coefficient of friction with increased loads (see ref [138–140]). A drop in the coefficient of friction with increased loads was also observed in previous studies on lab-scale deposited W-S-C coatings [86]. A recent molecular dynamics (MD) study [141] has shown that there is an energy threshold that needs to be achieved to trigger amorphous to crystalline transition in MoS_2. In our case, the usage of increased load can significantly raise the energy input at the sliding interface, providing enough energy to induce increased crystallization of the WS_2 phase, resulting in the formation of a low friction tribofilm. Based on these results, the tribological behavior (under standard laboratory air) of this coating is mainly governed by graphitic tribofilms during testing with low normal loads (e.g. 5 N). Increasing the normal load (35 N in our case) causes the formation of a WS_2 (very likely due to higher energy input in the contact) with higher crystallinity. The presence of WS_2 in the sliding interface further facilitates the lubricity, which is evident by the drop in the coefficient of friction.

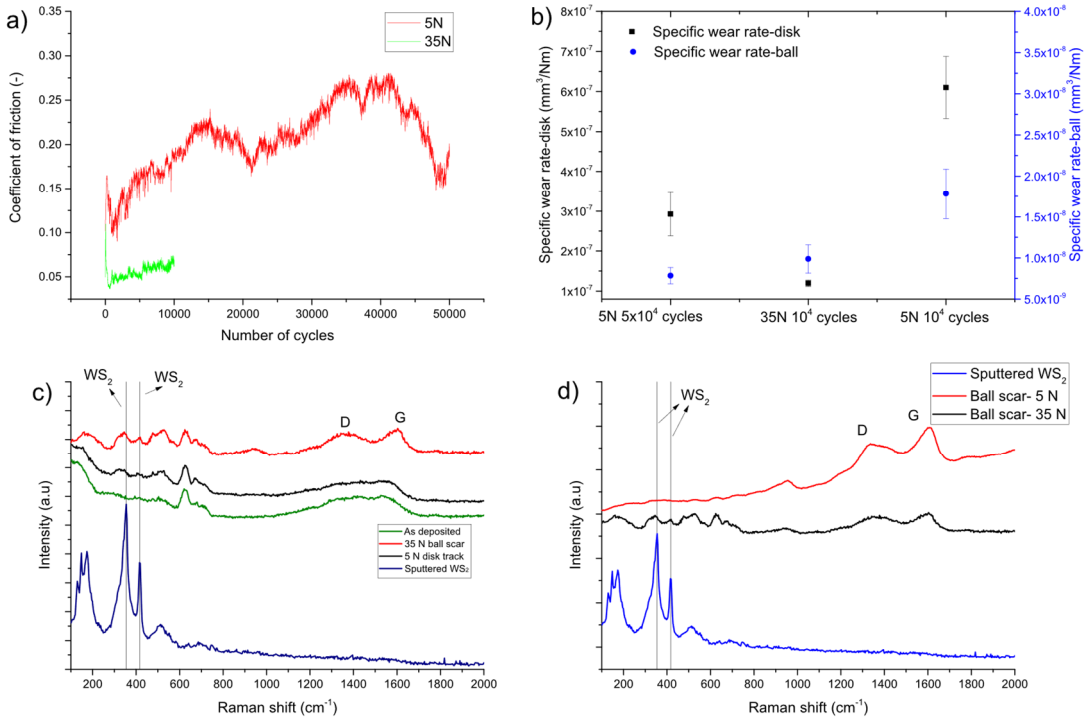

Figure 5-5 Result from the tribological testing in normal laboratory air: a) evolution of friction coefficient, b) specific wear c) Raman analysis of the wear tracks d) Raman analysis of the ball scars

5.4.2 Influence of the testing temperature

The tribological behavior of the coatings was tested at different temperatures from 100 to 400 °C. Figure 5-6 a) shows the evolution of the friction coefficient as a function of the number of sliding cycles. Running-in phase with steadily decreasing coefficient of friction from an initial value of 0.05 was observed at 100 °C; at about 1500 cycles, the coefficient of friction stabilized at a value as low as 0.01. The running-in period was much shorter for the tests performed at 200-400 °C and the steady-state regime is observed after 500 cycles. Average friction coefficient values calculated from the last 2500 cycles are shown in Figure 5-6 b).

In terms of wear, the coating shows increasing wear with testing temperature (Figure 5-6 c)). The wear in the counterbody follows similar trends as the disk wear for testing at temperatures up to 200 °C. Surprisingly, at the highest testing temperatures, no wear was detected on the counterbodies, due to material transfer from the coating. Similar tribological behavior of W-S-C coatings deposited in lab-scale equipment by RF magnetron sputtering with similar C content, and slightly lower S/W ratio, was also observed by Polcar et al. [142].

Again, Raman spectroscopy was used to investigate the worn surfaces; an example is shown in Figure 5-6 d) (testing temperature of 100 °C). Raman spectroscopy performed on the tribofilms, at locations similar to the patches of material shown at the location 1 in Figure 5-7 b), formed after sliding at elevated temperatures show clear contributions of the WS_2 phase responsible for a very low value of the coefficient of friction. It should be noted that Raman performed in the areas showing only shallow abrasive marks revealed a spectrum quite similar to the as-deposited one. The wear track after testing at 400 °C was also analyzed by SEM. An overview of the scar is shown in Figure 5-7 a). No signs of delamination indicate excellent adhesion of the coating to the substrate. The wear track is mostly smooth with shallow abrasive marks and areas with patches of adhered material. Higher magnification imaging and energy-dispersive spectroscopy (EDS) was performed on these patches, see Figure 5-7 b). EDS performed on the adhered material (area 1) showed a significant amount of oxygen and a small but measurable amount of iron, the latter originates from the counterbody. EDS performed in area 2 showed a higher amount of C (71 at. %) and lower S/W ratio (1.2, compared to 1.47 from the as deposited state); however, there were no vestiges of iron and a meager amount of oxygen.

Two main effects should be considered to understand the effect of temperature on the friction behavior. Firstly, heating to temperatures higher than 100 °C allows drying of the atmosphere around the testing rig, avoiding the detrimental effect of humidity in increasing the friction. Secondly, the increased temperatures

facilitate the formation of the crystalline WS_2 phase [141], and decrease its shear strength, which further contributes to the friction reduction. Raman spectroscopy performed on the tribofilms also shows the presence of graphitic carbon as a consequence of the structural transformation of the a-C phase. The presence of graphitic carbon, a very soft phase, in the tribofilms is likely the cause of the increased wear of the coating. Although carbon-based material was detected in the tribofilms, its role towards the frictional response is mainly related to the load-bearing capacity. It should be noted that hydrogen-free graphitic carbon is unable to provide friction reduction at elevated temperatures due to the lack of water vapour needed as an intercalating agent [9]. Increased coefficients of friction were often observed for hydrogen-free a-C coatings during elevated temperature testing (see, for example, Ref. [143,144]). Furthermore, the Raman signal can also originate from volumes below the lubricious tribofilms. Considering a very low coefficient of friction, the tribological response is mainly governed by the crystalline WS_2 formed during the testing, while the carbon phase provides the load-bearing capacity. The Raman spectroscopy performed on the wear debris (not shown) indicated D and G peaks typical of graphitic nature with very high intensity, together with a small WO_3 contribution at Raman shift value of ~800 cm^{-1}.

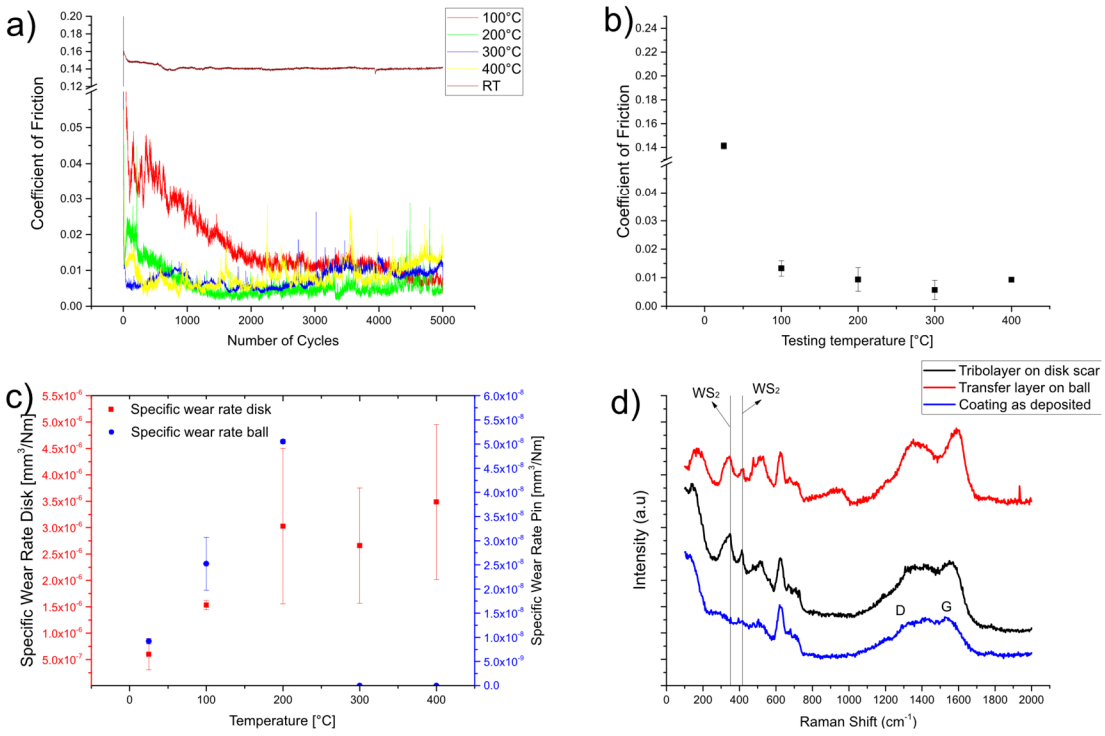

Figure 5-6 Results from the tribological tests at elevated temperatures: a) Evolution of friction coefficient as a function of the number of cycles, b) average friction coefficient as a function of testing temperature for the last 2500 cycles, c) specific wear rate of the pin and the coated disk as a function of testing temp d) Raman spectra obtained from the disk and ball after testing at 100°C.

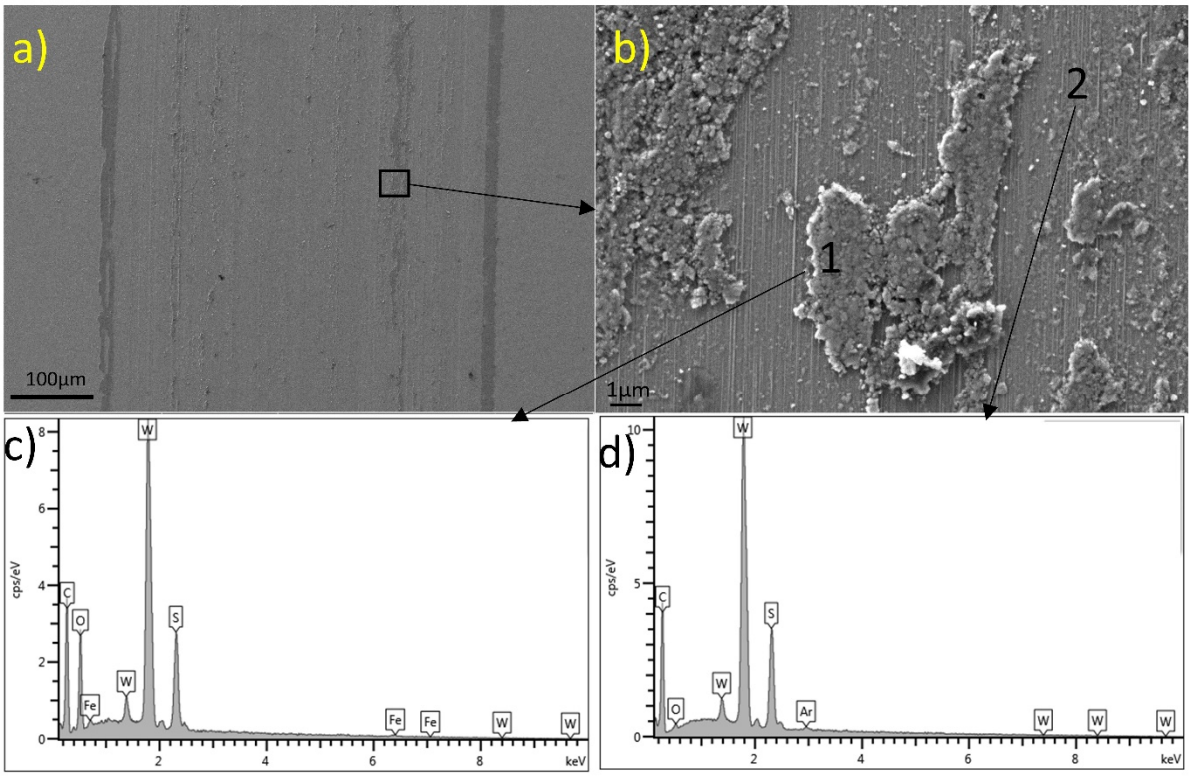

Figure 5-7 SEM imaging performed on the coating tested at 400°C: a) overview, b) higher magnification detail c-d) EDS spectra

5.4.3 Tests performed in vacuum and dry nitrogen

Initial testing in vacuum was performed against a 100Cr6 bearing steel counterbody under a load of 2 N (see Figure 5-8). The very low friction coefficient of ~0.01-0.02 was measured for the first 100 cycles after which a significant increase in the friction coefficient occurred with a final value of 0.4-0.5 at 800 cycles when the test was stopped. 3D profilometry performed on the ball counterbody revealed significant wear with a wear scar diameter of ~0.8 mm. On the other hand, 3D profilometry on the wear track of the disk did not show any wear with a significant presence of transferred material.

Considering the significant amount of wear of the bearing steel counterbody, with an indication of material transfer to the coated disk, it is clear that 100Cr6 bearing steel is not an appropriate sliding partner to achieve low friction. Therefore, the balls were also coated with the same coating as the disks, and the sliding tests were performed with a load of 2 N in a vacuum and a dry nitrogen environment. For the vacuum tests, the coefficient of friction was very low in the initial 1000 cycles with values below 0.01. Then, a spike in the friction appeared. Periodic spikes in friction to values up to 0.4 were followed by drops to low values in the range of 0.01-0.02 until the end of the test. These spikes are a clear indication of coating failure and optical

micrography showed zones where the coating flaked off at the counterbody revealing the steel surface. The delamination was limited only to the coated ball; the integrity of the coating deposited on the disc was preserved with maximum wear depth lower than the thickness of the coating. Specific wear rates for both triboelements were quite high, 2.5 x 10^{-5} and 1.3 x 10^{-6} mm^3 N^{-1} m^{-1} for the disk and the pin, respectively.

Tests performed in dry nitrogen showed a much more stable friction coefficient. Starting at rather low values of ~0.01, the coefficient of friction continuously increased up to values of 0.03-0.04 after around 1000 cycles. For the remaining time of the test, the friction coefficient fluctuated within values between 0.02-0.04, values slightly higher than those found in tests performed in a vacuum (not considering the spikes). Only sporadically, friction spikes occurred. The coatings showed lower wear compared to the tests performed in a vacuum with values of 2.4 x 10^{-7} and 3.7 x 10^{-8} mm^3 N^{-1} m^{-1} for the disk and the pin, respectively. Raman spectroscopy was performed on the triboelements after testing under dry N_2 and vacuum environment (see Figure 5-9). The tribolayers analyzed after testing presented intensities in the regions related to WS_2 (~350 and 417 cm^{-1}) as well as those related to carbon-based phases (1200-1700 cm^{-1}). Based on these results, the tribolayers are composed of C-based and TMD-based materials.

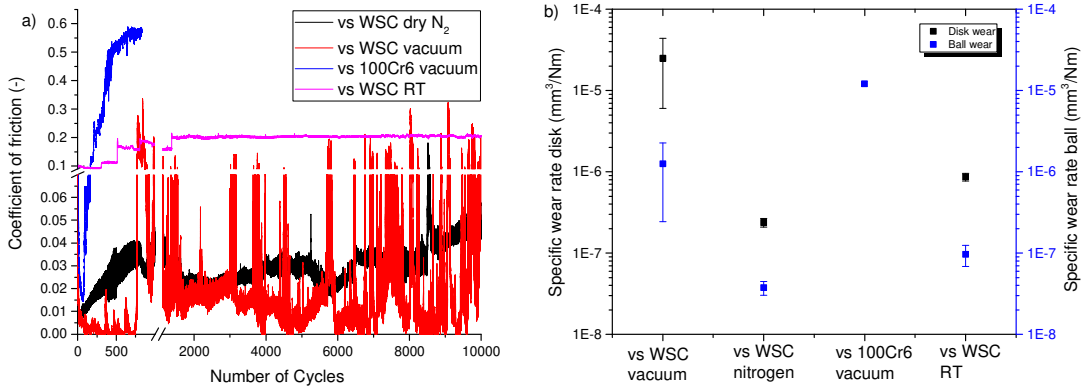

Figure 5-8 Results from the testing in vacuum and dry N_2 environments a) coefficient of friction b) specific wear rate

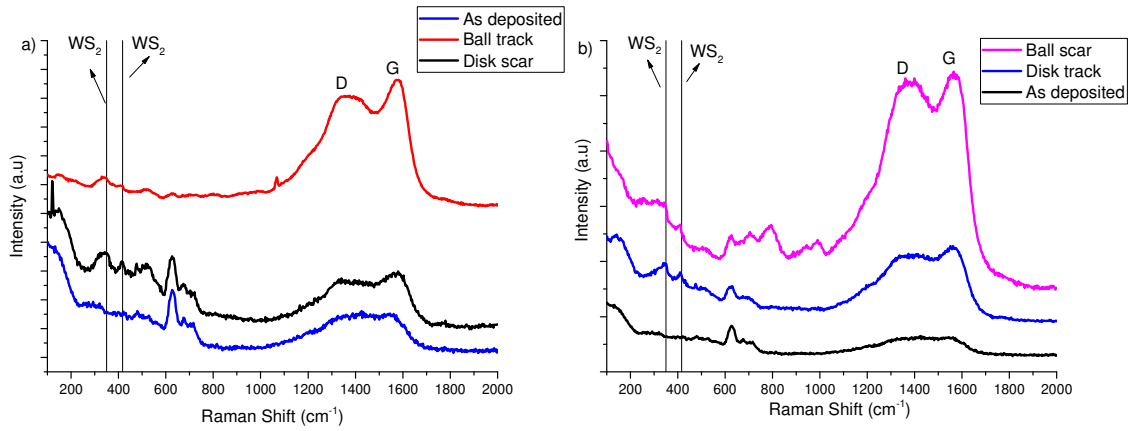

Figure 5-9 Raman spectroscopy performed after testing against W-S-C coated balls a) Dry N_2 environment b) vacuum environment

SEM was also performed on selected wear tracks (see Figure 5-10) from the testing performed in dry N_2 and vacuum. The disc track after testing with 2 N load against 100Cr6 counterbody in a vacuum can be observed in Figure 5-10 a,b). Lower magnification overview of the scar shows the presence of material transfer (darker regions in Figure 5-10 a)). Two regions were selected for EDS analysis (spots 3 and 4 in Figure 11 b)). The EDS analysis performed in the darker region (spot 3) resulted in 15 at. % of O, 5 at. % of Fe, 2 at. % of Cr, with the rest being a mixture of W, C and S, indicating transfer of ferrous material from the steel counterbody. Compared to the composition obtained from the analysis done on the brighter areas of the scar (spot 4), darker patches, also contain more C and O. Considering the high coefficient of friction and the preferential wear of the steel counterbody, it is very likely that the friction is governed by the hydrogen-free carbon phase, which is known to be unable to provide friction reduction unless species that can passivate the carbon atoms (e.g. water vapour, hydrogen) are available [145]. The presence of a hydrogen-free carbon phase on the sliding interface, unlike during sliding in air, is disadvantageous during sliding in a vacuum. Furthermore, as iron-based material is transferred on the disk, the interface between both counterbodies will be of a metal-to-metal type, which can have strong adhesion in vacuum resulting in a high coefficient of friction and wear of the counterbody [146]. Comparing the tests at high temperature and in a vacuum, it is very likely that crystallization of the WS_2 at elevated temperatures is occurring quite fast and the friction is governed by WS_2 rich tribofilm, while the effect of the carbon phase is not as negative during elevated temperatures testing compared to the vacuum testing. For example, Krumpiegl et al. [143] observed considerably worsened performance of hydrogen-free a-C coatings during testing under vacuum compared to elevated temperature.

SEM was also performed on the wear track after testing with 2 N of load against W-S-C coated ball in a vacuum environment (Figure 5-10 c)). Only a minimal amount of material transfer is visible compared to the test performed against 100Cr6 ball. EDS performed on one of these areas (spot 5, Figure 5-10 d)), also showed the presence of Fe (5 at. %) in addition to an increased amount of oxygen, again indicating material transfer from the ball. Cr was also detected (up to 1% at.), and, in this case, it can originate from the interlayer of the film deposited on the counterbody, as the coating of the ball was worn through during the test. Finally, SEM was also performed on the scars after testing in a nitrogen environment. The main difference that was observed was the presence of a much narrower wear scar (compare Figure 5-10 a,c) and Figure 5-10 e)). Smooth darker patches were also seen, aligned in the direction of sliding. EDS was performed on the brighter and darker areas of the scar, but no significant difference was observed.

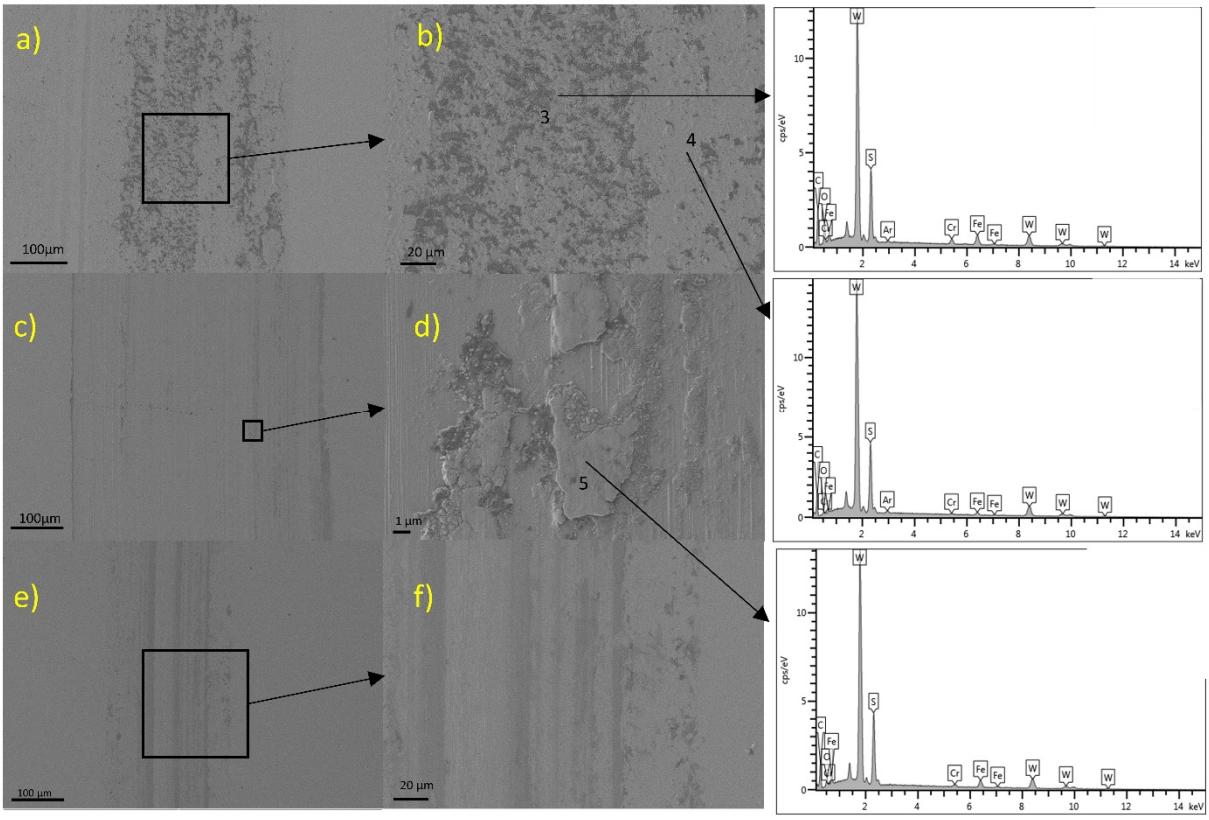

Figure 5-10 SEM micrographs of the disk wear scars after testing: a-b) 2N vs 100Cr6 in a vacuum, c-d) 2N vs WSC coated ball in a vacuum, e-f) 2N vs WSC coated ball in nitrogen

A significant difference can be observed for the tribological response of the WSC-WSC tribopair tested in a vacuum and dry nitrogen environments. Coatings with similar composition were also tested in a vacuum and dry N_2 against steel counterbodies in the work of Voevodin et al. [79]. Contrary to this study, for

coatings with at least 22. % at. of sulfur they observed very low friction in both dry N_2 and vacuum. In that work, the coatings that provided lubrication in dry N_2 had similar performance in a vacuum. The most probable reason for this behavior should be the different S/W ratio, although other parameters, such as the level of crystallinity of the films should not be disregarded [147]. Unfortunately, neither the crystallinity nor the S/W ratio can be indexed to the particular film, which was tested by Voevodin et al., in the conditions herein used. The worsened tribological response in a vacuum, for the coatings having low sulfur content, was attributed to the inability of the hydrogen-free amorphous carbon to provide lubrication in a vacuum and dry N_2 environments.

Extensive testing of TMD coatings alloyed with carbon was also performed in dry environments (N_2, dry air, Ar), against steel counterbodies [148–150]. The coatings having a similar chemical composition to the one presented in this study, have shown very good tribological performance. The reduction of friction and wear in these cases was attributed to a TMD tribolayer, protected from environmental attack with its basal planes oriented in the direction of sliding. The influence of the carbon phase was mostly related to the hardness improvement; during sliding, it was preferentially removed from the sliding interface. Comparing those results with the ones presented here, the coefficient of friction values (between 0.02-0.04) and specific wear rates for the disk (10^{-7}-10^{-6} mm^3/Nm) are quite similar, indicating that the friction reduction mechanism is similar. Indeed, Raman spectroscopy performed on the triboelements showed the presence of crystalline WS_2 on the sliding surfaces, while the debris was rich in graphitic carbon indicating that the C-phase is removed from the contact.

Considering the results from the testing performed in a vacuum, the mechanism proposed for friction and wear reduction in dry atmospheres (e.g. dry N_2) might not be valid. The coefficient of friction values when 100Cr6 bearing steel balls slide against the W-S-C coating were very similar to the values for hydrogen-free carbon coatings sliding against steel counterbodies in vacuum (see Ref. [145,151]). Considering the similarities of the tribological response of the tribopair in vacuum with the behavior of hydrogen-free carbon coatings, it can be assumed that the carbon phase plays a role in the tribological response. In the case of the uncoated ball, the response appears to be governed by the carbon-based material. When both sliding partners are coated, the coefficient of friction in vacuum is initially quite low indicating that the response is mainly governed by the WS_2 phase. Friction spikes during the remaining time of the test can again be a result of the influence of the carbon phase. The Raman analysis performed on the disk track showed carbon peaks with similar intensity as the ones observed in the as-deposited state. Small vestiges related to WS_2 can also be observed. The optical micrograph of the coated ball showed the complete wear of the coating. The Raman spectra revealed a significant presence of carbon in combination with WS_2 and WO_3 phases. The compounds identified can be directly related to the tribological response during the test.

The periods of low friction can be attributed to the presence of WS_2 in the sliding interface, while the frictional spikes are due to periodic interaction between the carbon phases present on both surfaces in contact.

However, it is still not clear why there is a discrepancy in the tribological response in vacuum compared to a dry nitrogen environment. Colas et al. [152], also observed a discrepancy in the tribological response of a Ti-doped MoS_2 coating during testing in vacuum, and under dry N_2 environment; in the latter test, much better performance was achieved. The authors associated the good response in dry N_2 with the adsorption of N_2 and the subsequent occupation of all the oxidation sites, preventing the adsorption of H_2O on the coating. Anomalous wear behavior of MoS_2 coatings in vacuum was also observed by Micheal Gardos [153]. In that study, the author also associated the better tribological response in dry N_2, compared to vacuum, to the adsorption of N_2 on the oxidation sites of the MoS_2 and, thus, preventing the adsorption of other species (e.g. H_2O) in the MoS_2 films. Considering the vacuum pressures at which Gardos performed the tests, which were quite similar to the ones used in our study, it is likely that the mechanism proposed by Gardos is herein valid.

5.5 Conclusions and future work

W-S-C self-lubricating coatings were deposited by close field unbalanced magnetron sputtering in a semi-industrial unit with various powers to targets and three target-to-substrate (TSD) distances. The chemical composition, microstructure, and mechanical properties were studied as a function of the selected deposition parameters. Tribological studies were performed on a single coating in various testing environments. The main conclusions are:

- TSD has a significant effect on the composition of the coatings, with the longer distances resulting in a higher S/W ratio and a higher overall amount of sulfur. The effect was a result of different scattering behavior of the sputtered species and different level of the bombardment of the growing film with energetic particles.

- The composition of the coatings influenced the microstructure and mechanical properties. Lower S/W ratios and higher C contents resulted in denser microstructures and increased hardness. X-ray diffraction experiments showed X-ray amorphous structures

- The tribological testing of the selected coatings showed good tribological response while testing in normal air with different loads and at elevated temperatures up to 400 °C. The frictional response was governed by graphitic tribofilms during testing at RT, with low loads. Increasing the loads and/or the testing temperature resulted in the accelerated formation of WS_2 rich tribofilms with a subsequent reduction in friction.

- Testing in vacuum with steel counterbodies resulted in very high friction, which was due to severe adhesion that led to preferential wear and material transfer from the steel counterbody to the coated disk. Tribological testing in vacuum with both counterbodies being coated resulted in significant improvement of the tribological response, but instabilities were observed.

- Testing in dry N_2, with both triboelements being coated was optimal with low coefficient of friction and low wear.

The coating that was tribologically tested might not be an ideal solution for providing friction and wear reduction in diverse testing environments since the tribological response in the vacuum was unstable. To better understand the relationship between the chemical composition and the tribological response, further studies will be performed on a set of coatings with a higher S/W ratio.

Chapter 6 The effect of substrate location on the composition, microstructure and mechano-tribological properties of W-S-C coatings deposited by magnetron sputtering

Aiming towards the industrial implementation of TMD-based coatings, in this chapter, W-S-C coatings deposited on substrates, placed on various locations in the semi-industrial chamber, are studied. The location of the substrates was chosen to mimic the surfaces of bigger components with more complex shapes, like moulds or dies. The recipe used for deposition was the one yielding ~50 at. % of carbon, based on the studies performed in previous chapters. The composition, structure, crystallinity, morphology, mechanical and tribological properties of the coated samples were studied. The work undertaken resulted in the following publication:

T. Vuchkov, M. Evaristo, T. Bin Yaqub, A. Cavaleiro, The effect of substrate location on the composition, microstructure and mechano-tribological properties of W-S-C coatings deposited by magnetron sputtering, Surf. Coatings Technol. 386 (2020) 125481. doi:10.1016/j.surfcoat.2020.125481.

6.1 Chemical composition and (micro)structure

The list of coatings deposited (see Figure 3-2) with their respective chemical composition is shown in Table 6.1.

Table 6.1 Coatings deposited, chemical composition and deposition rate

Coating	Elemental composition (at. %)				S/W ratio	Thickness (µm) / Deposition Rate (nm/min)
	C	S	O	W		
WSC-1	51.7 ± 0.2	24.6 ± 0.1	3.4 ± 0.2	20.5 ± 0.1	1.2	1.4 / 14
WSC-2	49.8 ± 0.2	28.3 ± 0.3	3.9 ± 0.1	18.1 ± 0.1	1.56	1.0 / 10
WSC-3	49.2 ± 0.1	27.3 ± 0.1	3.8 ± 0.1	19.7 ± 0.2	1.4	1.2 / 12
WSC-4	47.6 ± 0.1	29.4 ± 0.1	5.4 ± 0.5	17.4 ± 0.1	1.69	1.0 / 10

The coating placed on position 1 showed the highest amount of carbon and the lowest S/W ratio. The coating placed at position 2 showed a higher sulfur content (28.3% at.) with a much higher S/W ratio of 1.56 compared to the one deposited at location 1. Besides the sample being at a target-to-substrate distance of 15 cm, its orientation with the coated surface, not facing the targets directly during its pass in front of them, caused a change in the chemical composition. The substrate placed at position 3 displayer a S/W ratio (1.4) which is between the ratios observed for the substrates facing the targets placed at 15 and 25 cm. Finally, the coating positioned at location 4 has the highest amount of S, and the highest S/W ratio of 1.69.

The variations in the chemical composition of TMD coatings deposited by magnetron sputtering techniques are generally a result of two processes: i) different scattering behavior of the sputtered species and ii) preferential re-sputtering of the chalcogen atom due to bombardment of the growing film with energetic particles during deposition [110]. The effect of both processes was simulated using the SIMTRA software package. The results from the simulations performed in the SIMTRA software are summarized in Table 6.2.

Table 6.2 Results from the simulations performed in the SIMTRA software: S/W ratio calculated from the flux of arriving S and W atoms, the fraction of the backscattered Ar neutrals arriving at the substrates, percentage of the Ar neutrals that arrive at the locations thermalized and average energy of the Ar neutrals

Location	S/W ratio	The fraction of arriving Ar neutrals (%)	Thermalized Ar atoms (%)	E_{av}Ar (eV)
WSC-1	1.77	0.27	7.5	78.4
WSC-2	2.44	0.17	14.2	67.91
WSC-3	1.76	0.25	10.8	72
WSC-4	1.88	0.16	19.4	60.8

The S/W ratio as depicted from the flux of S and W atoms arriving at the substrates was highest for the WSC-2 position with a value of 2.44. As for the other location the values ranged between 1.76-1.88. A significant difference can be observed for the flux and the average energy of the backscattered Ar atoms arriving at the substrate locations used for deposition. The trends observed can be related to the chemical compositions attained. Namely, the flux and the energy of reflected Ar neutrals arriving at the substrates decreased in the following order: 1>3>2>4. On the other hand, the S/W ratio increases in the same order (1<3<2<4), indicating that the bombardment with reflected Ar neutrals has a major effect on the compositional variations. Considering that the ratio of the fluxes of S and W atoms did not change significantly for the location 1,3 and 4, it can be assumed that the different scattering behavior of the S and W has a minor effect on the chemical composition. As for the substrate located at position 2, the simulations predicted a possible S enrichment due to the different scattering behavior. However, considering that this coating still had a lower S/W ratio, compared to the one deposited at location 4, the different level of bombardment with reflected Ar neutrals is the dominant process influencing the compositional variations.

In summary, both processes responsible for the compositional variations were simulated to separate their effects. Due to different scattering behavior of W and S atoms we expect S/W ratios in the range of 1.7-2.4. The lower measured ratios are due to the preferential re-sputtering of the S atoms from the growing films by the backscattered Ar neutrals, with lower ratios for the coatings subjected to more intense bombardment.

Cross-section and top-view micrographs of the coatings can be observed in Figure 6-1. The Cr interlayer has a thickness in the range of 200-400 nm; the lower thicknesses are for the coatings deposited at either longer target-to-substrate distances or not facing the target directly, very likely due to the increased scattering of the sputtered Cr species. The Cr interlayer has a columnar microstructure that changes to a more compact featureless morphology during the gradient layer deposition. The W-S-C coatings have featureless morphologies with no signs of columnar growth. The Cr interlayer is towards establishing a

strong metallic bond with the steel substrate and it is often the material of choice for depositing interlayers during the synthesis of carbon-based sputtered coatings [154,155]. The role of the gradient layer is to prevent abrupt changes in the bonding type and a smooth transition in the chemical composition, from Cr-rich to W-S-C rich. The top surface morphology was of a cauliflower-type, which is often observed in carbon-alloyed TMD coatings.

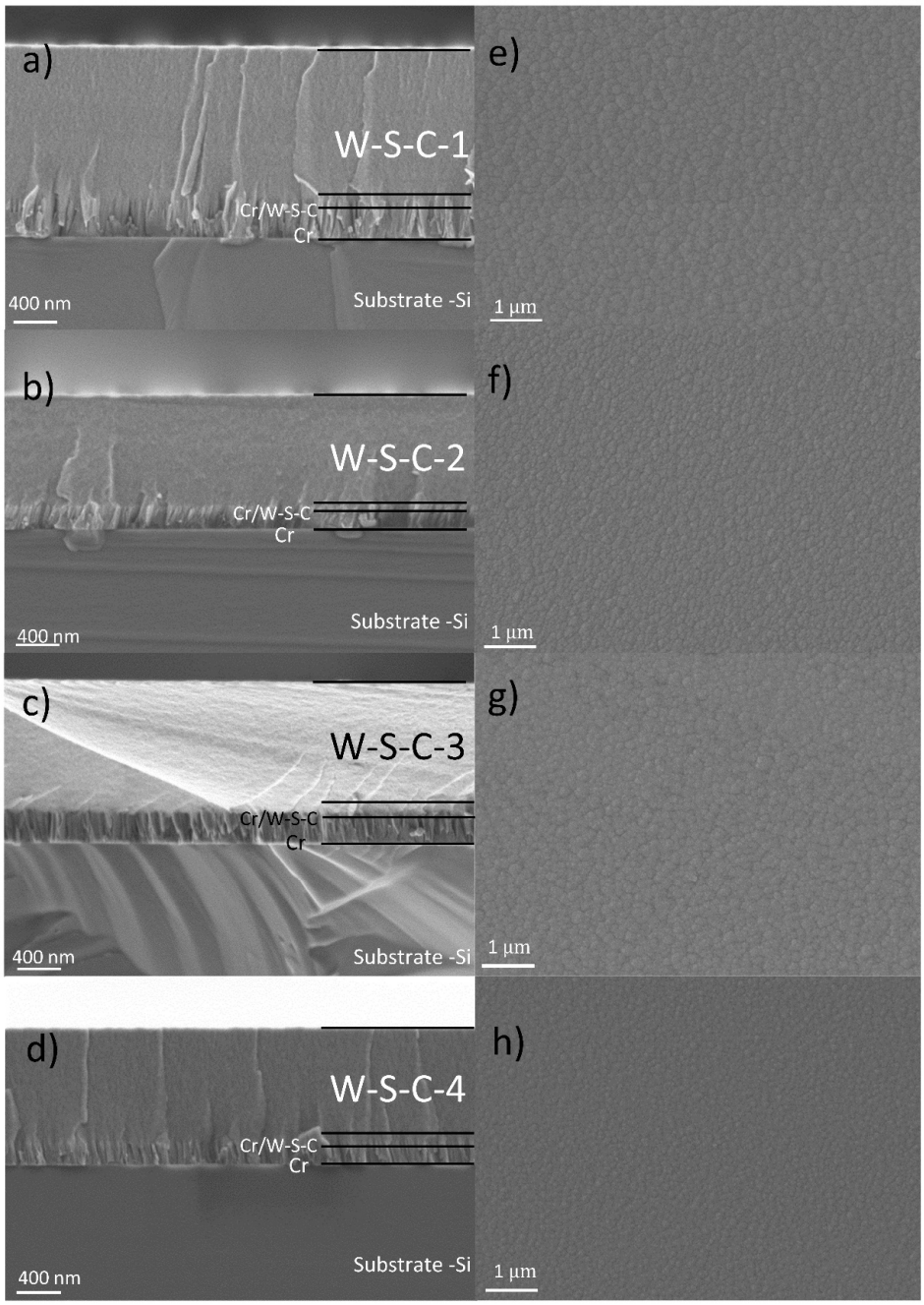

Figure 6-1 Cross-section and top-view micrographs of the coatings a,b) WSC-1 c,d) WSC-2 e,f) WSC-3 g,h) WSC-4

The patterns from the GIXRD (see Figure 6-2) experiments present XRD amorphous structures, characterized by a broad peak at 2θ = 30-45°. The broad peak at this range may contain peaks related to WS_2 and WC planes. A peak often observed in this range is related to the (100) plane of WS_2 located at 2θ = 33° (ICDD no. 00-008-0237), with a tail towards higher angles representing the turbostratic stacking of (10L) WS_2 planes with L having values of 1, 2 and 3 [32]. On the other hand, W_2C (100) peak is also located at 2θ = 34.5° (ICDD no. 00-035-0776), in addition to a WC_{1-x} (111) peak at 2θ = 38° (ICDD no. 00-020-1316) and a W_2C (002) plane located at 2θ~39°. The presence of both tungsten disulfide and tungsten carbide peaks in this region makes the interpretation of the diffractogram difficult. Nevertheless, even if present, the WS_2 and WC crystals are too small to be detected by XRD.

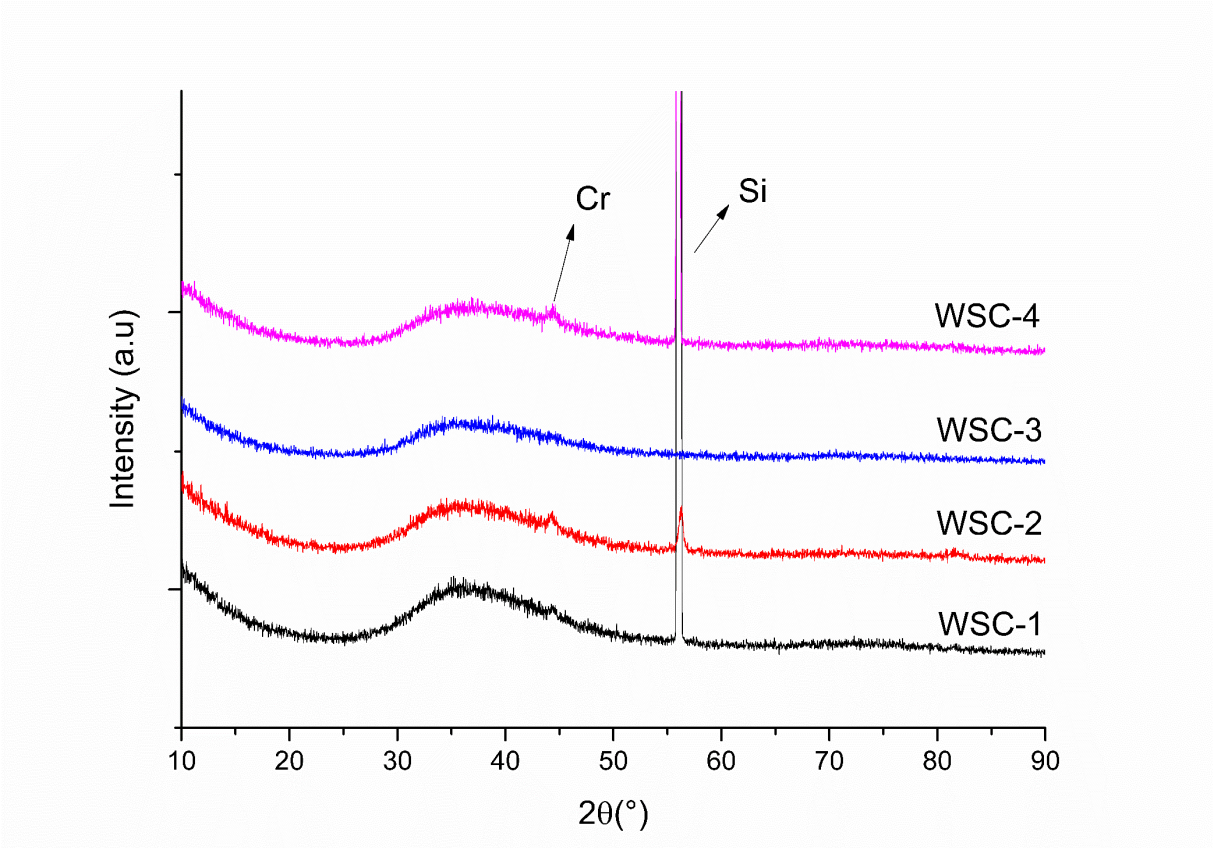

Figure 6-2 XRD patterns of the deposited coatings

To get a better understanding of the microstructure of the coatings, TEM analysis (Figure 6-3) was also performed on the coatings with ~30 nm thickness deposited on TEM grids. The lower magnification images (Figures 6-3 a), c), e), g)) revealed amorphous structures. On the other hand, higher magnification imaging uncovered the presence of fringes with a distance between them of ~0.62 nm which is the typical distance between the basal planes of WS_2, indicating the presence of nanoplatelets of WS_2. These randomly oriented platelets were enclosed in an amorphous carbon matrix and they were present in all coatings. The WS_2

platelets observed in the high magnification micrographs have a typical length of ~5 nm with thickness in the order of a couple of parallel basal planes (typically 2-3). The small crystalline size is in agreement with the broad XRD features. Based on the TEM analysis, all the deposited coatings have a nanocomposite structure consisting of WS_2 platelets enclosed in an amorphous carbon matrix (the latter was identified through Raman spectroscopy, see section 6.3). Besides the different amounts of sulfur and S/W ratios, there is no apparent difference in the microstructure of the coating, as depicted from the TEM analysis. The main influence of the different sulfur content and S/W ratio is very likely on the overall amount of WS_2 in the coatings, which is difficult to depict from the TEM analysis. It is highly probable that the coatings with a lower S/W ratio are more amorphous and contain lesser amounts of crystalline WS_2.

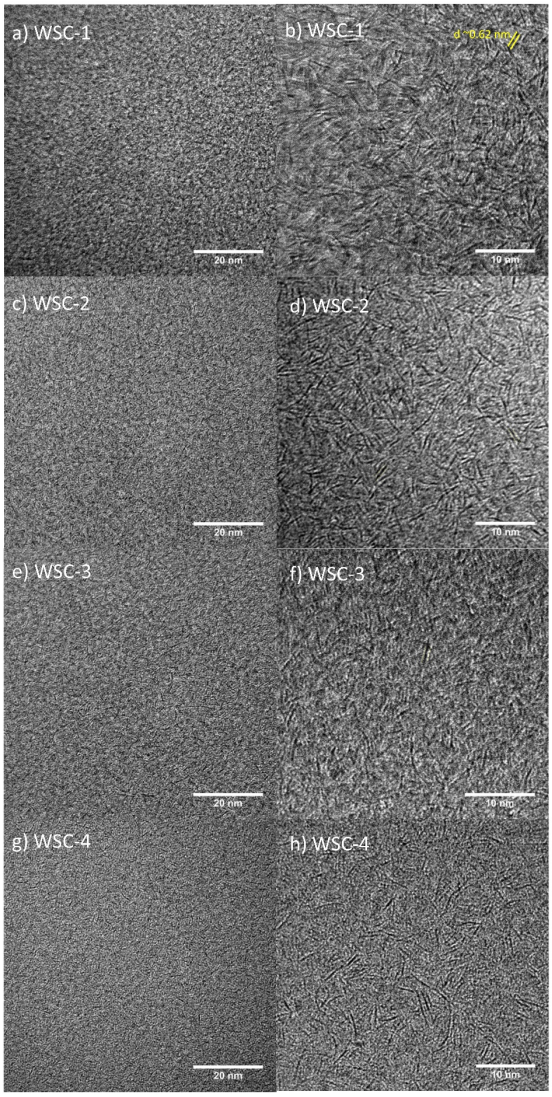

Figure 6-3 Overview and high magnification TEM micrographs of the coatings

6.2 Mechanical properties

6.2.1 Hardness and modulus

The hardness and the reduced modulus of the coatings are shown in Figure 6-4 a) and b), respectively. The maximum hardness of 6.9 GPa was measured for the WSC-1 coating. The coatings WSC-2 and WSC-3 showed quite similar hardness of ~5.2 GPa. The coating WSC-4 was the softest with a value of 4.8 GPa. Similar trends were observed for the reduced modulus, with the WSC-1 coating having the highest value of 98 GPa and WSC-4 having the smallest value with a reduced modulus of 61 GPa.

The hardness of the coatings can be related to their chemical composition. Namely, the hardness of the coatings increases as the overall S/W ratio is reduced, with the WSC-1 coating with S/W ratio of 1.2 being the hardest, while the WSC-4 coating with S/W ratio 1.69 being the softest. The low S/W ratio indicates that there is more tungsten available for the formation of hard tungsten carbide inclusions. Increased amounts of tungsten carbide phases can be the reason for the highest hardness obtained for the WSC-1 coating. As their presence could not be confirmed by the XRD and TEM analysis, they are very likely very small in size or present as an amorphous phase distributed in the a-C matrix [149]. On the other hand, the high S/W ratio (e.g. the coating WSC-4) indicates an increased presence of a softer WS_2 phase, explaining the observed reduction in hardness. Additionally, a higher level of bombardment of the growing films with Ar neutrals can provide densification of the morphology due to increased adatom mobility [112]. In this context, increased density and compactness can further provide higher hardness.

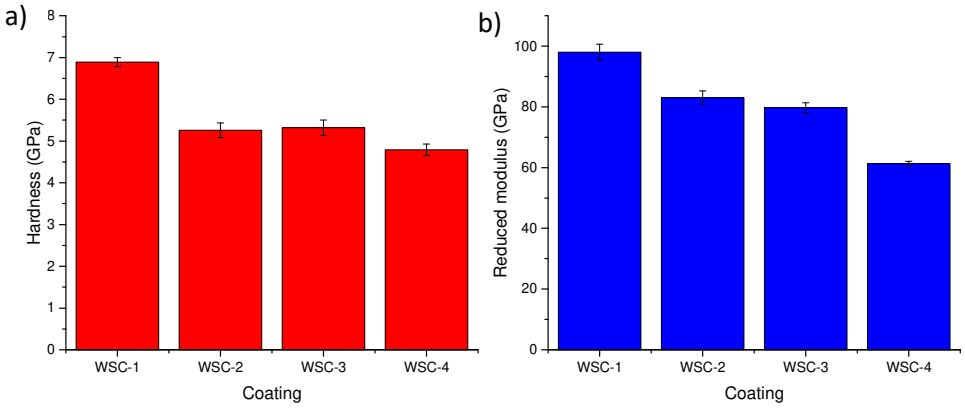

Figure 6-4 a) Hardness and b) Reduced modulus of the coatings

6.2.2 Adhesion-scratch testing

The results obtained from scratch testing are shown in Table 6-3. Lc_1 is the load at which the first cracks are observed, typically on edges of the scratch scar. Lc_2 represents the load at which chipping on the borders of the scratch scar occurs. Lc_3 load is related to the gross delamination of the coating [156]. The values indicated that the harder coatings (lower S/W ratio, WSC-1, and WSC-3) have the worst response to scratch testing with Lc_1, Lc_2 and Lc_3 values of ~6 N, ~17 N and ~23 N. The features observed on the optical and SEM micrographs were quite similar for both coatings and the micrographs and the analysis are from the coating WSC-1. On the other hand, the coatings WSC-2 and WSC-4 displayed much-improved adhesion. The values were fairly comparable for both coatings and the Lc_3 load was up to ~37 N. The micrograph shown is from a representative scratch scar from the coating WSC-4, which had very similar features to the coating WSC-2. It should be noted that the failure modes were different for the 2 groups of coatings. The coatings with worse adhesion (lower S/W ratio) showed larger delaminated areas (see the Lc_3 inset in Figure 6-5 a)) indicating gross spallation. The compressive stresses induced by the indenter cause buckling (evident from the curved cracks present in the scratch scar) of the coating, which can further evolve into spallation depending on the toughness of the coating. The thicknesses of the spalled regions (obtained by 3D profilometry) were typically ~ 600 nm, indicating that the failure occurred within the W-S-C coating or, at most, the gradient Cr/W-S-C layer. This is further confirmed by the EDS mapping performed in the region with delaminated areas. A significant amount of Cr was observed inside the scars with minor presence of Fe, W, and S. EDS performed in the areas outside of the scratch scar where the spalling occurs, did not show the presence of Cr or Fe, indicating that the W-S-C coating is still present there. The failure mode observed for the second group of coatings was different as only buckling within the scratch scar was observed accompanied by chipping on the edges of the scars. The buckling failure mode resulted in the gross delamination of the top-most W-S-C coating from the interlayer as soon as the Lc_3 load was applied. This is evident from the EDS maps shown in the inset of Figure 6-5 b). The darker regions in the Lc_3 micrograph are the areas at which the W-S-C is removed. The signal related to Fe is weaker compared to Cr which confirms that the Cr interlayer is not fully removed from the substrate. Although the deposition of the interlayer and the gradient layer was quite similar for all coatings, different response to the scratch testing was observed. Based on the gross spallation events observed, the harder coatings are very likely more brittle, less tough, and fail due to cohesive damage within the coating. This type of failure can result in worsened tribological performance due to accelerated wear. The response to the scratch testing of the coatings with a higher S/W ratio (WSC-2 and WSC-4) suggests an improved toughness with no gross spallation, which is more promising for the tribological performance.

Table 6.3 Results from the scratch testing-critical loads

Coating	Critical Load (N)		
	Lc_1	Lc_2	Lc_3
WSC-1	6 ± 1	18 ± 1	24.5 ± 1
WSC-2	11 ± 1	23 ± 1	37 ± 1
WSC-3	7 ± 1	15.5 ± 2	20.5 ± 1
WSC-4	9 ± 1	24 ± 1	36.5 ± 1

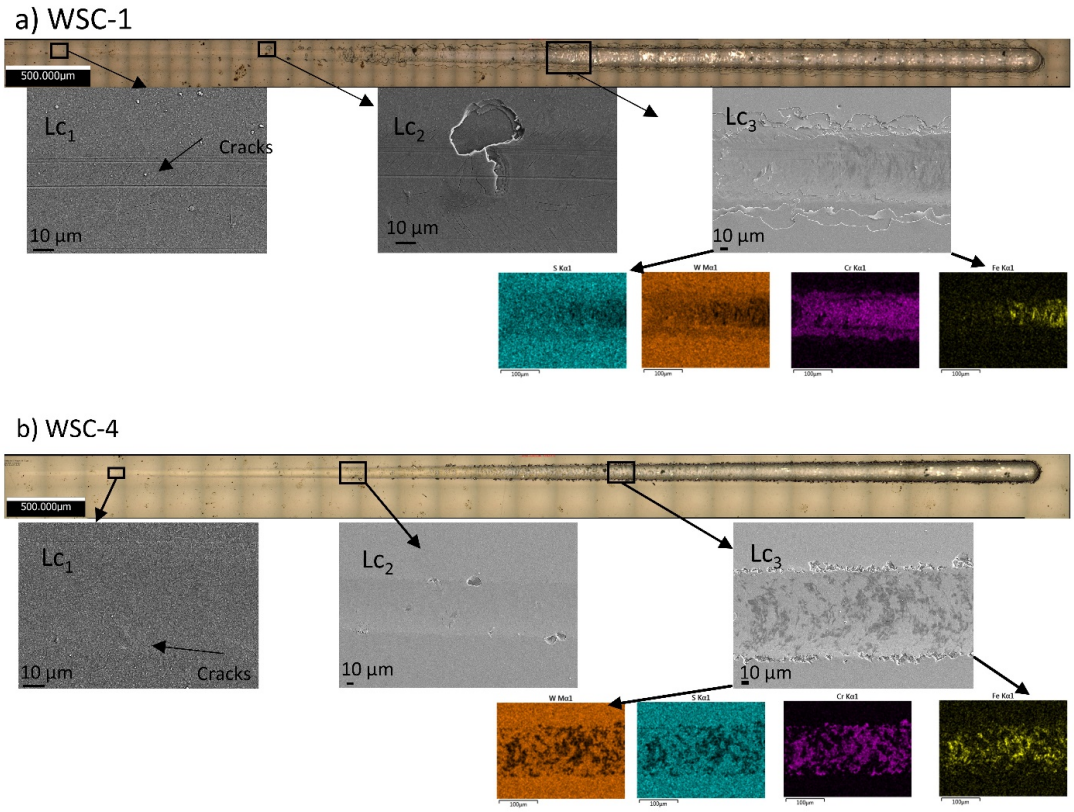

Figure 6-5 Optical and SEM micrographs of the scratch scars obtained for the coatings: a)WSC-1 b) WSC-4

6.3 Tribological performance

6.3.1 Room temperature tests

The evolution of the coefficient of friction (COF) as a function of testing time can be seen in Figure 6-6 a). The specific wear rates of both counterbodies are shown in Figure 6-6 b). The WSC-1 coating showed initially a COF of ~0.3, followed by a running-in stage during which the coefficient of friction drops to a

value of ~0.1. Signs of coating failure depicted from the friction spike can be observed after ~80 seconds of sliding (~4000 cycles). Afterward, the friction dropped to ~0.15 indicating that a tribofilm was again formed. However, a friction spike (COF>0.5) was again observed and as no drop was observed after ~20 sec the test was aborted.

The 3D profilometry performed on the wear track had shown wear depths higher than 1.5 μm indicating that the W-S-C coating was worn-out and the high coefficient of friction is due to the interaction between the substrate/Cr interlayer and the steel counterbody. The specific wear rate was ~1.75 x 10^{-6} mm^3/Nm.

The evolution of the friction coefficient for the coating WSC-2 showed a running-in period of ~90 sec during which the friction dropped to values of 0.1-0.15. The steady-state regime is characterized by friction values that fluctuated between 0.1-0.15, a rapid spike was observed after 550 seconds of testing, and the test was aborted. The specific wear rate was much lower compared to the WSC-1 test with an average value of ~5.5 x 10^{-7} mm^3/Nm.

The performance of the WSC-3 coating is quite similar to the WSC-1 coating. After a short running-in period the coefficient of friction dropped to 0.1, followed by small fluctuations during which a value of 0.2-0.3 was observed. A catastrophic failure marked by a rapid increase in friction was observed after ~175 seconds when the test was stopped. The wear depth measured was up to 3 μm, confirming that the coating was worn-out. The specific wear rate was slightly higher (2.78 x 10^{-6} mm^3/Nm), but in a similar range with the WSC-1 coating.

The best performance was observed for the WSC-4 coating. After a short running-in period of ~20 seconds, the friction dropped to values between 0.12-0.15. During the whole duration of the test, the friction was quite stable in this range and no friction spikes were observed. The wear depth was within the coating thickness (~1 μm) and the specific wear rate calculated was low with a value of 3.73 x 10^{-7} mm^3/Nm.

The ball wear follows the same trends as the wear of the disk, with higher values for sliding against the coatings that were worn through (WSC-1 and WSC-3).

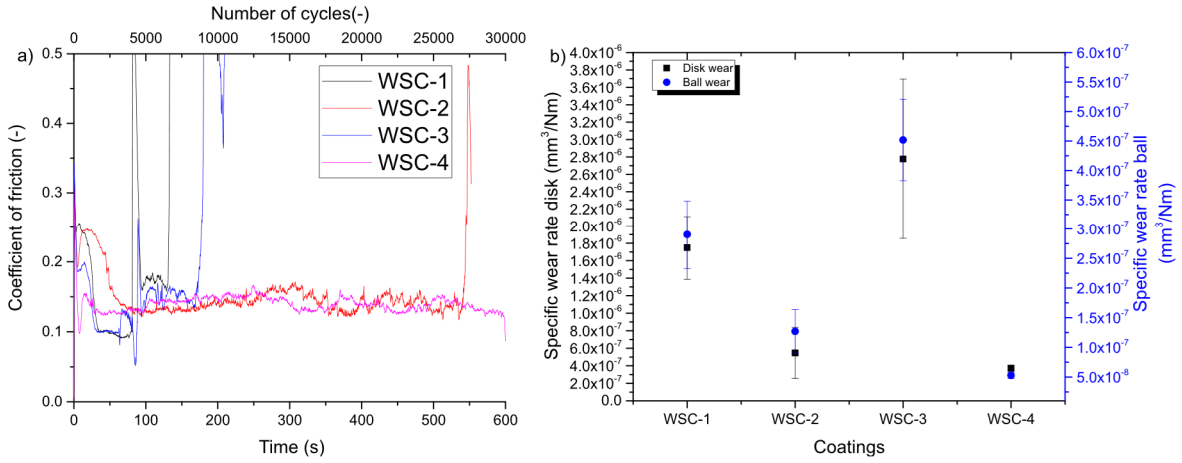

Figure 6-6 Results from the tribological tests at RT a) coefficient of friction b) specific wear rate

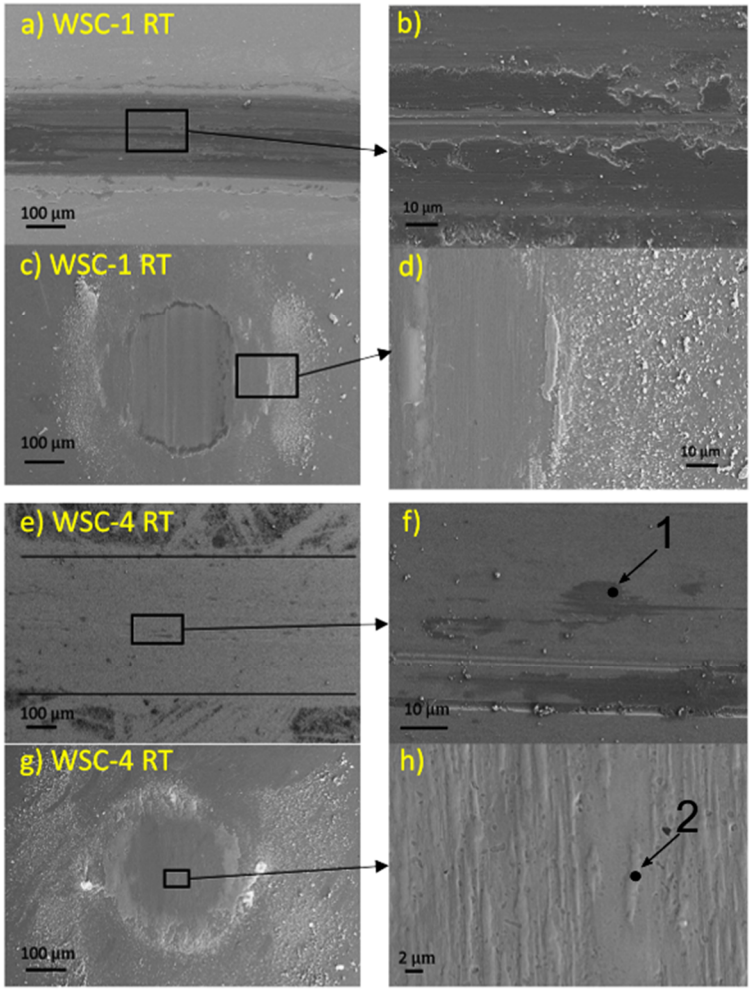

Figure 6-7 SEM imaging after the tribological testing at RT: a,b) WSC-1 disk; c,d) WSC-1 ball; e,f) WSC4-disk; g,h) WSC-4 ball

SEM imaging and Raman spectroscopy were performed on the wear scars for the coatings WSC-1 and WSC-4. The worn-out WSC-1 coating can be observed in Figure 6-7 a). Raman spectroscopy was performed on different areas in the wear tracks and the ball counterbodies after testing the WSC-1 coating (not shown). There were no signs of any crystalline WS_2 (peaks located at ~350 and ~417 cm^{-1} [127]) and the only features observed are the D and G peaks of carbon (1100-1700 cm^{-1}) [104] and some vestiges related to iron oxides (200-300 cm^{-1} [157]) and tungsten oxides (~ 800 cm^{-1} and ~970 cm^{-1} [158].).

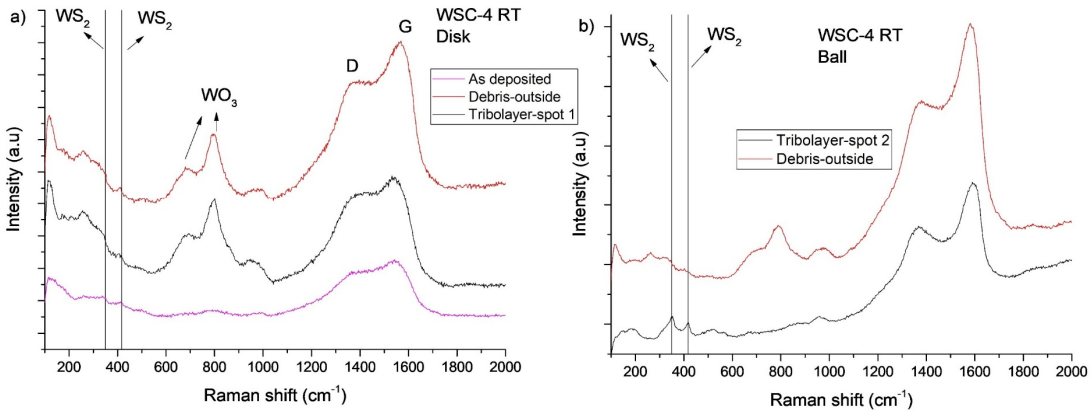

Figure 6-8 Raman spectroscopy performed after testing the WSC-4 coating at RT: a) Disk; b) Ball

On the other hand, the wear scar of the coating WSC-4 revealed a smooth track with areas having layers of material smeared in the direction of sliding (location 1 in Figure 6-7 f)). In its as-deposited state, the coating showed intensity in the region where WS_2 peaks are located, but no sharp peaks were observed, indicating poor crystallinity or small crystalline domains of the WS_2. The Raman spectrum of the tribofilm observed on the disk after testing at RT showed increased intensities in the locations for WS_2 but still, no clear peaks could be observed. In the region of 1100-1700 cm^{-1} the D and G peaks of carbon were observed with location and intensity typical for graphitic carbon. The graphitization is evident since the G peak is positioned at higher Raman shift values (~ 1600 cm^{1}), and the D and G peaks are more separated [104]. The Raman spectrum obtained from the scar on the steel counterbody (location 2 on Figure 6-7 h)) revealed sharper peaks in the region of 350 and 417 cm^{1}, in addition to the D and G peaks from graphitic carbon. Tungsten oxides were also observed in the tribolayers as well as the wear debris, with a higher intensity observed in the latter. Tungsten oxides are very likely produced by reaction of WS_2 with the H_2O from the humid air. Additionally, the Raman analysis on the wear debris showed the presence of graphitic carbon. Based on the Raman analysis, the tribological behavior of this coating at RT is mainly governed by C-based tribofilms, with minor contribution of the TMD phase. This statement is further supported by the fact that

the coefficient of friction (μ~0.15) is often observed for hydrogen-free DLC coatings sliding against steel counterbodies in similar humid air environments (see Ref. [8,133]).

The worsened adhesion of the WSC-1 and WSC-3 coatings can also be related to the premature failure of these coatings. Gross spallation caused by the stresses induced by the bearing steel ball very likely occurred fast. The gross spallation can result in the generation of large particles that cannot be contained in the contact zone and are rapidly removed from the sliding interface, resulting in accelerated wear.

Compared to the results obtained during ambient air testing of the W-S-C coating studied in Chapter 5, those results are similar to the ones obtained for the coatings WSC-2 and WSC-4, although the testing load and the testing configuration was different. A similar coefficient of friction of ~0.15 was also observed for the coating tested in Chapter 5. The wear rate is slightly higher, with values up to 5.5 x 10^{-7} mm^3/Nm measured for the WSC-2 coating, compared to the typical value of ~3-4 x 10^{-7} mm^3/Nm measured after a longer duration sliding in the studies performed in Chapter 5. The higher wear can be related to the harsher high-frequency reciprocating motion. There is always a friction spike during stroke reversal due to the drop in sliding speed and the presence of static friction. These friction spikes can promote accelerated wear of the coatings.

6.3.2 Testing in a dry N_2 environment

The tribological performance under a dry N_2 environment is presented in Figure 6-9 a), while the specific wear rates of the coated disks are presented in Figure 6-9 b). WSC-1 coating failed rapidly; the coefficient of friction rose to the maximum measurable value (~0.5) after sliding for a couple of seconds. Similar behavior was observed for the coating WSC-3, with the only difference being the low friction coefficient (~0.02-0.03) during the initial 20 seconds, after which the coefficient of friction rose rapidly, and the test was aborted.

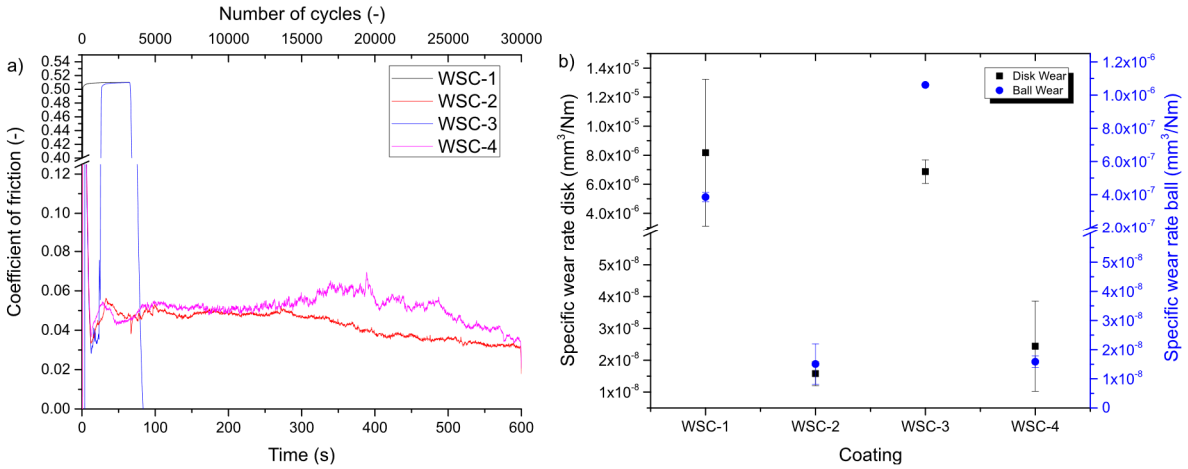

Figure 6-9 Results from the tribological testing under dry N2 a) coefficient of friction b) specific wear rate

The wear depths measured were ~3 µm. The specific wear rates calculated were high, with values of 8.17 x 10^{-6} mm^3/Nm and 6.87 x 10^{-6} mm^3/Nm for the coatings WSC-1 and WSC-3, respectively. Considerable improvement of the behavior is observed for the WSC-2 and WSC-4 coatings. The friction coefficient was relatively low with values around 0.03-0.06 (see Figure 6-9 a)). As expected, the low friction coefficient is accompanied by very low wear rates of 1.58 x 10^{-8} mm^3/Nm for WSC-2, and 2.44 x 10^{-8} mm^3/Nm for WSC-4.

SEM imaging performed after testing is shown in Figure 6-10. The fully worn WSC-1 coating can be seen in Figure 6-10 a). Raman spectroscopy (not shown) was performed in the wear track and the only phase identified was the a-C, very likely due to a thin carbon film that remains in the wear track. There were no Raman intensities in the region related to WS_2. The wear track from the coating WSC-4 was very smooth and featureless (Figure 6-10 f)). Raman spectroscopy was performed in it and a representative spectrum can be seen in Figure 6-11 a). Peaks related to crystalline WS_2 can be observed. Examination of the ball counterbody revealed the presence of material transfer (brighter areas on Figures 6-10 g),h)). The analysis performed in these areas also revealed the presence of WS_2. The intensities related to tungsten oxides were significantly reduced compared to the ones observed from the tribolayers formed during testing at RT, demonstrating the negative effect of the humidity on the oxidation of the WS_2 tribolayers. The D and G peaks of carbon were also observed on both the tribolayers formed on the disk as well as the transferred material on the counterbody. These C-based phases are often unable to provide friction reduction in dry and inert environments [151], unless there is a presence of species (e.g. hydrogen, H_2O) that can adsorb, and passivate the carbon surface. Since the location and intensity of the D and G peaks did not change significantly compared to the as-deposited state, it is also probable that the Raman signal from the carbon material originated from below the lubricious TMD tribolayers. Considering the low coefficient of friction

observed in the present case it is very likely that, although present, the C phase has a minor effect towards the frictional response in the dry N_2 environment. The frictional response in this situation is mainly governed by lubricious WS_2 tribolayers protected from an environmental attack by the dry N_2 gas. The role of carbon is mostly towards the improvement of the mechanical properties and the load-bearing capacity.

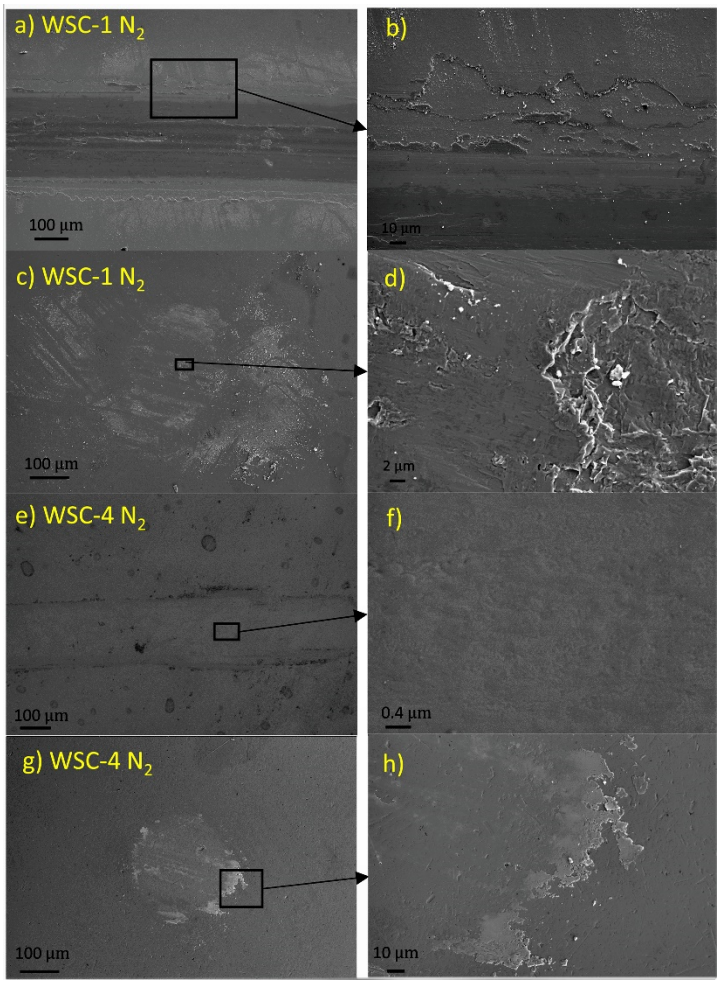

Figure 6-10 SEM imaging of the wear scars after testing in dry N_2 environment: a,b) WSC1-disk, c,d) WSC1-ball e,f) WSC4-disk g,h) WSC4-disk

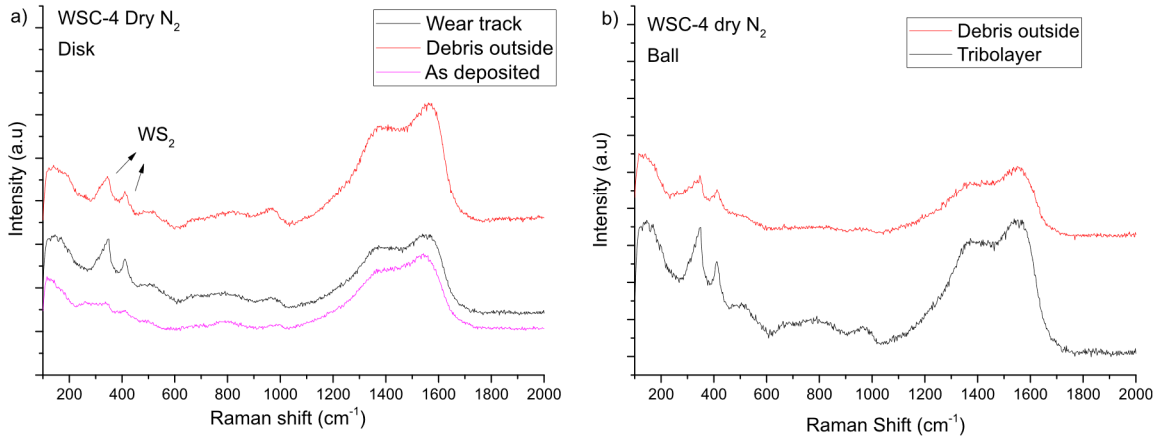

Figure 6-11 Raman analysis after tribological testing of the WSC-4 coating in dry N_2

In the tribological studies on W-S-C coatings performed by Voevodin et al. [79], the authors observed high friction in dry environments for the coatings having low sulfur content (less than 20 % at.), while the coatings having at least 22 at. % of sulfur provided friction reduction. In the present case, although the coatings had more than 22 at. % of S (up to ~27 % for WSC-3), the coatings (WSC-1 and WSC-3) failed to form a low friction WS_2 tribofilm. One of the parameters that can be associated with the tribological response is the S/W ratio. The coatings that failed to form low friction WS_2 tribolayer and hence showed high friction and wear had the lowest S/W ratios (1.2 and 1.4). On the other hand, the coatings that formed a low friction WS_2 tribofilm and provided a significant reduction in friction and wear during sliding in dry environments had higher values of 1.56 and 1.69. It should also be noted that the difference in overall S content for the coatings WSC-2 and WSC-3 is ~1 at. %, but the triboperformance was significantly different, indicating that the S/W ratio should be carefully considered alongside the overall S content. Similarly to the results of the testing in ambient air condition, the worsened performance of the WSC-1 and WSC-3 coatings can also be related to the increased brittleness and lower toughness of the coatings, ensuing in the rapid removal of the W-S-C coating in the form of bigger spalled particles which further results in accelerated wear.

The tribological performance of the coatings with a higher S/W ratio presents an improvement compared to the one of the W-S-C coating tested in Chapter 5. The comparison with that coating further shows that the S/W ratio has a significant impact on the tribological properties of the W-S-C coatings. The significant

improvement is generally related to the wear resistance, as the present coatings have an order of magnitude (1-3 x 10^{-8} mm^3/Nm compared to 2-3 x 10^{-7} mm^3/Nm) improvement in wear resistance.

6.3.3 Testing at elevated temperature (200°C)

The results from the testing at elevated temperatures are shown in Figure 6-12. Surprisingly, the coatings that failed to provide friction and wear reduction during testing at RT and under dry N_2 showed considerable improvement in the tribological performance. After a running-in period of ~10 sec (~500 passes), all coatings showed a tribological response characterized by a fluctuation of the coefficient of friction between 0.02-0.05. The average values are in the range between 0.03-0.05. The wear rates are plotted in Figure 6-12 b). Low wear rates were observed for all coatings, with average values in the range from 9.6 x 10^{-8} mm^3/Nm to 2.6 x 10^{-7} mm^3/Nm. The SEM micrographs and the Raman analysis results are shown in Figure 6-13 and Figure 6-14, respectively. The wear scars of both coatings were smooth with no signs of exposure of the substrate. Raman analysis was performed on the layers of material present on the wear track and smeared in the direction of sliding (spot 1 in Figure 6-13 b)) and spot 3 in Figure 6-13 f)). The Raman spectra indicated that those regions are rich in crystalline WS_2. The intensities related to the carbon phase were very weak. The tribolayers (brighter areas in Figure 6-13 c), d), g), h)) on the counterbody were almost exclusively made of WS_2. The wear debris was rich in graphitic carbon and tungsten oxides.

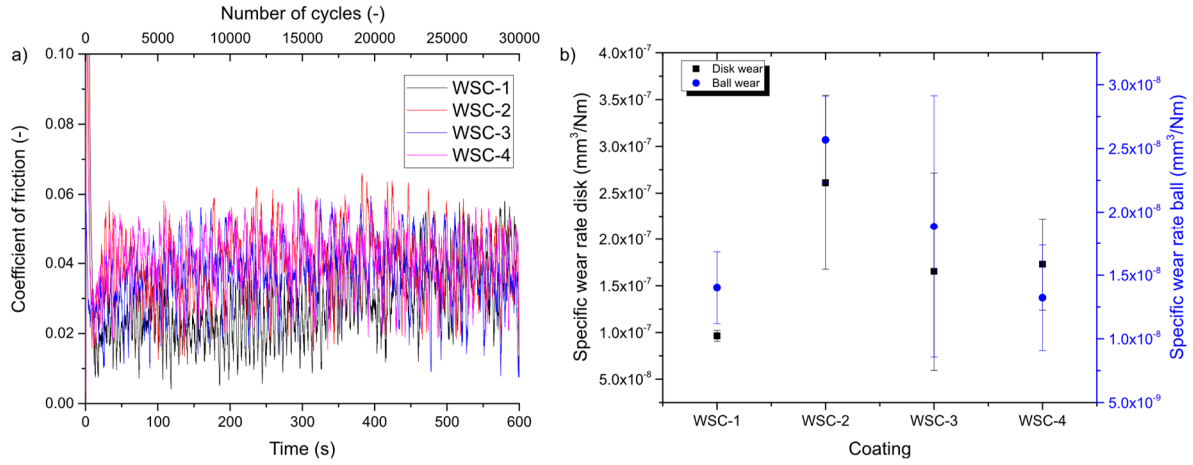

Figure 6-12 Results from the tribological testing at elevated temperature a) coefficient of friction b) specific wear rate

Based on the examination performed, as soon as the testing temperature is increased there is a formation of tribolayers consisting almost exclusively of crystalline WS_2, while the C is preferentially removed from the wear track. The formation of crystalline WS_2 is likely due to the additional energy input into the sliding interface. In a reactive MD (molecular dynamics) study performed by Nicolini et al. [141], it was shown that there is an energy threshold needed to achieve amorphous to crystalline transition in MoS_2, a TMD

compound similar to WS_2. In that context, this energy threshold was likely achieved in the present case as soon as the testing temperature was increased. Furthermore, heating both counterbodies to 200°C would dry the surrounding air and reduce the potentially detrimental effect of the humidity towards the tribological properties of the WS_2 tribofilm [159].

It should be noted that the coatings having a lower S/W ratio (WSC-1 and WSC-3), although having significantly deteriorated toughness, performed remarkably well during elevated temperature testing. This is most probably because the conditions for the accelerated formation of crystalline WS_2 were achieved and a WS_2 rich tribofilm was formed, significantly reducing the friction force acting at the sliding interface and thus reducing the shear stresses acting on the coating.

An excellent tribological performance was also observed for the W-S-C coating studied in Chapter 5. Slightly higher values were observed in the present case since in the reciprocating tribometer there is a friction spike during stroke reversal because of the drop in sliding speed and thus having periods of static friction. The SRV tribometer outputs an instantaneous COF value including the friction spike during stroke reversal. In terms of wear, the present study revealed improved wear resistance, which can be related to the higher number of sliding cycles (30000 compared to the 5000 performed in the study in Chapter 5). The higher number of cycles indicate longer sliding in the steady-state regime, a regime during which the tribolayers are established and the wear is low.

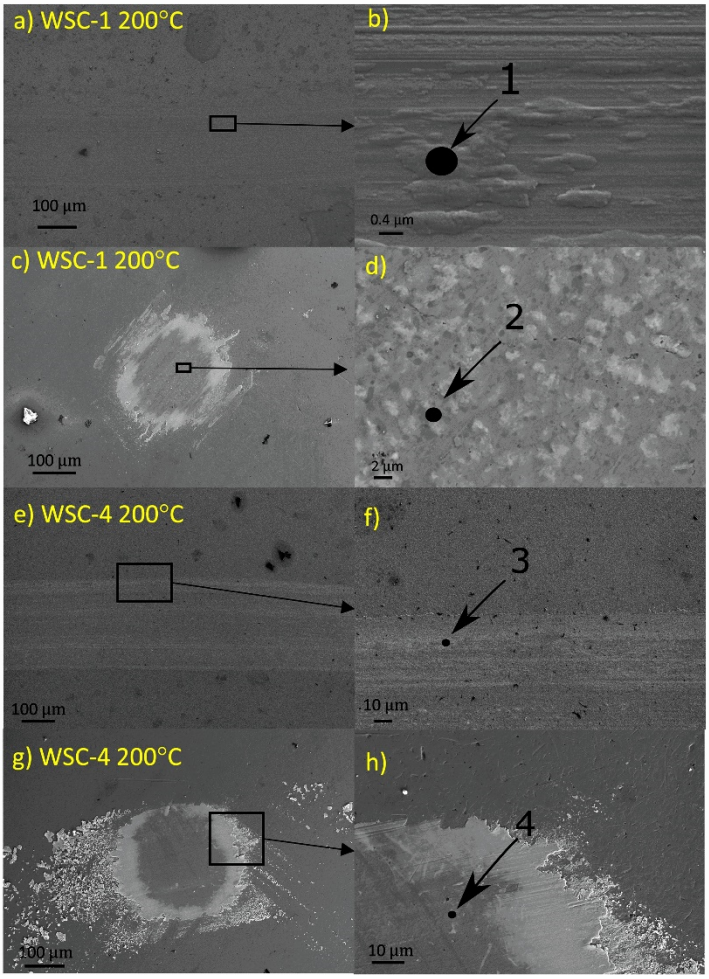

Figure 6-13 SEM micrographs of the wear scars after testing at elevated temperature

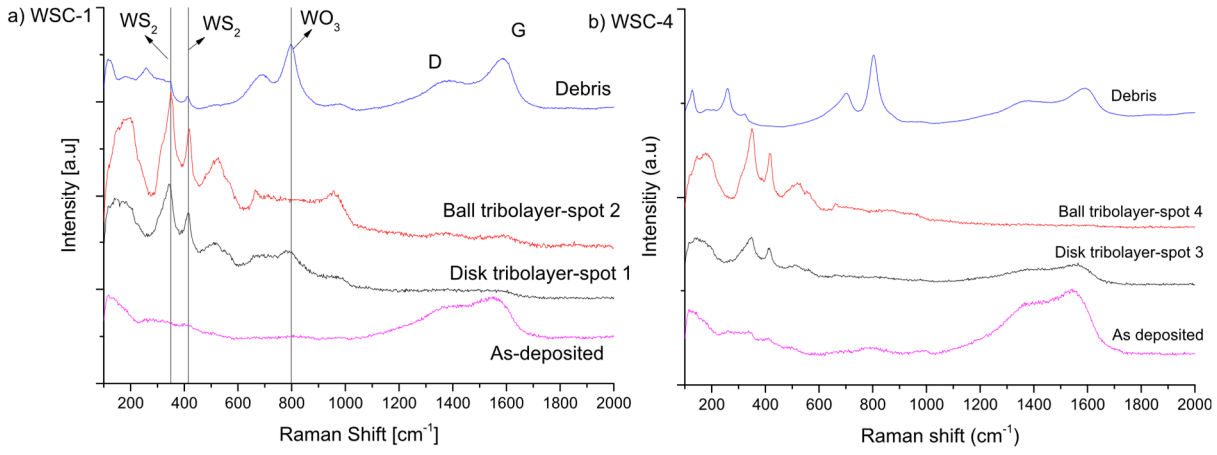

Figure 6-14 Raman analysis of the wear scars after testing at elevated temperatures

6.4 Conclusions

In this chapter, the effect of the substrate location on the chemical composition, microstructure, and tribo-mechanical properties was studied for W-S-C coatings deposited by closed-field unbalanced magnetron sputtering. The main conclusions are:

- The location of the substrates affected the chemical composition, mainly towards the S/W ratio. The Monte-Carlo simulations performed indicated that the differences are mainly due to different level of bombardment of the films with reflected Ar neutrals.
- The deposition process led to a compact featureless cross-sectional morphology and formation of a nanocomposite structure consisting of an amorphous carbon matrix with WS_2 platelets embedded in it.
- The hardness varied between 5-7 GPa, with a higher S/W ratio resulting in lower hardness.
- An adaptive tribological response was observed during dry sliding against bearing steel counterbody in different environments (ambient air, dry N_2, and 200°C) for the coatings having a S/W ratio higher than 1.5.
- The tribological response was governed by graphitic and WS_2 rich tribofilms during ambient air testing. A low-friction WS_2 tribofilm was responsible for the very good tribological response of the coatings that were able to provide friction and wear reduction in dry N_2 and elevated temperature environments.

The deposition of the self-lubricant W-S-C coatings with the processing parameters herein used should be performed with the surfaces to be coated placed at locations resulting in a S/W ratio higher than 1.5. To obtain optimal S/W ratios, deposition at higher pressures can also be considered, to reduce the detrimental effect of the reflected Ar neutrals.

Chapter 7 Synthesis, microstructural and mechanical properties of self-lubricating Mo-Se-C coatings deposited by closed-field unbalanced magnetron sputtering

This chapter extends the study of the previous one for generalizing the upscaling of TMDs in industrial machines. Therefore, an initial attempt of the upscaling of the deposition process of Mo-Se-C coatings is herein presented. The literature reports the deposition of these coatings exclusively in laboratory-scale equipment. The following chapter will demonstrate the potential of the Mo-Se-C coatings, deposited in semi-industrial conditions, for friction and wear reduction in diverse operating environments.

The work undertaken resulted in the following publication:

T. Vuchkov, T. Bin Yaqub, M. Evaristo, A. Cavaleiro, Synthesis, microstructural and mechanical properties of self-lubricating Mo-Se-C coatings deposited by closed-field unbalanced magnetron sputtering, Surf. Coatings Technol. 394 (2020) 125889. doi:https://doi.org/10.1016/j.surfcoat.2020.125889.

7.1 Chemical composition and (micro)structure

The chemical composition, thickness, and roughness of the coatings, as described in Chapter 3, are summarized in Table 7.1. The C-containing coatings have carbon contents between 48 and 53 at. %, with the ones deposited with substrate bias having slightly higher values. The oxygen content is low with values up to 4 at. %. Its incorporation is very likely due to residual oxygen in the chamber and from contamination present in the porous $MoSe_2$.

Table 7.1 Chemical composition, thickness, deposition rate e surface roughness of the coatings

Coating	Elemental composition (at. %)				Se/ Mo ratio	Thickness (µm)/Deposition Rate (nm/min)	Roughness Sa (nm)
	C	Se	O	Mo			
MoSe-15	4.8 ± 0.1	62.3 ± 0.4	2.7 ± 0.4	30.3 ± 0.1	2.07	2.0 / 14.5	26.0 ± 2.4
MoSe-25	3.0 ± 0.1	64.8 ± 0.1	3.7 ± 0.1	28.6 ± 0.1	2.26	2.2 / 17.5	5.7 ± 0.3
MoSeC0V-15	48.8 ± 0.1	32.4 ± 0.1	1.5 ± 0.1	17.4 ± 0.1	1.85	2.2 / 16.3	6.1 ± 0.3
MoSeC0V-25	46.2 ± 0.2	35.1 ± 0.2	2.0 ± 0.1	16.8 ± 0.1	2.1	1.8 / 13.8	5.0 ± 0.1
MoSeC50V-15	51.8 ± 0.4	29.2 ± 0.2	1.1 ± 0.1	18.0 ± 0.1	1.62	1.8 / 12.7	4.8 ± 0.1
MoSeC50V-25	53 ± 0.6	26.8 ± 0.3	1.4 ± 0.1	18.8 ± 0.1	1.43	1.5 / 11.0	3.3 ± 0.1

It should be noted that the pure sputtered $MoSe_x$ coatings exhibited slightly higher oxygen content which is very likely due to their more porous microstructure, being more prone to oxidation. The Se/Mo ratio was close to the stoichiometry ($MoSe_2$) for the pure $MoSe_x$ coatings and the carbon alloyed coatings deposited without substrate bias. For the coatings deposited without substrate bias, increasing the deposition distance resulted in a higher Se/Mo ratio. This is, very likely, due to the reduction of the energy and flux of the energetic Ar neutrals, backscattered from the $MoSe_2$ target, which bombard the growing film. Bombardment of a TMD containing film with energetic species during deposition often results in preferential re-sputtering of the lighter chalcogen atom (Se in the present case) [123]. For the films deposited with substrate bias, there was a reduction of the Se/Mo ratio which is due to the significantly increased bombardment of the growing film with Ar^+ ions. The deposition chamber, equipped with unbalanced magnetrons, in a closed-field configuration, provides increased ionization of the Ar atoms in the proximity of the substrates; by applying a negative bias to the substrates, the growing film is continuously bombarded with Ar^+ ions, resulting in the preferential sputtering of Se. For the coatings deposited with a negative substrate bias, an opposite trend is observed, i.e. the Se/Mo ratio decreases as the TSD is increased. This phenomenon can be understood if the incoming ion-to-atom ratio is considered. As

the deposition distance is increased, there is a drop in the deposition rate for the coatings deposited without a negative substrate bias (compare MoSeC0V-15 and MoSeC0V-25). In other words, the flux of incoming atoms is reduced. When a negative substrate bias is applied on the substrates, the incoming ions are extracted from the discharge and their flux is very likely quite similar at both distances (15 and 25 cm). Therefore the incoming ion-to-atom ratio would be higher for the substrates placed at a higher distance, and, thus, the preferential re-sputtering of the Se atoms is amplified.

The compositions attained for these Mo-Se-C coatings show an improved stoichiometry (Se/Mo ratio) compared to the W-S-C coatings were lower ratios of chalcogenide to transition metal atoms (X/M) was observed. It must be noted that the deposition conditions were quite similar, with the same deposition pressure and quite similar target currents and voltages. The improved ratio can be related to the reduced energy of the backscattered neutrals in the case of $MoSe_2$. The energy distribution of the reflected Ar neutrals during the sputtering of WS_2 and $MoSe_2$ is illustrated in Figure 7-1. The data was obtained from SRIM simulations. In the case of WS_2, the reflected Ar neutrals have an energy of up to 300-350 eV, compared to a maximum value of 200-250 calculated for $MoSe_2$. The fraction of reflected Ar neutrals was slightly higher for the sputtering of $MoSe_2$ target with a value of ~11 % compared to a ~10 % fraction obtained for the WS_2. The average energy value was significantly higher for WS_2 (~103 eV), compared to $MoSe_2$ (~57 eV). Based on this data it is expected that the bombardment with energetic backscattered Ar neutrals will be lower for the Mo-Se-C coatings and, thus, there is a lower re-sputtering of the lighter Se atoms from the growing film. The higher Se/Mo ratio can further be related to the lower difference in the atomic mass of the sputtered species (Mo and Se). Due to the smaller mass difference, it is expected that the scattering of the Se and Mo atoms will be more similar compared, for example, to the scattering of the W and S atoms in the case of W-S-C coatings.

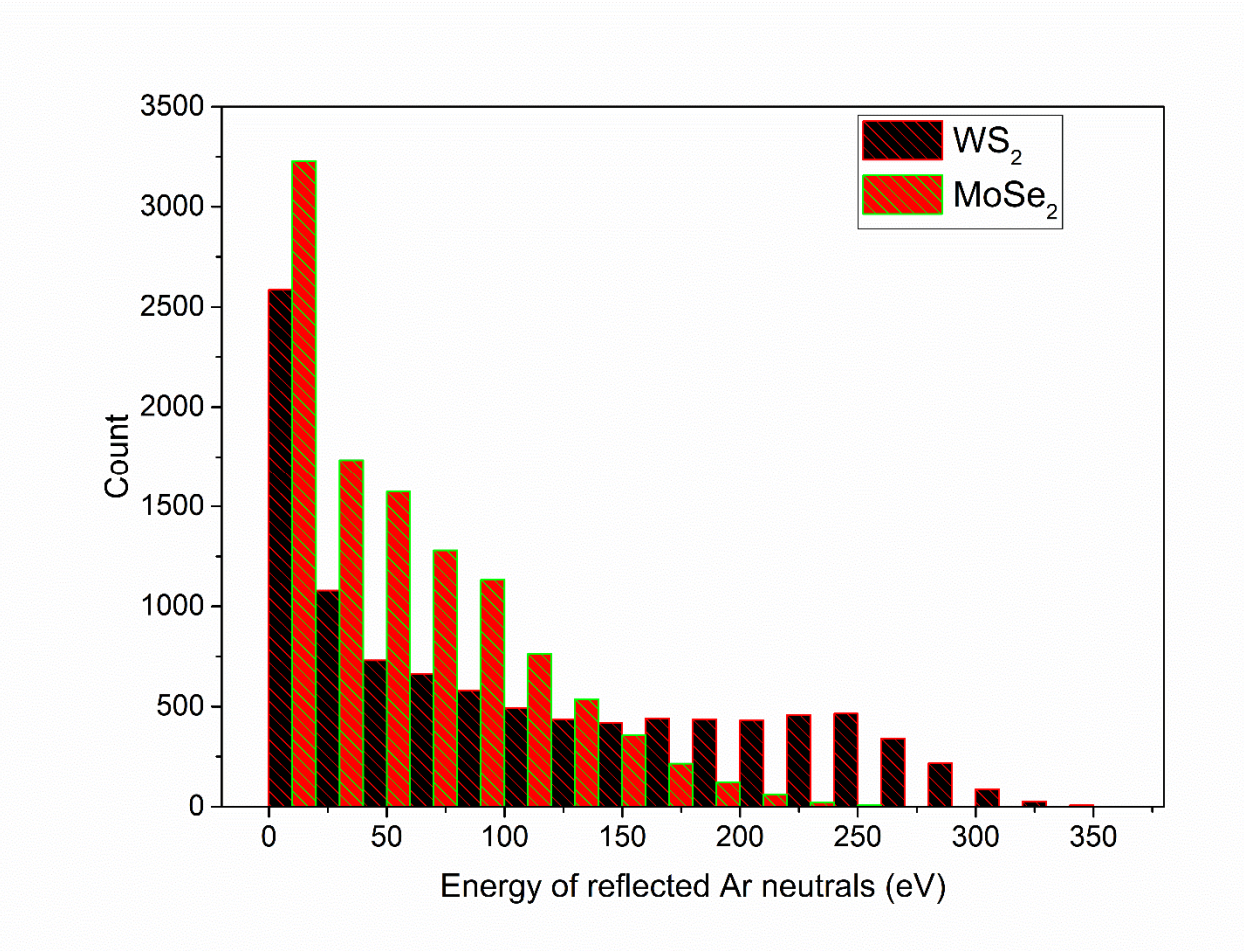

Figure 7-1 Energy distribution of the backscattered Ar neutrals during sputtering of WS_2 and $MoSe_2$

The electron micrographs of the deposited coatings are shown in Figure 7-2. The pure sputtered coatings have a columnar porous structure, which is typical for sputtered TMD coatings. The micrographs also revealed that the coating deposited at a longer target-to-substrate distance (TSD), with a higher Se/Mo ratio contains a more porous worm-like structure (see Figure 7-2 d)). On the other hand, the pure MoSe coating deposited at 15 cm, although still porous, exhibits a denser fibrous morphology. This coating, even though deposited at a smaller target-to-substrate distance, is thinner, which can be related to its increased compactness and density. The increased compactness is very likely due to increased bombardment of the growing film with backscattered argon neutrals causing increased adatom mobility and reduced atomic shadowing. As carbon is co-sputtered, significant densification of the coatings occured. The columnar morphology was still evident but the intercolumnar porosity is reduced (see Figure 7-2 e)). With the addition of carbon, the top-surface morphology became cauliflower-like (Figure 7-2 f)). The densification of the coatings is further evident by a similar deposition rate between the carbon alloyed coatings and the pure coating, besides the additional sputtering of the graphite targets. The application of substrate bias results in

further densification of the coatings, resulting in compact and featureless cross-sectional morphologies (Figure 7-2 g)). The densification of the morphology is due to the increased adatom mobility induced by the continuous bombardment of the growing film with Ar^+ ions [160]. The deposition rate, in this case, was further reduced compared to the coatings deposited without substrate bias (e.g. from ~16.3 to 12.7 nm/min for the coating deposited at 15 cm). The top-surface morphology is of a cauliflower-type for the coating deposited at 15 cm, while for the coating deposited at 25 cm the cauliflower features disappeared and smoother, more featureless morphology was observed. The disappearance of the cauliflower features is very likely due to the increased incoming ion-to-atom ratio causing increased re-sputtering of the growing film and smoothening of the surface. In terms of roughness, the pure films exhibited increased roughness compared to their carbon alloyed counterparts. The highest roughness was observed for the MoSe-15 coating, with an average value of 26 nm. The MoSe-25 coating, although having a more porous microstructure has a smaller average roughness of 5.7 nm. The carbon alloyed coatings were smoother, with the ones deposited with substrate bias having the smallest values (e.g. S_a=3.3 nm for the MoSeC50V-25 coating).

The morphological features observed for the Mo-Se-C coatings illustrate the importance of the bombardment of the film with energetic species. For example, both MoSeC0V-15 and WSC-1 (Chapter 6) have very similar carbon content but the morphological features were significantly different. The former coating has an underdense columnar morphology while the latter has a very compact, featureless morphology. The main difference between these 2 coatings is the ratio between chalcogen atoms and transition metal atoms, with the latter having a significantly lower value (S/W ratio of ~1.2 compared to the Se/Mo ratio of 1.85). In this context, it should be noted that a carbon content of ~50 at. % does not ensure a dense and compact morphology.

The X-ray diffractograms from the coatings are presented in Figure 7-3. XRD performed on the pure MoSe coatings revealed they are crystalline. The XRD patterns reveal the presence of various $MoSe_2$ crystallite orientations with the strongest reflections being the (002) at 2θ ~ 12.8°, (100) at 2θ ~ 31.5°, (103) at 2θ ~ 37.8° and (110) at 2θ ~ 55.8° (ICCD card No. 01-077-1715). Additional peaks stemming from the Cr interlayers were observed at 2θ ~ 44.4° and 2θ ~ 81.7°. One major difference between the MoSe-15 and MoSe-25 coatings was the ratio ((002) / (100)) between the intensities related to the (002) and (100) planes. The (002) orientation represents the presence of planes that are closely parallel to the substrate (basal orientation), planes that play a crucial role in the tribological properties. On the other hand, the (100) orientation represents the basal planes that are closely perpendicular to the substrates (edge orientation), and in this case reorientation of the crystal is needed to provide low friction [159]. The MoSe-15 coating has a higher ratio of (002) / (100) indicating that the coating has a preferential orientation with the basal

planes closely parallel to the substrates, compared to the MoSe-25 coating which has a lower ratio of (002) / (100), hence the coating has a preferential orientation with the basal planes being closely perpendicular to the substrate. The main difference in terms of deposition condition for these films is the target-to-substrate distance. This parameter mainly affects the bombardment of the growing film with energetic species, with higher bombardment for the substrates placed closer to the target. In a study performed by Muratore and Voevodin [161], they reported increased basal (002) orientation for MoS_2 films when optimized deposition rates are achieved while there is an optimal bombardment of the growing film with energetic species. In the present study, the deposition rate for the coating with basal orientation is comparable (~14.5 nm/min) with the one reported in the study by Muratore and Voevodin (~13 nm/min). Furthermore, a deposition distance of 15 cm seems to be optimal in terms of the bombardment of the films with energetic species, thus providing conditions for an increased presence of basally oriented (002) crystals. As the deposition distance is increased to 25 cm the bombardment with energetic species (flux and energy) is reduced, with its evident effect on the orientation of the crystals.

As carbon was co-sputtered with $MoSe_2$ the XRD patterns revealed broad amorphous-like features. The diffractograms contained a broad peak in the 2θ range of 30-50°. This broad feature is often associated with turbostratic stacking of (10L) $MoSe_2$ planes, with L having values of 0, 1, 2, 3, and 4. This turbostratic stacking of the (10L) planes is often observed for sputtered TMD coatings [113,162]. Nevertheless, even if present these crystallites are too small to be resolved by XRD.

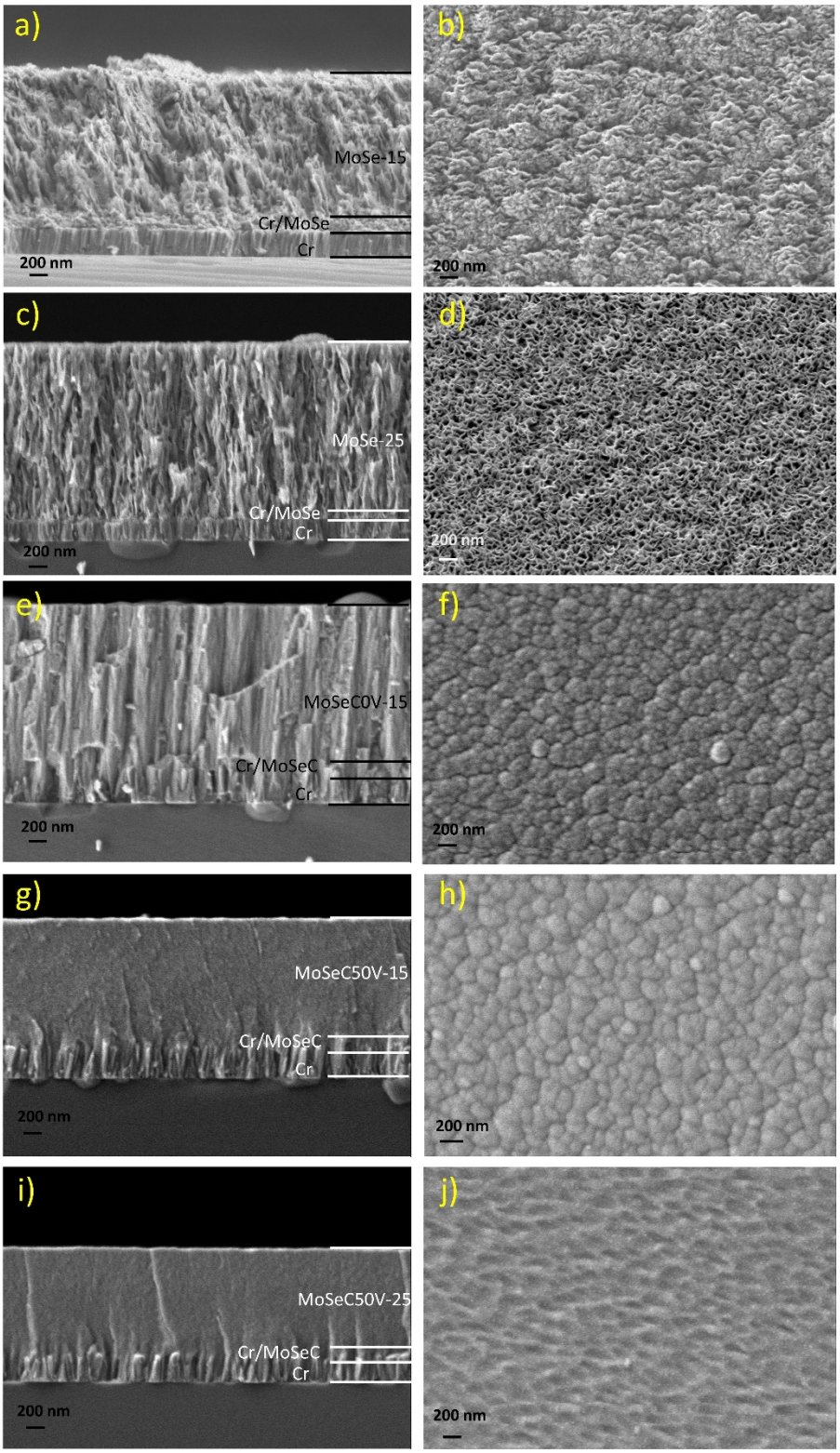

Figure 7-2 Cross-sectional and top-view micrographs of: a,b) MoSe-15; c,d) MoSe-25 e,f) MoSeC0V-15; g,h) MoSeC50V-15; i,j) MoSeC50V-25

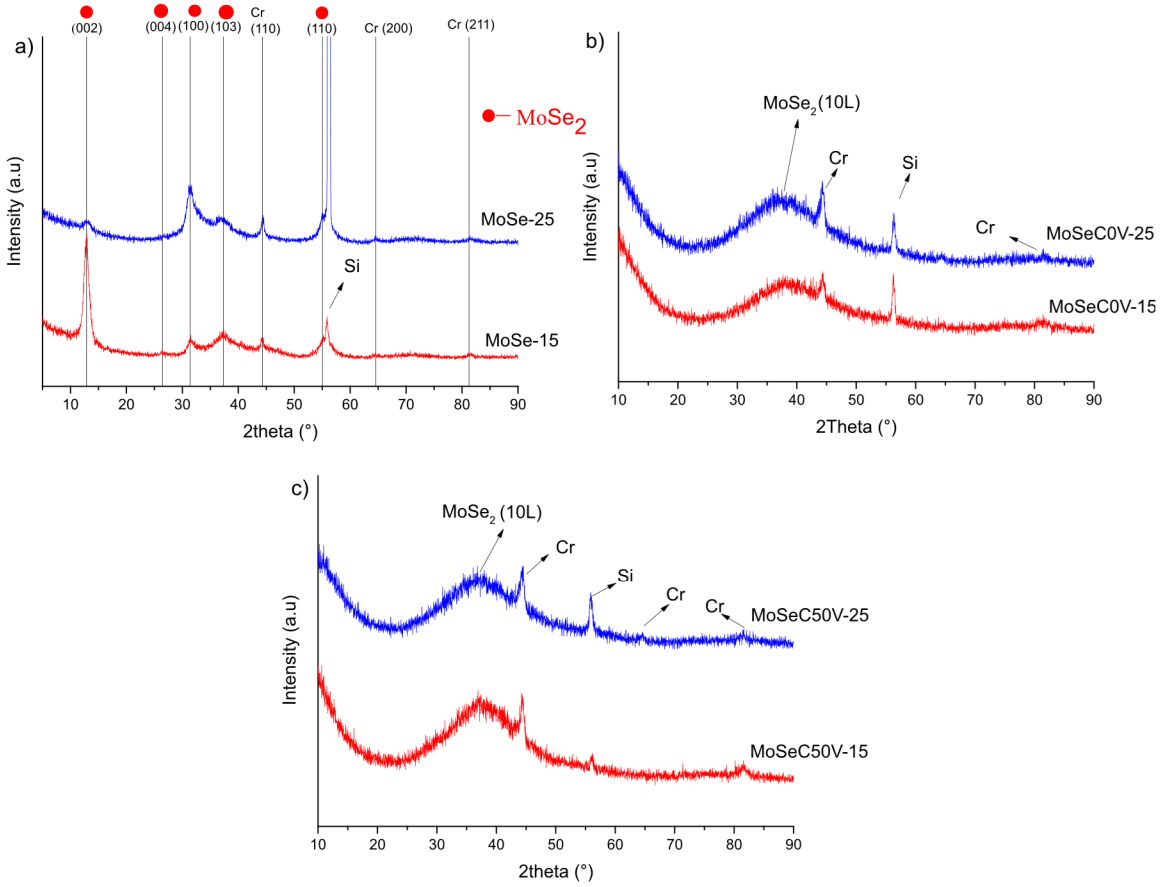

Figure 7-3 XRD diffractograms from a) MoSe b) MoSeC0V and c) MoSeC50V coatings

The nanostructure was further assessed by TEM, with the results presented in Figure 7-4. For the pure sputtered coating MoSe-15, crystallites with length up to ~15 nm and thickness of up to ~15 layers of $MoSe_2$ are observed (see Figure 7-3 a)). The distance between the fringes observed in Figure 7-3 a) is ~0.65 nm, which corresponds to the interplanar distance of the (002) planes of $MoSe_2$. The TEM micrographs from the C alloyed coatings revealed the presence of fringes with spacing typical for the (002) planes $MoSe_2$ (~0.65 nm), but with much smaller crystallite sizes, embedded in an amorphous C (a-C) matrix (the presence of the a-C matrix was identified by Raman spectroscopy). The co-sputtering of carbon restricted the growth of the $MoSe_2$ crystallites, and their length is reduced to ~5 nm with a thickness of a couple of $MoSe_2$ planes (typically 2-4). It should be noted that the coating deposited with a substrate bias, although having a lower Se/Mo ratio, still contained crystallites of $MoSe_2$. The small crystallite size observed in the TEM studies agrees with the broad XRD features observed for the carbon-containing coatings.

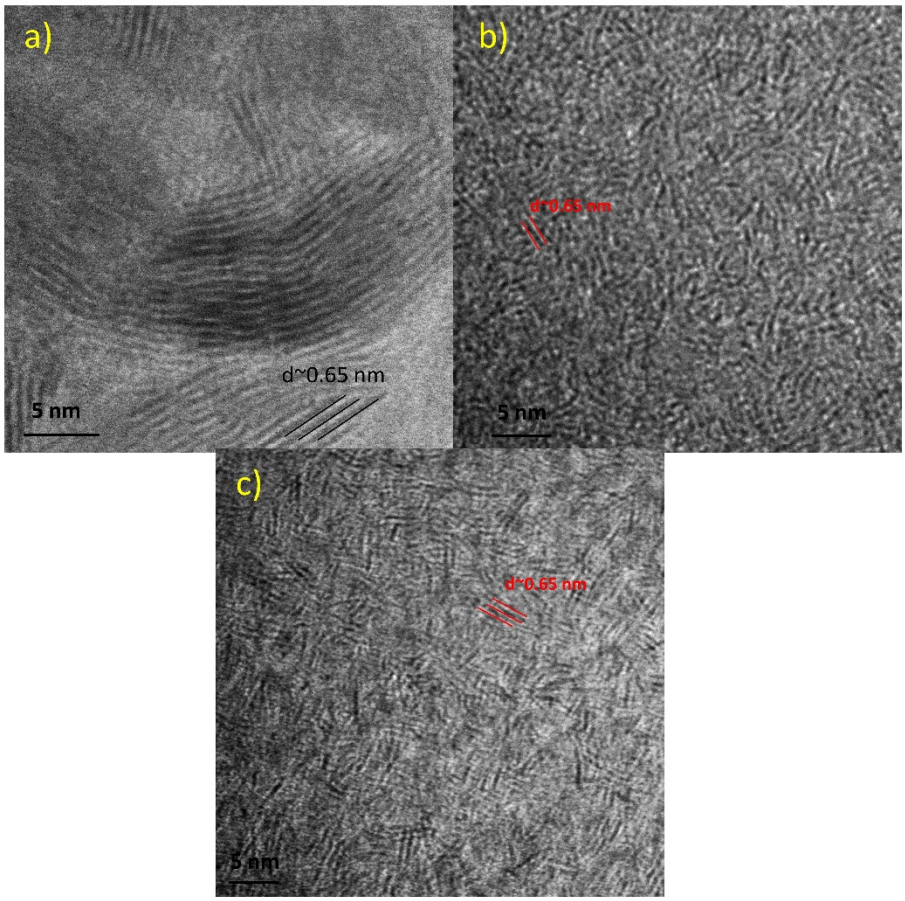

Figure 7-4 TEM micrographs of the coatings a)MoSe-15, b)MoSeC0V-15, c)MoSeC50V-15

The coatings were further analyzed by Raman spectroscopy and the results are presented in Figure 7-5. The Raman intensities related to the $MoSe_x$ phase are typically between 100-400 cm^{-1}. The strongest peaks identified for the pure sputtered MoSe films (see Figure 7-5 a)) are the E_{1g}, A_{1g}, and $E_{2g}{}^1$ located at Raman shift values of ~170 cm^{-1}, 237 cm^{-1} and 287 cm^{-1}, respectively [163]. No additional intensities were observed in the range of 800-1600 cm^{-1}, representing the lack of presence of Mo oxides and carbon. The spectra related to the MoSeC coatings are presented in Figure 7-4 b) and c). The features observed for all coatings are quite similar. Intensities are observed in the area related to the $MoSe_2$ phase, but the peaks could not be resolved. These features point out to a reduced structural quality of the $MoSe_2$ phase, which is in agreement with the X-ray diffraction analysis as well as the TEM analysis. Broad features related to the minor presence of Mo oxides are observed at Raman shift values between 700 and 950 cm^{-1} [164]. The region between 1000 and 1700 cm^{-1} contains the D and G bands of carbon. The carbon peaks were deconvoluted using a Lorentzian lineshape for the D band and a Breit-Wigner-Fano (BWF) for the G peak, following the recommendations by Ferrari and Robertson [104]. The fitting resulted in a ratio between the intensity of

the D and G peak (I(D)/I(G)) of ~ 1. The location of the G peak was between 1560 and 1580 cm^{-1}. The ratio between the intensities of the D and G peak and the position of the G peak is typical for an a-C phase.

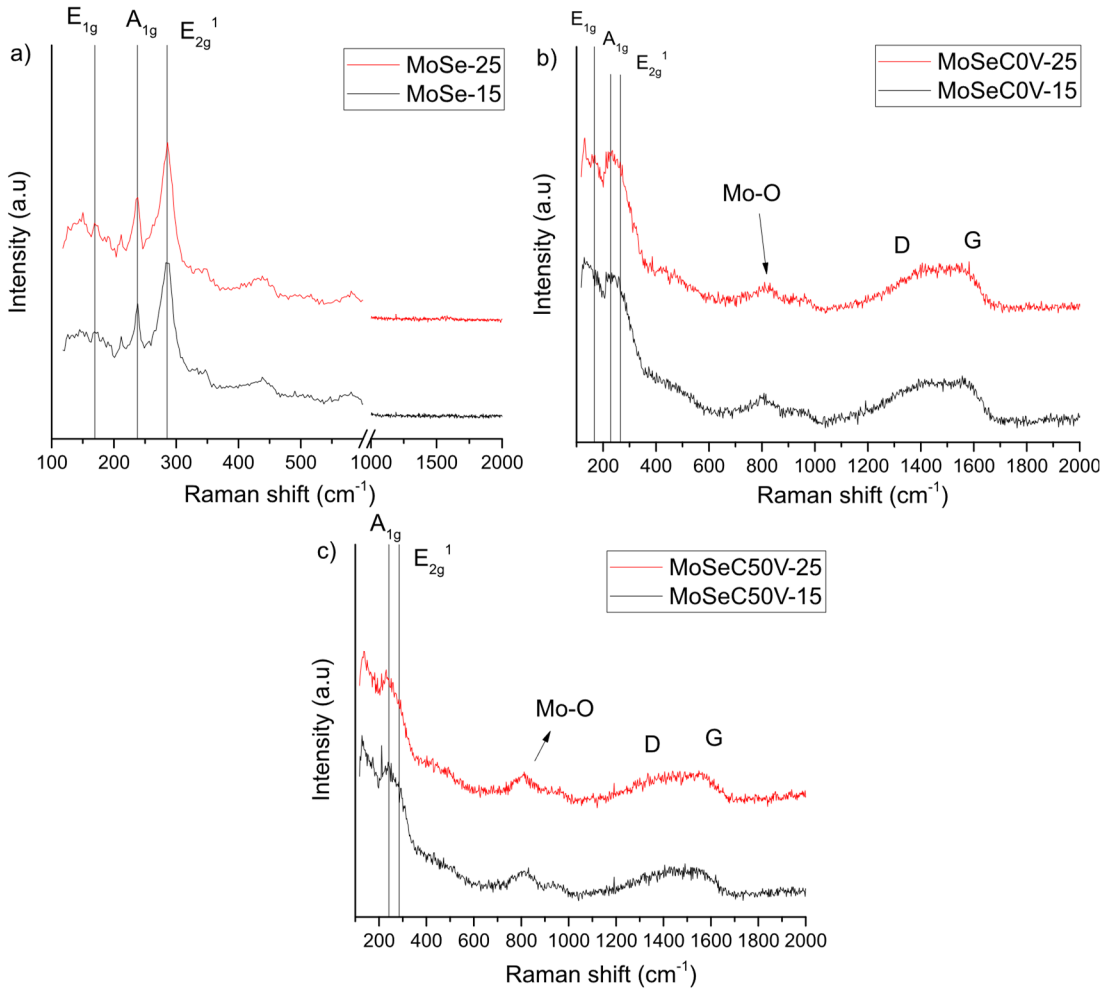

Figure 7-5 Raman spectroscopy results a) MoSe b) MoSeC0V c) MoSeC50V

7.2 Mechanical Properties

The results from the nanoindentation are shown in Figure 7-6. The pure MoSe coatings presented low hardness with values of 0.67 and 0.47 GPa for MoSe-15 and MoSe-25, respectively. The slightly higher average hardness of the MoSe-15 coating can be related to its higher density and lower Se/Mo ratio (as discussed in section 7.1). Significant hardness increase is achieved as carbon is added to the coatings. For the carbon alloyed coatings deposited without substrate bias, the hardness values are ~5 and ~4 GPa for the coatings deposited at a TSD of 15 and 25 cm. The hardness difference can be related to the Se/Mo ratio. This ratio can be associated with the amount and, very likely, the crystallinity of the softer $MoSe_x$ phase present in the coatings. In this context, the higher the Se/Mo ratio, the lower is the hardness. This relation

can be observed for the carbon alloyed coatings as well as for the pure MoSe coatings. The hardness of the carbon alloyed coatings deposited with substrate bias is higher (7.1 and 7.8 GPa) compared to the coatings deposited without substrate bias. Biasing the substrate significantly improved the density and the compactness of the coatings due to concurrent bombardment with Ar^+ ions. From this point of view, the increased density can provide a hardness improvement. Furthermore, the bombardment with Ar^+ resulted in preferential re-sputtering of Se from the growing film and the reduction of the Se/Mo ratio, which can further contribute to the increase in the hardness. The reduced modulus of the coatings follows the same trends as the hardness with higher modulus for the harder coatings, except for the pure MoSe coatings were the opposite trend was observed.

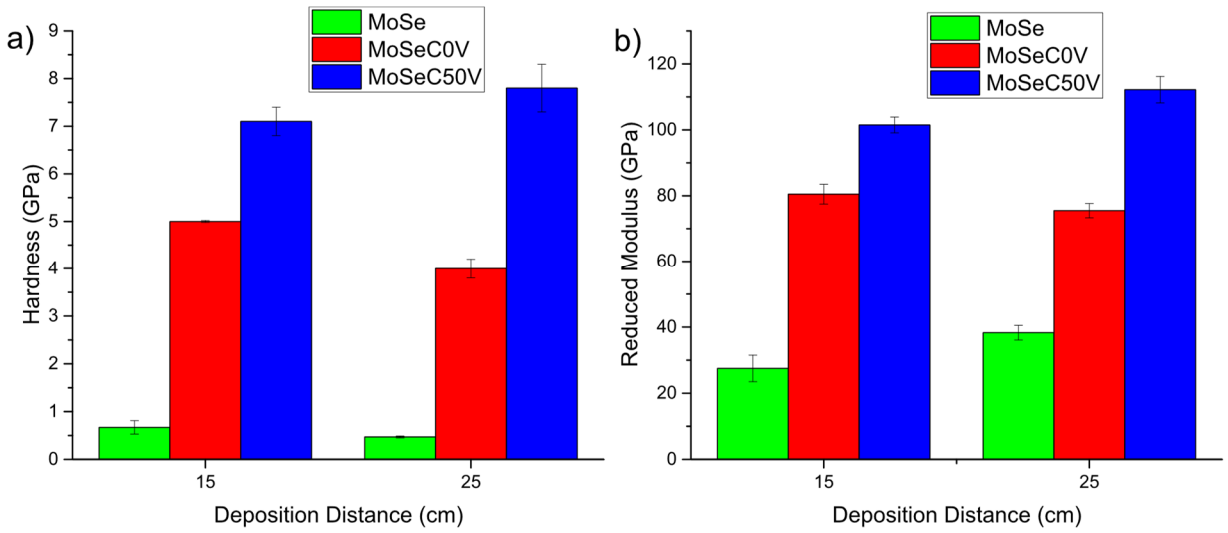

Figure 7-6 a) Hardness and b) Reduced Modulus of the coatings

7.3 Adhesion

The critical loads from scratch testing are shown in Table 7-2. The Lc_1 load is related to the appearance of chevron cracks at the border of the scratch track. Lc_2 is the load at which chipping and spallation occur at the borders of the scratch track. Lc_3 load represents the gross delamination of the coating [156].

Table 7.2 Critical loads from the scratch testing

Coating	Critical Load (N)		
	Lc_1	Lc_2	Lc_3
MoSe-15			5.5 ± 0.1
MoSe-25			3 ± 0.1
MoSeC0V-15	12.5 ± 0.5	24.5 ± 1	>60
MoSeC0V-25	10.5 ± 1	25.5 ± 1	>60
MoSeC50V-15	18.5 ± 2	52 ± 2	>60
MoSeC50V-25	35 ± 1	>60	>60

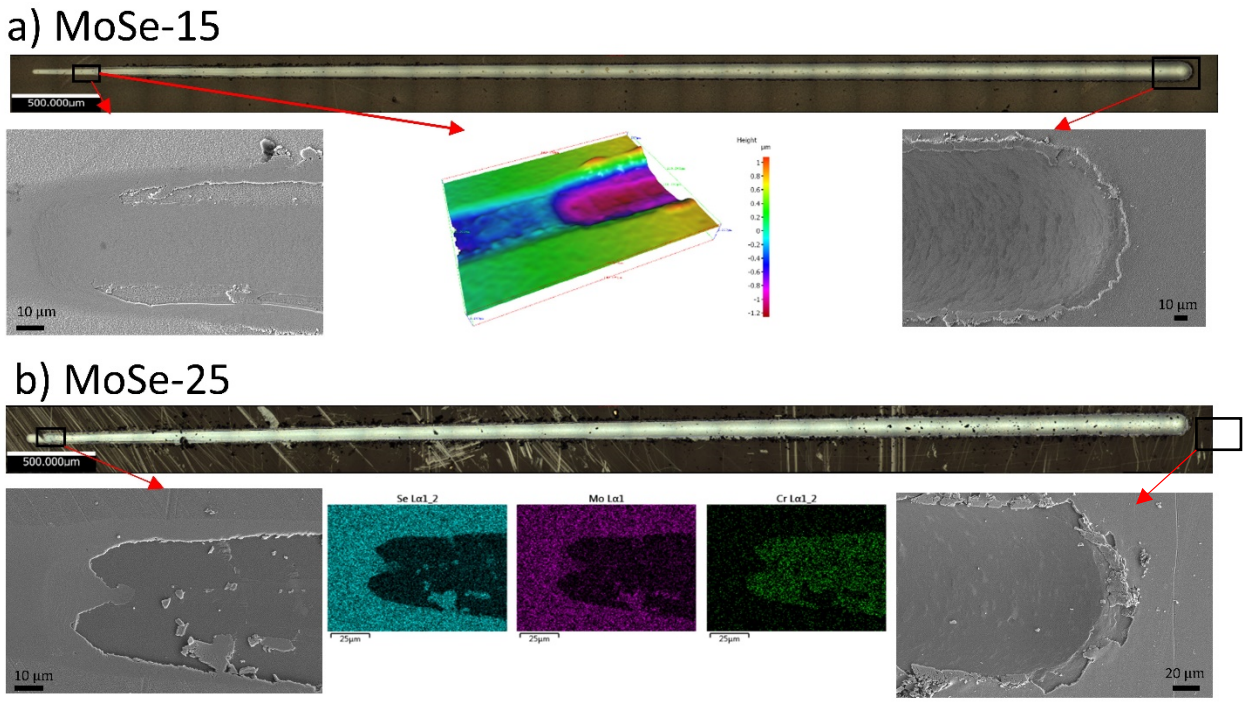

Figure 7-7 Scratch scars of the Pure MoSe coatings

The MoSe coatings have quite low critical loads of ~5.5 and 3 N for the coatings deposited at a TSD of 15 and 25 cm, respectively. Due to the low hardness of these coatings, severe ploughing can occur under the stresses induced by the indenter and smeared material can be observed on the sides of the scratch scars, like in the case of the MoSe-15 coating. In this case, the failure at ~5.5 N of load is identified due to the significant drop (~ 0.8 µm) in residual depth observed in the 3D reconstructed detail (inset in Figure 7-7

a)). EDS analysis was performed in the same area and it revealed the presence of $MoSe_x$ even after the failure spot, indicating its presence, even though a significant portion of the coating was removed. The lower thickness of the MoSe layer after the failure spot was confirmed by the presence of Cr during EDS analysis (not shown). Unlike the MoSe-15 coating, the failure of the MoSe-25 coating was marked by the complete delamination of the $MoSe_x$ top layer from the Cr interlayer (see the EDS maps in Figure 7-7 b). The difference in adhesion between the MoSe coatings can be related to the crystalline orientation of the coatings. The MoSe-15 coating has a basal (002) preferential orientation with the low shear strength planes being parallel to the substrate. These planes can accommodate the tangential loads induced by the indenter, thus reducing the shear stresses, resulting in no gross detachment of the coating as well as smearing of the MoSe material in the direction of sliding. The MoSe-25 coating has an edge (100) preferential orientation with the low-shear strength planes being perpendicular to the substrate. As the indenter is sliding across the coating, strong shear stresses arise as the low shear strength planes are not aligned to the surface, resulting in detachment of the coating from the Cr interlayer. The results are in agreement with previous studies on sputtered TMD coatings (see Ref [165,166]) where films with basal (002) preferential orientation often have better adhesion and better fracture toughness than the edge (100) oriented TMD films.

The coatings co-sputtered with carbon have improved adhesion compared to the pure MoSe ones. The coatings deposited without substrate bias (MoSeC0V) have similar adhesion with the first chevron cracks appearing at ~ 10-12 N (Lc_1). Spalling on the edges of the track was observed at a load of ~ 25 N (Lc_2). The failure mode observed until the end of the test was mostly spallation at the edges of the track with minor chipping in the middle of the track. No gross delamination was observed in this range of loads. Significant improvement is observed for the coatings deposited with substrate bias. The first appearance of cracks is observed at higher loads, 18 N and 35 N for the coatings MoSeC50V-15 and MoSeC50V-25, respectively.

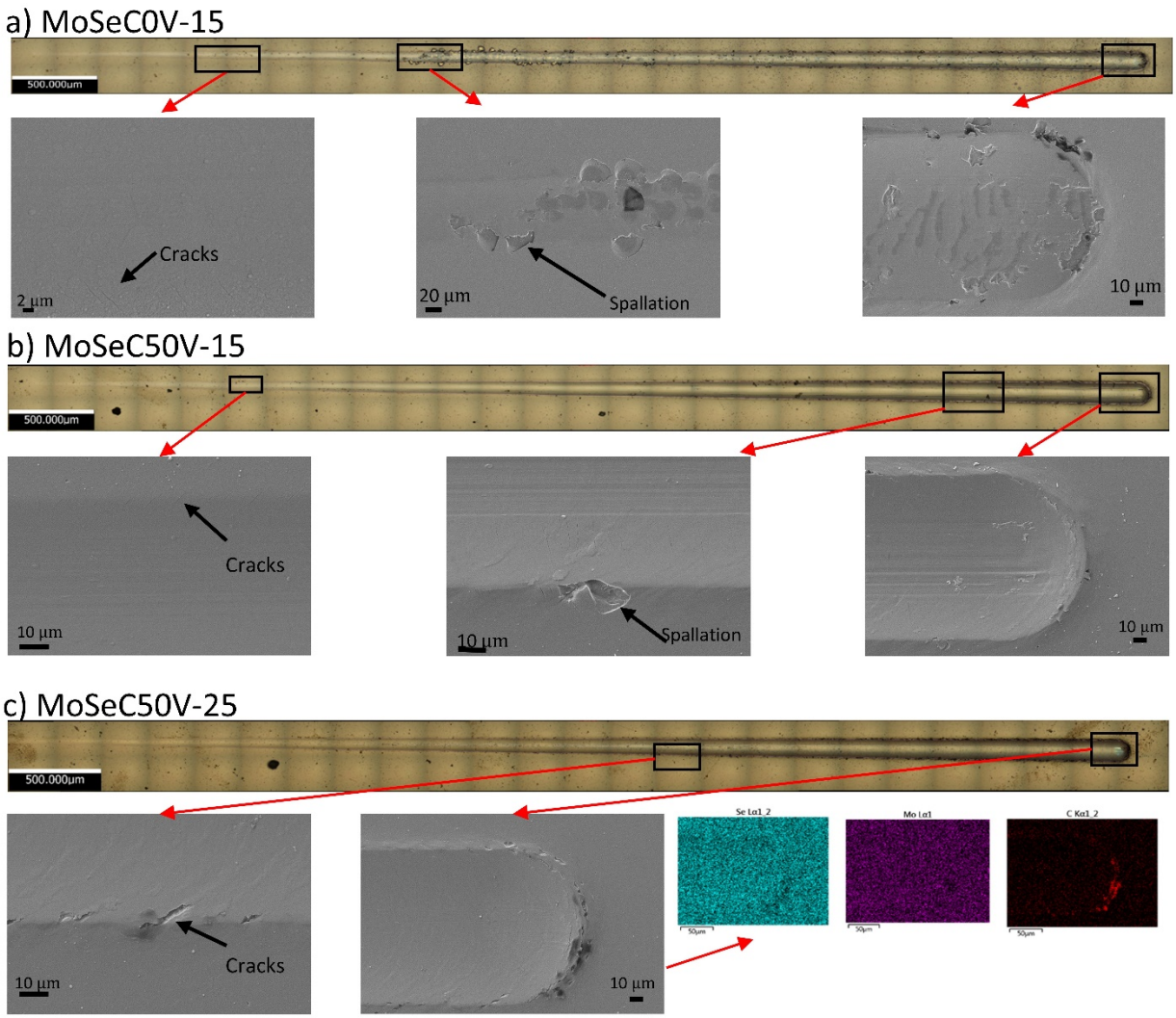

Figure 7-8 Scratch scars from the testing of the carbon alloyed coatings a) MoSeC0V-15 b) MoSeC50V-15 c) MoSeC50V-25

Spallation at the edges of the scar is observed at ~ 52 N for the coating MoSeC50V-15, but the occurrence of these spallation events was rarer compared to the coating deposited without substrate bias (compare the end of the scratch scars shown in Figure 7-8 a) and 7-8 b)). The Lc_1 load for the MoSeC50V-25 coating is even higher (~35 N) and no spallation is observed until the end of the test. To further confirm this, EDS mapping was performed in an area located at the end of the track (inset in Figure 7-8 c)) and no signal related to Cr is detected and the presence of Mo and Se is uniform inside and outside the scratch scar. Based on these results, having a compact featureless morphology is beneficial towards the adhesion of the coating. The coating deposited without substrate bias has a more porous columnar morphology, thus having more

columnar boundaries which are detrimental in terms of microcrack initiation and propagation and subsequently more prone to spallation [167].

The SEM micrographs from the Rockwell C indents are shown in Figure 7-9. The pure MoSe coatings have insufficient adhesive strength marked by delamination around the whole circumference of the imprint. An HF5 adhesion class was assigned for the MoSe-15 coating due to the fact the delaminated areas are not large, and there is very likely a thin MoSe layer present in the delaminated area (see the inset in Figure 7-9 a)). For the MoSe-25 coating, an HF6 class was assigned as the delaminated areas were bigger and the high magnification micrograph in

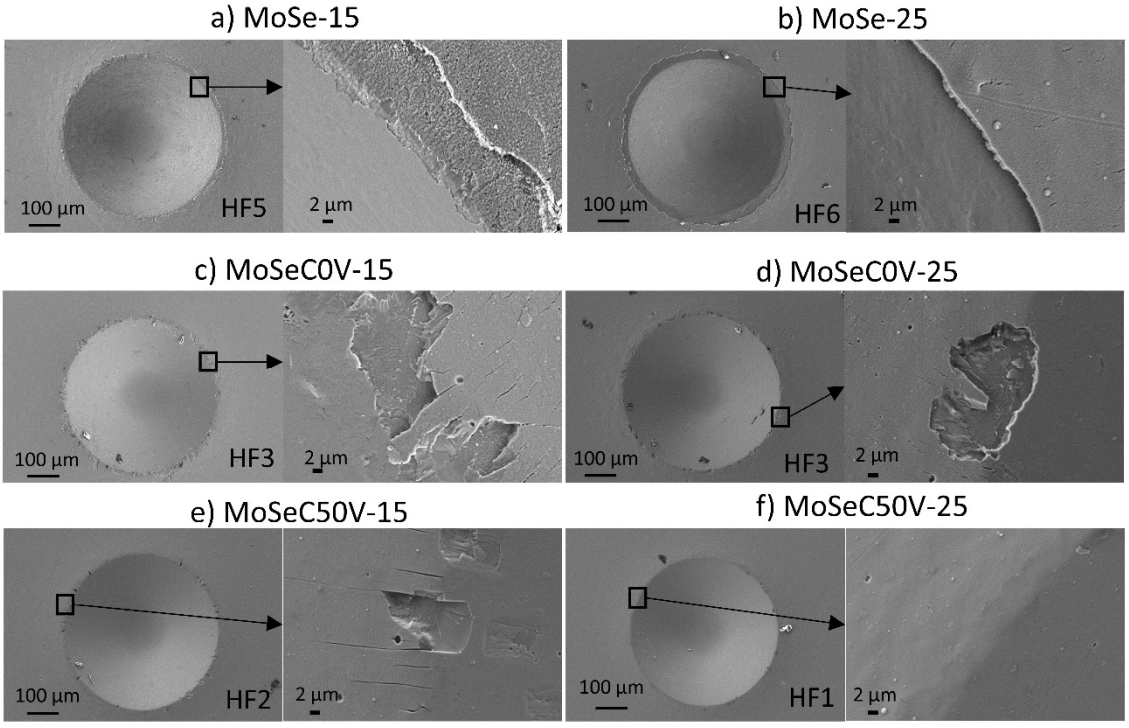

Figure 7-9 SEM micrographs from the Rockwell C adhesion tests a) MoSe-15 b) MoSe-25 c) MoSeC0V-15 d) MoSeC0V-25 e) MoSeC50V-15 f) MoSeC50V-25

Figure 7-9 b) shows the complete detachment of the coatings with no signs of MoSe remains in the delaminated region.

For the MoSeC coatings deposited without substrate bias, an acceptable adhesion was observed and an adhesion class of HF3 was assigned. Spallation and cracking were observed around the indent, but the spalled areas were not interconnected, and no gross delamination was observed. Additional improvement was observed when substrate bias was used for the MoSeC coatings. The coating deposited at a TSD of 15 cm (MoSeC50V-15) has an adhesion class of HF2 as minor spallation was observed, accompanied by cracking. The best adhesion was observed for the MoSeC50V-25 coating, which showed very minor

cracking, and an HF1 adhesion class was assigned. Similar trends were observed in terms of adhesion between the scratch testing and the Rockwell C adhesion tests, with the coatings having more compact featureless cross-sectional morphologies (MoSeC50V) having the best adhesion strength.

7.4 Tribological properties

7.4.1 Room temperature behavior

The results from the tribological tests performed at room temperature under normal ambient air atmosphere are plotted in Figure 7-10. The MoSe coating deposited at 15 cm has a coefficient of friction of ~0.08 in the initial testing stages and during the test, the COF slightly increases with a final value of ~0.09-0.1. No friction spikes are observed indicating that there was no metal-to-metal contact and the friction was governed by the $MoSe_2$ phase. On the other hand, the pure MoSe coating deposited at a TSD of 25 cm had a smaller initial COF of ~0.03-0.04, but a continuous increase of the friction coefficient occurred, indicating that the $MoSe_2$ tribofilm was removed and, at least partially, there was metal-to-metal contact. The test was aborted as soon as the friction increased more than 0.2 in order to prevent severe interaction between the steel ball and the steel disk. The difference in the tribological response between the pure $MoSe_2$ coatings is very likely due to the orientation of the crystallites, as the response of the coating with more basal oriented crystals (higher (002) / (100)) was much more stable. Additionally, the coating deposited at TSD of 15 cm was denser, and slightly harder, which can also be beneficial towards the tribological response. Both carbon alloyed coatings deposited without substrate bias have a similar tribological response with COF values of ~0.08 in the steady-state regime. The frictional response of the coating deposited without substrate bias at a TSD of 25 cm is characterized by a frictional spike after ~330 seconds of sliding followed by a fluctuation of the COF with values between 0.08 and 0.2. The friction spike is very probably due to partial spallation of the coating leading to severe metal-to-metal contact followed by a continual drop of the COF indicating that tribolayer was again being established. The coatings deposited with substrate bias had a similar response in the steady-state regime compared to the coatings deposited without substrate bias, with the main difference being in the running-in stage. The running-in stage for the coatings deposited with substrate bias was characterized by much higher friction of ~0.12-0.15 and this stage lasted for ~200 and ~100 seconds for the coatings deposited at 15 cm and 25 cm, respectively.

In terms of wear, the worst performance was observed for the MoSe-25 coating with a value of ~ 7 x 10^{-6} mm^3/Nm. Surprisingly, the MoSe-15 coating (wear rate of 5.5 x 10^{-7} mm^3/Nm) performed slightly better than the carbon alloyed coatings deposited without substrate bias which have wear rates of ~7.5 x 10^{-7} mm^3/Nm. The highest wear resistance was observed for the carbon-doped coatings deposited with substrate bias, where low values were measured. The wear of the counterbodies followed similar trends as the wear of the disks. Higher counterbody wear was observed after the tests at which instabilities in the frictional

response was registered. As previously mentioned, these instabilities are due to severe interaction of the counterbody with the metallic interlayer (or the substrate) leading to increased wear of the counterbody.

The frictional response of the Mo-Se-C revealed an improvement compared to the W-S-C coatings with similar composition. The typical COF of ~0.08 is significantly lower compared to the values of ~0.15 often observed for W-S-C coatings. In terms of wear, the coatings deposited with a negative substrate bias (MoSeC50V) had a very similar wear resistance compared to the W-S-C ones (specific wear rate of ~3 x 10^{-7} mm^3/Nm).

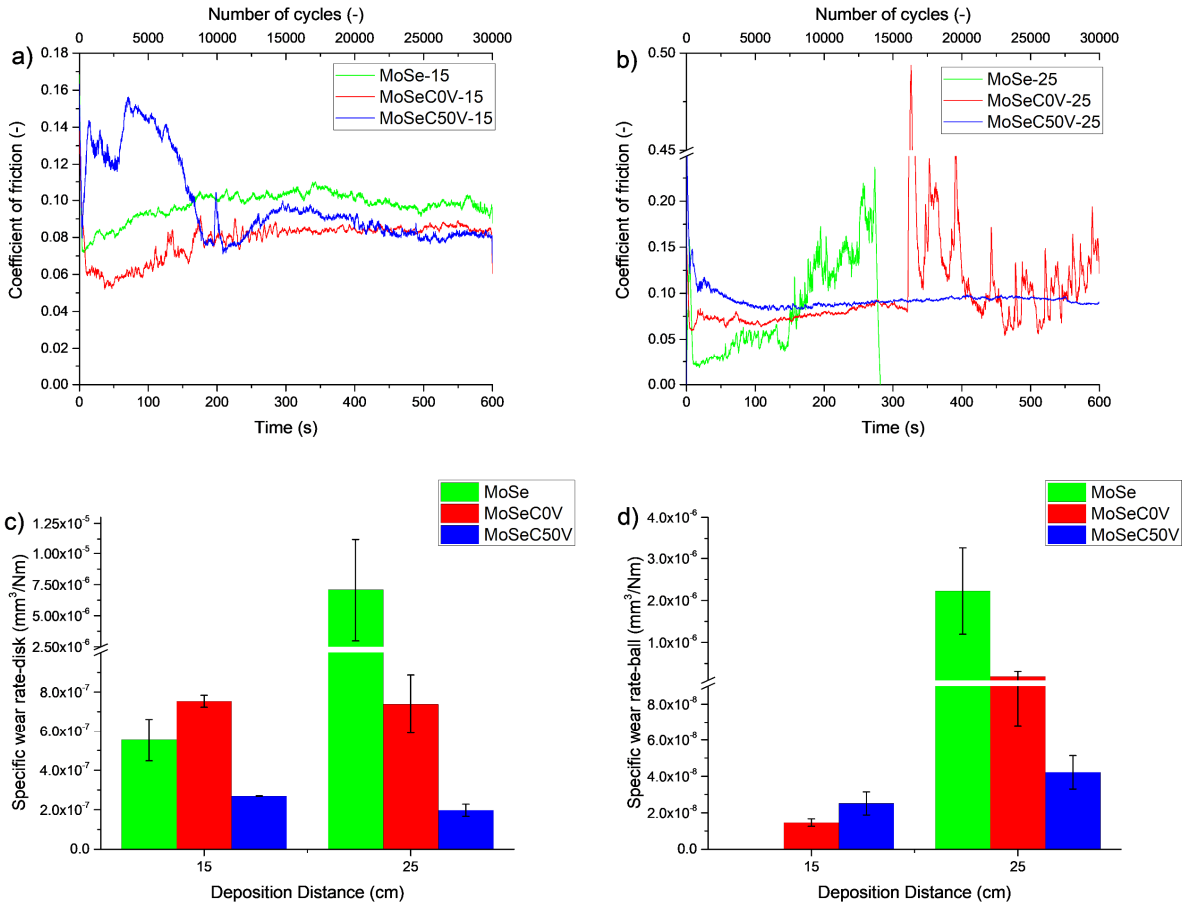

Figure 7-10 Results from the tribological tests at room temperature and ambient air condition a) evolution of the friction coefficient of the coatings deposited at TSD of 15 cm b) evolution of the friction coefficient of the coatings deposited at TSD of 25 cm c)specific wear rate of the coated disk d) specific wear rate of the counterbodies

7.4.2 Tribological behavior in dry N_2 environment

The results from the tribological tests in dry N_2 environments are shown in Figure 7-11. The pure $MoSe_x$ coating deposited at a TSD of 15 cm again outperformed the coating deposited under the same conditions

but a TSD of 25 cm. Moreover, the coating deposited at a TSD of 25 cm failed rather fast (within 10-20 s) with the complete detachment of the $MoSe_x$ coating, leading to the rapid increase in the friction caused by the strong interaction between the Cr interlayer and the bearing steel ball. The COF of the MoSe-15 coating was similar compared to the ambient air testing, although a slight drop to values of ~0.06 occurred before the failure of the coating. It should also be noted that the MoSe-15 coating performed worse under these conditions as failure marked by a continuous increase in friction occurred after ~450 seconds of sliding. This friction increase indicates that the $MoSe_2$ based tribofilm is removed and there is metal-to-metal contact. The worsened behavior during testing in the inert environment can be associated with the potential presence of Cr at the sliding interface. The wear depths measured after both ambient air tests and dry N_2 tests were ~1.7-1.8 μm which reveals that the load support is provided by the Cr interlayer and the gradient $Cr/MoSe_x$ layer and, very probably, there is a presence of Cr in the tribofilms. The increased presence of Cr can have a detrimental effect during sliding against the steel counterbody in inert environments as strong metal-to-metal adhesion can occur [146], followed by the increased wear on both sliding partners. The increased wear can result in the formation of a harder 3rd body wear particles that can easily remove the soft $MoSe_2$ layer, resulting in progressive wear and increase in friction, and, finally, in the complete removal of the lubricious coating. The earlier failure of the MoSe-15 coating during dry N_2 testing is further evident by the increased wear rate compared to the ambient air testing. The carbon alloyed coatings deposited without substrate bias also failed prematurely, with the coating deposited at a TSD of 25 cm lasting longer. The steady-state COF was ~0.06 and ~0.03-0.04 for the MoSeC0V-15 and MoSeC0V-25 coatings, respectively. The specific wear rates were ~4.7 x 10^{-6} mm^3/Nm for and ~9 x 10^{-7} mm^3/Nm for the coatings deposited at a TSD of 15 cm and 25 cm, respectively. Further improvement was observed for the coatings deposited with the application of substrate bias. Initially, the COF was low in both coatings with values of ~0.02-0.03. In the steady-state regime, the COF fluctuated with COF values of ~0.05-0.06. The specific wear rates were low with values of 2.4 x 10^{-7} mm^3/Nm and 3.8 x 10^{-7} mm^3/Nm for the MoSeC50V-15 and MoSeC50V-25 coating, respectively.

Considering the low coefficient of friction achieved in dry N_2 environment, it is very probable that the friction is governed by the $MoSe_2$ phase. The influence of the carbon phase is considered minor as hydrogen-free graphitic carbon phases are unable to provide friction reduction in inert environments, due to the strong adhesion forces with the metallic counterbody [143,145]. The carbon is very likely preferentially removed from the sliding interface [148,168] and its role is towards the hardness improvement, which would provide an improved load-bearing capacity to the coating. These processes would lead to an optimal sliding scenario where the shear strength of the sliding interface is governed by a thin $MoSe_2$ layer while the real contact area is governed by the harder carbon-containing coating.

During sliding in dry N_2 environment, the frictional response of the best performing Mo-Se-C coating is comparable to the one of the W-S-C. A significant difference was observed in terms of wear, where the best performing W-S-C (wear rate of 2-3 x 10^{-8} mm^3/Nm for WSC-4) coating is showing an order of magnitude lower wear rate compared, for example, to the MoSeC50V coating (2-3 x 10^{-7} mm^3/Nm).

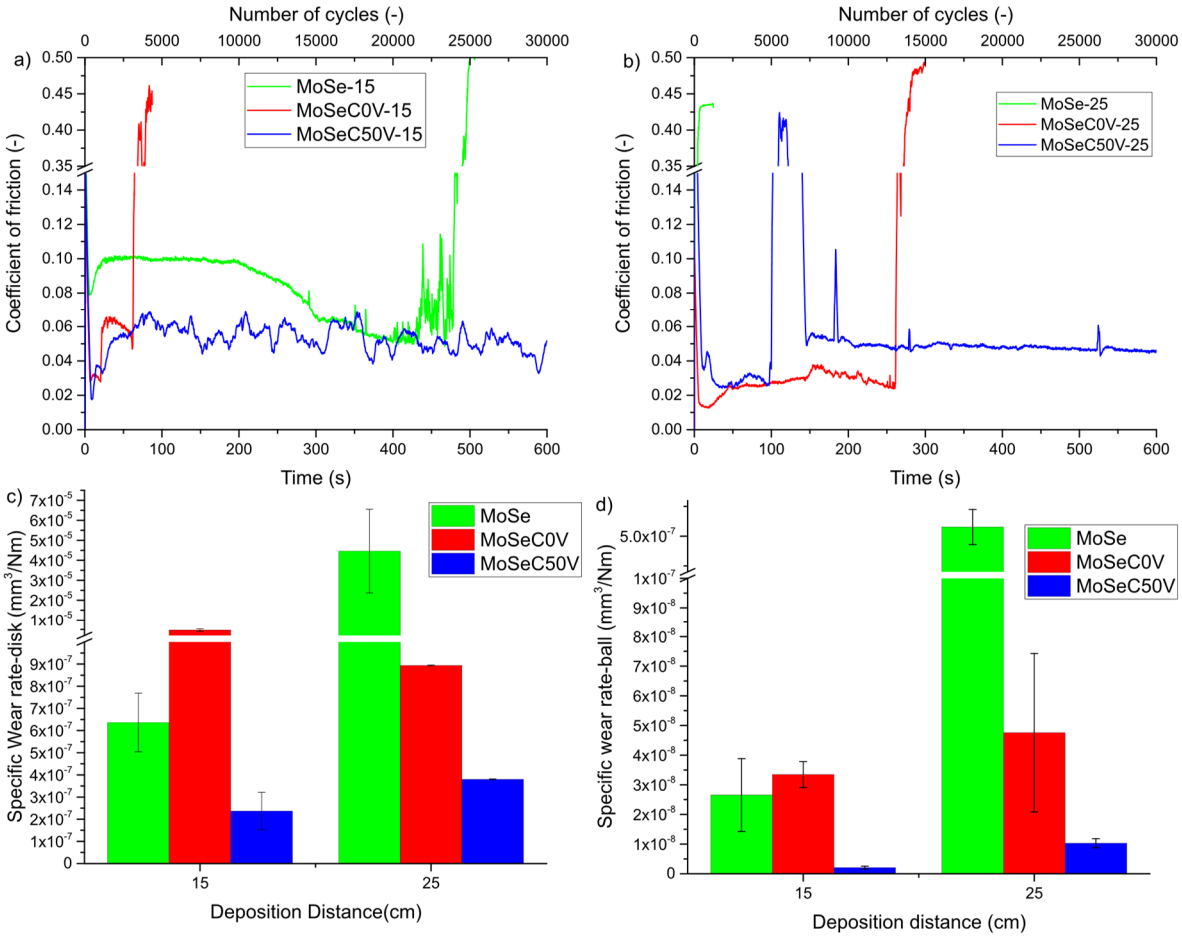

Figure 7-11 Results from the tribological tests performed in dry N_2 environment a) evolution of the friction coefficient of the coatings deposited at TSD of 15 cm b) evolution of the friction coefficient of the coatings deposited at TSD of 25 cm c) specific wear rate of the coated disk d) specific wear rate of the counterbodies

7.4.3 Testing at elevated temperature

The results from the testing at a temperature of 200°C are presented in Figure 7-12. The MoSe-15 coating has a coefficient of friction of ~0.08-0.09 in the steady-state regime. The response was stable until ~550 s of sliding where first a drop in the coefficient of friction was observed (~0.05) followed by a rapid increase with COF values up to 0.3. The coating lasted for 600 s and the wear rate calculated was slightly higher compared to the room temperature test with a value of ~9.5 x 10^{-7} mm^3/Nm. The higher wear is probably a result of accelerated oxidation caused by the elevated temperature [169]. The MoSe-25 coating failed

after ~ 50 s of sliding with a high specific wear rate of ~ 9 x 10^{-6} mm^3/Nm. All the carbon alloyed coatings have a similar coefficient of friction of ~0.04-0.05 with the difference between them being the durability.

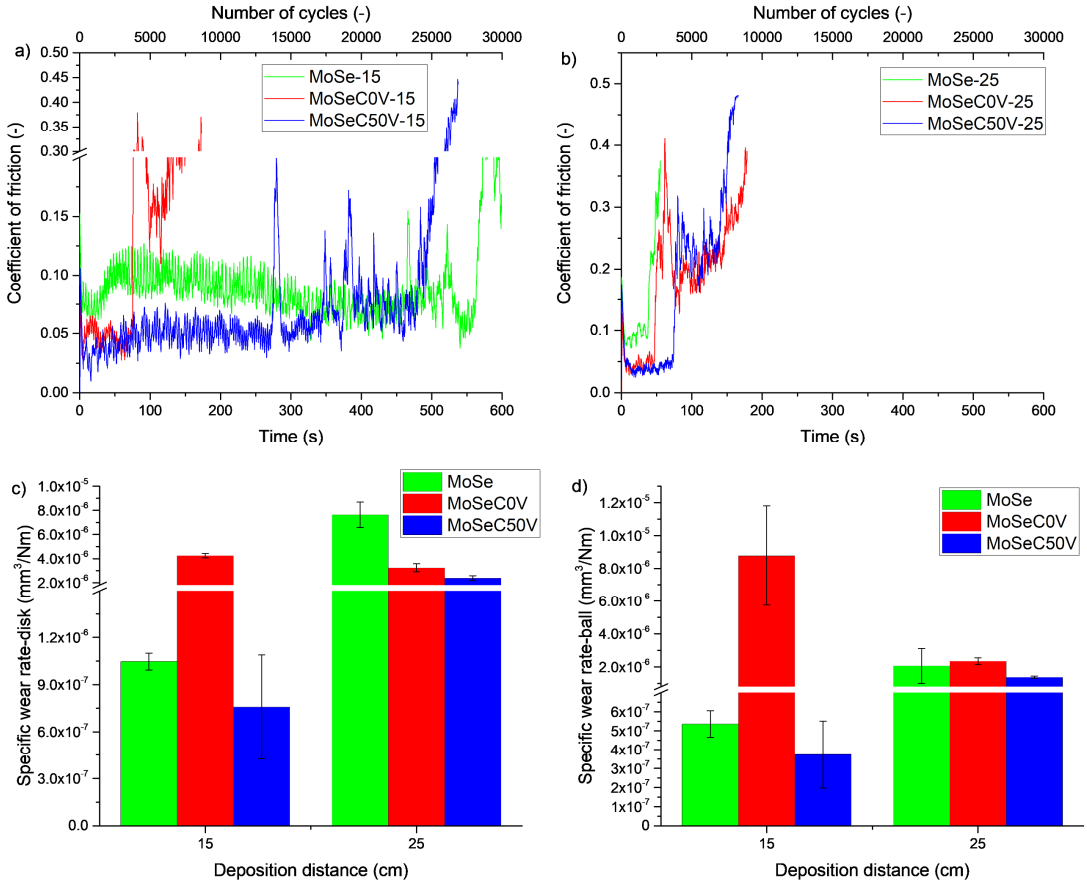

Figure 7-12 Results from the tribological tests performed at 200°C a) evolution of the friction coefficient of the coatings deposited at TSD of 15 cm b) evolution of the friction coefficient of the coatings deposited at TSD of 25 cm c) specific wear rate of the coated disk d) specific wear rate of the counterbodies

The coating MoSeC50V-15 outperformed all the coatings in terms of wear resistance. It should be noted that this coating failed after 500 seconds of sliding, but the volumetric wear loss was lower because the coating had much lower thickness compared to the MoSe-15 coating, which survived the whole duration of the test.

Comparing these results with the ones obtained during sliding in RT condition we can observe a slightly lower coefficient of friction for the carbon alloyed coatings. The lower coefficient of friction can be associated with an accelerated formation of the crystalline $MoSe_2$ tribofilms as a result of the additional input of thermal energy into the contact. Regarding the durability, a significant increase in terms of wear was observed, which can be related to the accelerated oxidation of the $MoSe_2$ phase as well as the increased graphitization of the carbon phase. The hydrogen-free graphitic carbon, although having a layered structure

with low shear strength, is not a good solid lubricant at elevated temperature due to the lack of water vapor that can passivate the surface. Increased wear rate was often observed for hydrogen-free carbon-based coatings at elevated temperatures (see Ref. [144] and the references therein).

Overall, the tribological response was inferior for the optimized MoSeC coatings, compared to the W-S-C ones. The COF was comparable, in the range of 0.02-0.05. The specific wear rate was higher with values of ~ 7 x 10^{-7} mm^3/Nm compared to the typical ~1 x 10^{-7} mm^3/Nm values for the W-S-C coatings. The worsened behavior of MoSeC coatings is in agreement with previous studies on lab-scale deposited Mo-Se-C coatings [168], where the maximum testing temperature without failure was 250°C, which is lower compared to the successful testing of W-S-C even at a temperature of 400°C [142].

7.5 Conclusions

In this Chapter, the deposition of Mo-Se-C coatings was performed by closed-field unbalanced magnetron sputtering. The addition of carbon resulted in the densification of the $MoSe_x$ coatings and hardness improvement. Further optimization was performed by the application of negative substrate bias, resulting in superior nanocomposite coatings. The carbon-containing coatings were X-ray diffraction amorphous, although the additional nanostructure analysis by TEM showed the presence of $MoSe_2$ nanocrystals. The reference pure $MoSe_2$ coatings were soft with hardness below 1 GPa. The Mo-Se-C coatings were significantly harder with values ranging between 4 and 8 GPa, values which were dependent on the compactness of the coatings and the Se/Mo ratio. The adhesion of the coatings could be related to the cross-sectional morphology since the coatings with more compact featureless morphologies showed improved adhesion. This is very likely due to the lack of columnar boundaries affecting the initiation and propagation of the cracks. Finally, the tribological testing demonstrated that the nanocomposite coatings with tailored properties synthesized in a bigger deposition unit can provide low friction and wear, sliding against steel-based material in different environments.

Chapter 8 Conclusions and future work

This chapter summarizes the main conclusions achieved during the work. Furthermore, suggestions for future work and the potential application of the coatings will be discussed.

8.1 Conclusions

The main objective of this work was to upscale the deposition process for carbon alloyed TMD based solid lubricant coatings. The upscaling was performed in several steps, during which various information was extracted related to the relationship between the process parameters and the properties of the resulting coatings.

In terms of an optimal deposition process, sputtering in a non-reactive gas should be the method of choice. The usage of a hydrocarbon gas for the addition of carbon has a disadvantage due to either the poisoning of the TMD targets during deposition or the incorporation of H in the coatings. The poisoning of the targets results in increased target voltages and, thus, the generation of Ar neutrals with high energy which can deteriorate the film properties through the preferential re-sputtering of the lighter chalcogen atoms. Co-sputtering of separate TMD and graphite targets adds flexibility to the process as the target currents and voltages can be adjusted and, thus, the chemical composition can be easily controlled.

Although the compositions studied in the work were limited, the historically used carbon contents of 40-50 at. % showed a promising performance during the semi-industrial synthesis of the coatings. One crucial aspect observed during the study is the ratio between the chalcogen and the transition metal atoms. Based on the Monte-Carlo simulations, this ratio is mostly governed by the bombardment of the growing film with reflected Ar neutrals, with a minor effect of the different scattering behavior of the sputtered species. The optimal ratios were typically 1.5-1.7. On the one hand, lower ratios (e.g. 1.2) gave rise to coatings with increased brittleness which were prone to cracking and delamination. On the other hand, higher ratios of 1.8-2 resulted in coatings with a columnar structure which is inherently porous and prone to intercolumnar cracking, although not to the same extent as the brittle coatings with low ratio.

As mentioned, the ratio between the chalcogen and the transition metal atoms strongly affected the morphological features of the coatings. Higher ratios (e.g. MoSeC0V-15 in Chapter 7 and D2-17 in Chapter 4) resulted in coatings with a pronounced columnar growth due to lower bombardment of the growing film with energetic species and, thus, increased atomic shadowing. The coatings deposited under increased bombardment had a lower ratio (e.g MoSeC50V-15 and WSC-1), and showed denser and compact featureless morphologies.

Generally, the carbon alloyed coatings showed amorphous X-ray diffraction patterns, except for the low carbon content coatings studied in Chapter 4, where WS_2 peaks were detected. Further analysis of the nanostructure through HRTEM often revealed the presence of platelets of TMD embedded in an a-C matrix, even for the W-S-C coating with 50 at. % of carbon and low S/W ratio. The minor differences between the coatings with varying S/W ratio were difficult to depict from the analysis.

The hardness of the coatings was typically in the range of 4-8 GPa. The main properties that affected the hardness were the overall carbon content, the S/W ratio, and the morphology of the coatings. The hardness followed increasing trends with higher carbon content and lower S/W ratios. In this context, the coatings with lower ratios of chalcogen atoms to transition metal atoms are very likely richer in transition metal carbides, although it was difficult to confirm their presence and their content.

The information extracted related to the scratch response and the adhesion of the coatings revealed interesting details. During the semi-industrial synthesis of the coating, the deposition of the interlayer was very similar for all coatings (a Cr interlayer with a gradient Cr/TMD-C layer). This process was well-established for the carbon-based coatings (e.g. W-DLC) often deposited in the same equipment. Besides having a similar interface, some coatings were more prone to cracking, spallation, and delamination. The best results were obtained for the coatings with optimal S,Se/W,Mo ratio and compact featureless morphology (i.e. MoSeC50V-15 in Chapter 7 and WSC-4 in Chapter 6). These coatings were followed by the ones with values very close to the stoichiometry and a columnar structure (e.g MoSeC0V in Chapter 7). The worst scratch response was observed for the coatings with very low ratios, where gross spallation was observed. The bad performance was related to the reduced toughness of the coatings, since, typically, the spallation of the brittle coating was occurring within the top-most TMD-C layer or, at most, the gradient Cr/TMD-C layer. In this context, the main message regarding the adhesion of these coatings is that there is no “single” interface that will ensure good adhesion of the coatings. The toughness of the coating should be carefully considered, along with a fine adjustment of the deposition of the Cr and the gradient layer.

The optimized coatings (MoSeC50V-15 and WSC-4) showed an excellent tribological response during ambient air testing, under dry N_2 environment, and at elevated temperature. The frictional response (COF ~ 0.08) was improved for the $MoSe_2$ based coating compared to the WS_2 one during the ambient air testing, while the wear resistance was quite similar(~ 3 x 10^{-7} mm^3/Nm for both coatings). In a dry N_2 environment the frictional response was very similar for both coatings, with the WS_2 based one showing an improved wear resistance. Finally, the elevated temperature testing revealed an overall better performance for the WS_2 based coating.

In summary, 2 optimal recipes (WSC-4 in Chapter 6 and MoSeC50V-15 in Chapter 7) were achieved for the deposition of self-lubricant carbon alloyed TMD coatings. The recipes are yielding 50% carbon and an X/M ratio of 1.5-1.7. The deposition conditions ensured an optimal bombardment of the growing film with energetic species resulting in a compact featureless morphology, without a significant re-sputtering of the chalcogen atoms and, thus, no hindering of the lubricity. The hardness was ~5 GPa for the WS_2 based coating and ~7 GPa for the $MoSe_2$ based one. It should be noted that the target-to-substrate distance used for the optimal W-S-C coating was longer (25 cm) compared to the Mo-Se-C one (15 cm). In this context,

the Mo-Se-C recipe is more industrially favorable as the standard carousel can be used for the deposition and there is space for fitting more samples.

8.2 Future work

In terms of further development of the PVD deposited coatings studied in the thesis, the influence of the deposition pressure can be studied, particularly for the W-S-C case. The motivation behind this study is the fact that the properties of the coatings were strongly affected by the composition, especially the X/M ratio. Additionally, this ratio was mostly affected by bombardment of the growing film with energetic species which, in the case of W-S-C, were the reflected Ar neutrals. By a fine adjustment of the deposition pressure, the energy of the reflected Ar neutrals can be optimized and, thus, the industrially favorable shorter target-to-substrate distances (15 cm) might be utilized for the deposition. Further studies should be performed on 2-fold rotating parts; minor differences in properties are expected in this case.

The main focus of the future work should be on the applicability of the coatings. The in-lab tribological testing showed very promising performance but the in-service behavior is far from known. Potential applications would be mechanical components operating in diverse environments, ranging from vacuum to humid ambient air conditions and elevated temperatures up to 300-400°C. Typical examples are aerospace components operating in a vacuum that are subjected to relative motion like ball bearings, journal bearings, gears, and other moving assemblies. The good tribological behavior at elevated temperature can further be exploited in manufacturing processes operating at elevated temperatures like injection molding or warm stamping. Finally, the coatings can be exploited in contacts involving aluminium and titanium. A big issue during sliding of, for example, steel against aluminium or titanium is galling, a severe form of wear caused by strong adhesion between the surfaces in contact.

In the context of the application of the coatings on mechanical components, some attempts were already made. Figure 8-1 illustrates the placement of injection moulding components, including ejector pins and the mold itself. These components were coated with a W-S-C coating. Other components on which the W-S-C coating was applied were gears used in aerospace electromechanical actuation systems. The motivation for applying this coating on the gears was the fact that these gears operate in a diverse range of humidities and, thus, the W-S-C were considered good candidate coatings. In order to keep the S/W ratio high, the gears were placed in the middle of the chamber (See Figure 8-2). The placement illustrates the drawback of the currently developed W-S-C coatings in terms of the number of components that can be coated in a single batch.

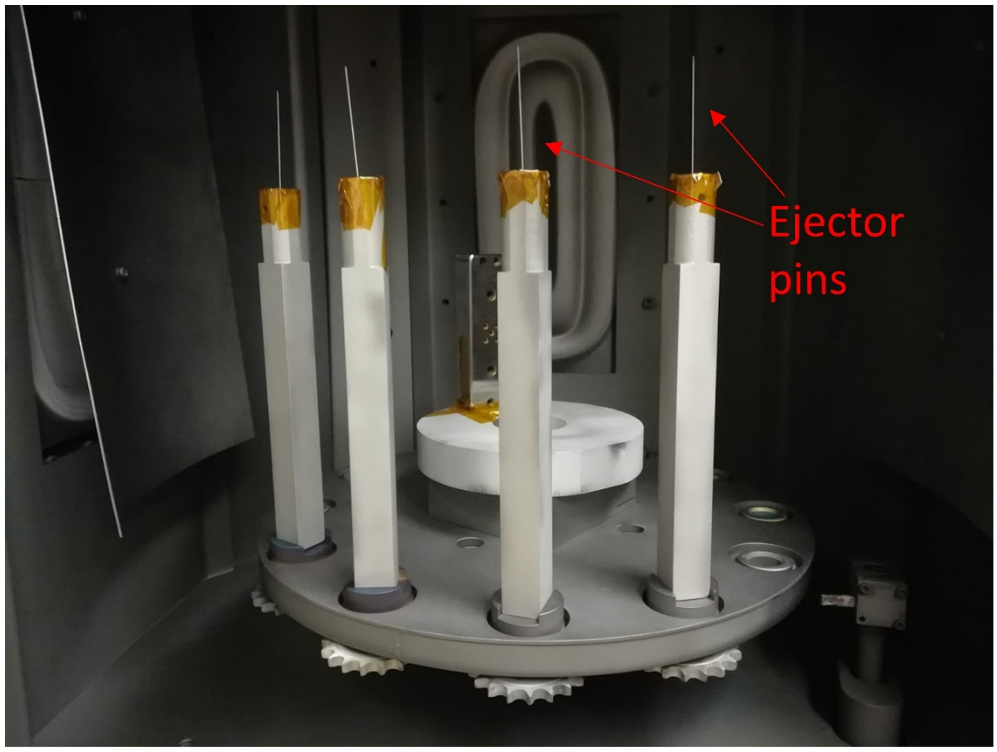

Figure 8-1 Injection moulding components placed in the chamber for coatings

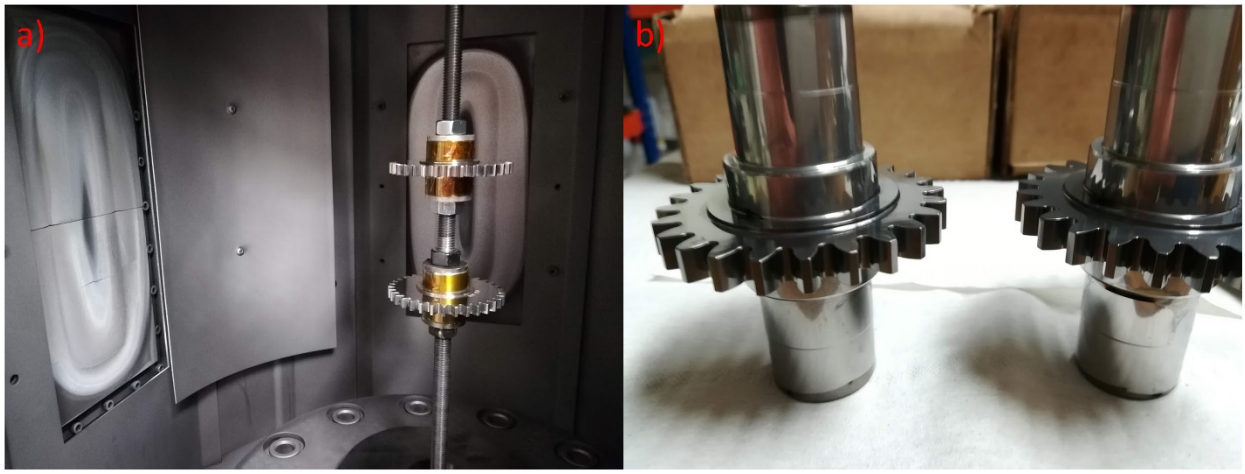

Figure 8-2 a) Placement of gears in the deposition chamber b) gears with the W-S-C coating

References

[1] K. Holmberg, A. Erdemir, Influence of tribology on global energy consumption, costs and emissions, Friction. 5 (2017) 263–284. doi:10.1007/s40544-017-0183-5.

[2] S.K. Biswas, K. Vijayan, Friction and wear of PTFE — a review, Wear. 158 (1992) 193–211. doi:https://doi.org/10.1016/0043-1648(92)90039-B.

[3] B. Panjwani, N. Satyanarayana, S.K. Sinha, Tribological characterization of a biocompatible thin film of UHMWPE on Ti6Al4V and the effects of PFPE as top lubricating layer, J. Mech. Behav. Biomed. Mater. 4 (2011) 953–960. doi:https://doi.org/10.1016/j.jmbbm.2011.02.005.

[4] M. Sedlaček, B. Podgornik, J. Vižintin, Tribological properties of DLC coatings and comparison with test results: Development of a database, Mater. Charact. 59 (2008) 151–161. doi:https://doi.org/10.1016/j.matchar.2006.12.008.

[5] T.W. Scharf, A. Rajendran, R. Banerjee, F. Sequeda, Growth, structure and friction behavior of titanium doped tungsten disulphide (Ti-WS2) nanocomposite thin films, Thin Solid Films. 517 (2009) 5666–5675. doi:https://doi.org/10.1016/j.tsf.2009.02.103.

[6] G. Weise, N. Mattern, H. Hermann, A. Teresiak, I. Bächer, W. Brückner, H.-D. Bauer, H. Vinzelberg, G. Reiss, U. Kreissig, M. Mäder, P. Markschläger, Preparation, structure and properties of MoSx films, Thin Solid Films. 298 (1997) 98–106. doi:https://doi.org/10.1016/S0040-6090(96)09165-1.

[7] M. Kano, Diamond-Like Carbon Coating Applied to Automotive Engine Components, Tribol. Online. 9 (2014) 135–142. doi:10.2474/trol.9.135.

[8] A.A. Voevodin, A.W. Phelps, J.S. Zabinski, M.S. Donley, Friction induced phase transformation of pulsed laser deposited diamond-like carbon, Diam. Relat. Mater. 5 (1996) 1264–1269. doi:10.1016/0925-9635(96)00538-9.

[9] A.A. Voevodin, J.S. Zabinski, Supertough wear-resistant coatings with “chameleon” surface adaptation, Thin Solid Films. 370 (2000) 223–231. doi:10.1016/S0040-6090(00)00917-2.

[10] tribology | Definition of tribology in English by Oxford Dictionaries, (n.d.). https://en.oxforddictionaries.com/definition/tribology (accessed March 17, 2018).

[11] G. Stachowiak, A.W. Batchelor, Engineering tribology, Butterworth-Heinemann, 2013.

[12] T. Mang, K. Bobzin, T. Bartels, Industrial Tribology, Wiley-VCH Verlag GmbH & Co. KGaA, Weinheim, Germany, 2010. doi:10.1002/9783527632572.

[13] E. Popova, V.L. Popov, The research works of Coulomb and Amontons and generalized laws of friction, Friction. 3 (2015) 183–190. doi:10.1007/s40544-015-0074-6.

[14] I.L. Singer, Solid Lubrication Processes, in: Fundam. Frict. Macrosc. Microsc. Process., Springer Netherlands, Dordrecht, 1992: pp. 237–261. doi:10.1007/978-94-011-2811-7_13.

[15] P.J. Blau, Tribosystem analysis : a practical approach to the diagnosis of wear problems, CRC Press, 2017.

[16] G.W. Stachowiak, ed., Wear - Materials, Mechanisms and Practice, John Wiley & Sons Ltd, Chichester, England, 2005. doi:10.1002/9780470017029.

[17] R. Chattopadhyay, Surface wear : analysis, treatment, and prevention, ASM International, 2001.

[18] K. Kato, Chapter 2 Classification of wear mechanisms/ models, in: G. Stachowiak (Ed.), Wear – Mater. Mech. Pract., John Wiley & Sons Ltd, 2005. doi:https://doi.org/10.1002/9780470017029.ch2.

[19] T. BELL, Surface Engineering: a rapidly developing discipline, Eur. J. Eng. Educ. 12 (1987) 27–32. doi:10.1080/03043798708939334.

[20] T. Bell, Surface engineering: its current and future impact on tribology, J. Phys. D. Appl. Phys. 25 (1992) A297–A306. doi:10.1088/0022-3727/25/1A/045.

[21] J. Vetter, G. Barbezat, J. Crummenauer, J. Avissar, Surface treatment selections for automotive applications, Surf. Coatings Technol. 200 (2005) 1962–1968. doi:https://doi.org/10.1016/j.surfcoat.2005.08.011.

[22] C. Mitterer, PVD and CVD Hard Coatings, in: Compr. Hard Mater., Elsevier, 2014: pp. 449–467. doi:10.1016/B978-0-08-096527-7.00035-0.

[23] K.A.H. Al Mahmud, M.A. Kalam, H.H. Masjuki, H.M. Mobarak, N.W.M. Zulkifli, An updated overview of diamond-like carbon coating in tribology, Crit. Rev. Solid State Mater. Sci. 40 (2015) 90–118. doi:10.1080/10408436.2014.940441.

[24] K. (Kenneth) Holmberg, A. (Allan) Matthews, Coatings tribology : properties, mechanisms, techniques and applications in surface engineering, Elsevier Science, 2009.

[25] D.S. Rickerby, A. Matthews, Advanced Surface Coatings: a Handbook of Surface Engineering, Springer Netherlands, 1991.

[26] P.H. Shipway, The range of surface coating methods, in: Surf. Coatings Prot. Against Wear, Elsevier, 2006: pp. 79–100. doi:10.1533/9781845691561.79.

[27] ASM International. Handbook Committee., ASM Handbook: Volume 5: Surface Engineering, 1994.

[28] H. Frey, Cathode Sputtering, in: Handb. Thin-Film Technol., Springer Berlin Heidelberg, Berlin, Heidelberg, 2015: pp. 133–165. doi:10.1007/978-3-642-05430-3_6.

[29] J.E. Greene, Tracing the 5000-year recorded history of inorganic thin films from ∼3000 BC to the early 1900s AD, Appl. Phys. Rev. 1 (2014) 41302. doi:10.1063/1.4902760.

[30] A.R. Lansdown, Lubrication and lubricant selection : a practical guide, ASME Press, 2004.

[31] J.P. Gassiot, On the Stratifications in Electrical Discharges, as Observed in Torricellian and Other Vacua.--Second Communication, Philos. Trans. R. Soc. London. 149 (n.d.) 137–160. doi:10.2307/108693.

[32] A.W. Wright, On a new process for the electrical deposition of metals, and for constructing metal-covered glass specula, J. Franklin Inst. 104 (1877) 242–251. doi:10.1016/0016-0032(77)90348-9.

[33] H.F. Fruth, Cathode sputtering — A commercial application, Bell Syst. Tech. J. 11 (1932) 283–292. doi:10.1002/j.1538-7305.1932.tb03125.x.

[34] W. Crookes, II. On electrical evaporation, Proc. R. Soc. London . 50 (1892) 88–105. doi:10.1098/rspl.1891.0009.

[35] E. Goldstein, XXXVI. On the canal-ray group, London, Edinburgh, Dublin Philos. Mag. J. Sci. 15 (1908) 372–385. doi:10.1080/14786440809463780.

[36] G.K. Wehner, Controlled Sputtering of Metals by Low-Energy Hg Ions, Phys. Rev. 102 (1956) 690–704. doi:10.1103/PhysRev.102.690.

[37] J.J. Thomson, XL. *Cathode Rays*, London, Edinburgh, Dublin Philos. Mag. J. Sci. 44 (1897) 293–316. doi:10.1080/14786449708621070.

[38] Penning Frans Michel, Coating by cathode disintegration, US2146025A, 1936.

[39] J.R. Mullaly, CROSSED-FIELD DISCHARGE DEVICE FOR HIGH RATE SPUTTERING., Dow Chemical Co., Golden, Colo. Rocky Flats Div., 1969.

[40] E. Kay, Magnetic Field Effects on an Abnormal Truncated Glow Discharge and Their Relation to Sputtered Thin-Film Growth, J. Appl. Phys. 34 (1963) 760–768.

[41] J.S. Chapin, Sputtering process and apparatus, US4166018A, 1974.

[42] I. Petrov, F. Adibi, J.E. Greene, W.D. Sproul, W. -D. Münz, Use of an externally applied axial magnetic field to control ion/neutral flux ratios incident at the substrate during magnetron sputter deposition, J. Vac. Sci. Technol. A Vacuum, Surfaces, Film. 10 (1992) 3283–3287. doi:10.1116/1.577812.

[43] P.. Kelly, R.. Arnell, The influence of magnetron configuration on ion current density and deposition rate in a dual unbalanced magnetron sputtering system, Surf. Coatings Technol. 108–109 (1998) 317–322. doi:10.1016/S0257-8972(98)00566-0.

[44] W.D. Sproul, D.J. Christie, D.C. Carter, Control of reactive sputtering processes, Thin Solid Films. 491 (2005) 1–17. doi:10.1016/J.TSF.2005.05.022.

[45] V. Kouznetsov, Method and apparatus for magnetically enhanced sputtering, 1999.

[46] V. Kouznetsov, K. Macák, J.M. Schneider, U. Helmersson, I. Petrov, A novel pulsed magnetron sputter technique utilizing very high target power densities, Surf. Coatings Technol. 122 (1999) 290–293. doi:10.1016/S0257-8972(99)00292-3.

[47] K. Sarakinos, J. Alami, S. Konstantinidis, High power pulsed magnetron sputtering: A review on scientific and engineering state of the art, Surf. Coatings Technol. 204 (2010) 1661–1684. doi:10.1016/J.SURFCOAT.2009.11.013.

[48] A. Anders, A review comparing cathodic arcs and high power impulse magnetron sputtering (HiPIMS), Surf. Coatings Technol. 257 (2014) 308–325. doi:10.1016/J.SURFCOAT.2014.08.043.

[49] K. Bobzin, N. Bagcivan, P. Immich, S. Bolz, J. Alami, R. Cremer, Advantages of nanocomposite coatings deposited by high power pulse magnetron sputtering technology, J. Mater. Process. Technol. 209 (2009) 165–170. doi:10.1016/J.JMATPROTEC.2008.01.035.

[50] J. Alami, P. Eklund, J. Emmerlich, O. Wilhelmsson, U. Jansson, H. Högberg, L. Hultman, U. Helmersson, High-power impulse magnetron sputtering of Ti–Si–C thin films from a Ti3SiC2 compound target, Thin Solid Films. 515 (2006) 1731–1736. doi:10.1016/J.TSF.2006.06.015.

[51] J.E. Mahan, Physical vapor deposition of thin films, Wiley New York, 2000.

[52] D.M. Mattox, Handbook of Physical Vapor Deposition (PVD) Processing, Elsevier Inc., 2007. doi:10.1016/c2009-0-18800-1.

[53] J. Bohdansky, J. Roth, H.L. Bay, An analytical formula and important parameters for low-energy ion sputtering, J. Appl. Phys. 51 (1980) 2861–2865. doi:10.1063/1.327954.

[54] M.W. Thompson, Atomic collision cascades in solids, in: Vacuum, Pergamon, 2002: pp. 99–114. doi:10.1016/S0042-207X(02)00179-3.

[55] R. Behrisch, Introduction and overview BT - Sputtering by Particle Bombardment I: Physical Sputtering of Single-Element Solids, in: R. Behrisch (Ed.), Springer Berlin Heidelberg, 1981: pp. 1–8. doi:10.1007/3540105212_6.

[56] F. Boydens, W.P. Leroy, R. Persoons, D. Depla, The influence of target surface morphology on the deposition flux during direct-current magnetron sputtering, Thin Solid Films. 531 (2013) 32–41. doi:10.1016/j.tsf.2012.11.097.

[57] S. Prasad, J. Zabinski, Super slippery solids, Nature. 387 (1997) 761. doi:10.1038/42820.

[58] A.R. Lansdown, Lubrication and lubricant selection : a practical guide, ASME Press, 2004.

[59] A.I. Brudnyi, A.F. Karmadonov, Structure of molybdenum disulphide lubricant film, Wear. 33 (1975) 243–249. doi:10.1016/0043-1648(75)90279-3.

[60] R.L. Fusaro, Lubrication and failure mechanisms of molybdenum disulfide films, National Aeronautics and Space Administration, Scientific and Technical …, 1978.

[61] W.J. Bartz, X. Jinfen, Wear behaviour and failure mechanism of bonded solid lubricants, Wear. 150 (1991) 231–246. doi:10.1016/0043-1648(91)90319-P.

[62] T. Spalvins, Lubrication with Sputtered MoS_2 Films, A S L E Trans. 14 (1971) 267–274. doi:10.1080/05698197108983252.

[63] T. Spalvins, Lubrication with sputtered MoS 2 films: principles, operation, and limitations, J. Mater.

Eng. Perform. 1 (1992) 347–351.

[64] B.C. Stupp, Synergistic effects of metals co-sputtered with MoS2, Thin Solid Films. 84 (1981) 257–266. doi:10.1016/0040-6090(81)90023-7.

[65] J.L. Grosseau-Poussard, P. Moine, J.P. Villain, Microstructural and tribological characterization of MoSx coatings produced by high-energy ion-beam-assisted deposition, Thin Solid Films. 224 (1993) 52–57. doi:10.1016/0040-6090(93)90457-Z.

[66] S. V. Prasad, J.S. Zabinski, Tribology of tungsten disulphide (WS2): characterization of wear-induced transfer films, J. Mater. Sci. Lett. 12 (1993) 1413–1415. doi:10.1007/BF00591592.

[67] J.R. Lince, M.R. Hilton, A.S. Bommannavar, Oxygen substitution in sputter-deposited MoS2 films studied by extended X-ray absorption fine structure, X-ray photoelectron spectroscopy and X-ray diffraction, Surf. Coatings Technol. 43–44 (1990) 640–651. doi:10.1016/0257-8972(90)90008-Z.

[68] L. Huiwen, Z. Xushou, Y. Deyang, W. Xiaoping, The enhancement of wear life and moisture resistance of sputtered MoS2 films by metal ion implantation, Wear. 173 (1994) 145–149. doi:10.1016/0043-1648(94)90267-4.

[69] M.R. Hilton, R. Bauer, S. V. Didziulis, M.T. Dugger, J.M. Keem, J. Scholhamer, Structural and tribological studies of MoS2 solid lubricant films having tailored metal-multilayer nanostructures, Surf. Coatings Technol. 53 (1992) 13–23. doi:10.1016/0257-8972(92)90099-V.

[70] S.D. Walck, J.S. Zabinski, N.T. McDevitt, J.E. Bultman, Characterization of air-annealed, pulsed laser deposited ZnO-WS2 solid film lubricants by transmission electron microscopy, Thin Solid Films. 305 (1997) 130–143. doi:10.1016/S0040-6090(97)00129-6.

[71] G. Weise, A. Teresiak, I. Bächer, P. Markschläger, G. Kampschulte, Influence of magnetron sputtering process parameters on wear properties of steel/Cr3Si or Cr/MoSx, Surf. Coatings Technol. 76–77 (1995) 382–392. doi:10.1016/0257-8972(95)02605-3.

[72] D.-Y. Yu, J.-A. Wang, J.-L.O. Yang, Variations of properties of the MoS2-LaF3 cosputtered and MoS2-sputtered films after storage in moist air, Thin Solid Films. 293 (1997) 1–5. doi:10.1016/S0040-6090(96)08959-6.

[73] X. Zhang, R.G. Vitchev, W. Lauwerens, L. Stals, J. He, J.-P. Celis, Effect of crystallographic orientation on fretting wear behaviour of MoSx coatings in dry and humid air, Thin Solid Films. 396 (2001) 69–

77. doi:https://doi.org/10.1016/S0040-6090(01)01141-5.

[74] T. Kubart, T. Polcar, L. Kopecký, R. Novák, D. Nováková, Temperature dependence of tribological properties of MoS2 and MoSe2 coatings, Surf. Coatings Technol. 193 (2005) 230–233. doi:10.1016/J.SURFCOAT.2004.08.146.

[75] D.G. Teer, J. Hampshire, V. Fox, V. Bellido-Gonzalez, The tribological properties of MoS2/metal composite coatings deposited by closed field magnetron sputtering, Surf. Coatings Technol. 94–95 (1997) 572–577. doi:https://doi.org/10.1016/S0257-8972(97)00498-2.

[76] V.C. Fox, N. Renevier, D.G. Teer, J. Hampshire, V. Rigato, The structure of tribologically improved MoS2–metal composite coatings and their industrial applications, Surf. Coatings Technol. 116–119 (1999) 492–497. doi:https://doi.org/10.1016/S0257-8972(99)00193-0.

[77] S. Mikhailov, A. Savan, E. Pflüger, L. Knoblauch, R. Hauert, M. Simmonds, H. Van Swygenhoven, Morphology and tribological properties of metal (oxide)–MoS2 nanostructured multilayer coatings, Surf. Coatings Technol. 105 (1998) 175–183. doi:https://doi.org/10.1016/S0257-8972(98)00483-6.

[78] J. Rech, A. Kusiak, J.L. Battaglia, Tribological and thermal functions of cutting tool coatings, Surf. Coatings Technol. 186 (2004) 364–371. doi:https://doi.org/10.1016/j.surfcoat.2003.11.027.

[79] A.A. Voevodin, J.P. O'Neill, J.S. Zabinski, Nanocomposite tribological coatings for aerospace applications, Surf. Coatings Technol. 116–119 (1999) 36–45. doi:10.1016/S0257-8972(99)00228-5.

[80] A.A. Voevodin, T.A. Fitz, J.J. Hu, J.S. Zabinski, Nanocomposite tribological coatings with "chameleon" surface adaptation, J. Vac. Sci. Technol. A Vacuum, Surfaces, Film. 20 (2002) 1434–1444. doi:10.1116/1.1487875.

[81] A. Nossa, A. Cavaleiro, The influence of the addition of C and N on the wear behaviour of W–S–C/N coatings, Surf. Coatings Technol. 142–144 (2001) 984–991. doi:10.1016/S0257-8972(01)01249-X.

[82] A. Nossa, A. Cavaleiro, Mechanical behaviour of W–S–N and W–S–C sputtered coatings deposited with a Ti interlayer, Surf. Coatings Technol. 163–164 (2003) 552–560. doi:10.1016/S0257-8972(02)00622-9.

[83] A. Nossa, A. Cavaleiro, Chemical and physical characterization of C(N)-doped W–S sputtered films, J. Mater. Res. 19 (2004) 2356–2365. doi:10.1557/JMR.2004.0293.

[84] A. Nossa, A. Cavaleiro, N.J.M. Carvalho, B.J. Kooi, J.T.M. De Hosson, On the microstructure of tungsten disulfide films alloyed with carbon and nitrogen, Thin Solid Films. 484 (2005) 389–395. doi:10.1016/j.tsf.2005.02.018.

[85] M. Evaristo, A. Nossa, A. Cavaleiro, W–S–C sputtered films: Influence of the carbon alloying method on the mechanical properties, Surf. Coatings Technol. 200 (2005) 1076–1079. doi:10.1016/J.SURFCOAT.2005.02.039.

[86] T. Polcar, M. Evaristo, A. Cavaleiro, Friction of Self-Lubricating W-S-C Sputtered Coatings Sliding Under Increasing Load, Plasma Process. Polym. 4 (2007) S541–S546. doi:10.1002/ppap.200731402.

[87] T. Polcar, M. Evaristo, M. Stueber, A. Cavaleiro, Synthesis and structural properties of Mo–Se–C sputtered coatings, Surf. Coatings Technol. 202 (2008) 2418–2422. doi:10.1016/J.SURFCOAT.2007.08.019.

[88] C.S. Sandu, T. Polcar, A. Cavaleiro, TEM investigation of MoSeC films, Microsc. Microanal. 14 (2008) 7–10. doi:10.1017/S1431927608089228.

[89] T. Polcar, M. Evaristo, M. Stueber, A. Cavaleiro, Mechanical and tribological properties of sputtered Mo-Se-C coatings, Wear. 266 (2009) 393–397. doi:10.1016/j.wear.2008.04.010.

[90] T. Polcar, M. Evaristo, R. Colaço, C. Silviu Sandu, A. Cavaleiro, Nanoscale triboactivity: The response of Mo–Se–C coatings to sliding, Acta Mater. 56 (2008) 5101–5111. doi:10.1016/J.ACTAMAT.2008.06.029.

[91] F. Gustavsson, S. Jacobson, A. Cavaleiro, T. Polcar, Frictional behavior of self-adaptive nanostructural Mo–Se–C coatings in different sliding conditions, Wear. 303 (2013) 286–296. doi:10.1016/J.WEAR.2013.03.032.

[92] M. Evaristo, T. Polcar, A. Cavaleiro, Synthesis and properties of W–Se–C coatings deposited by PVD in reactive and non-reactive processes, Vacuum. 83 (2009) 1262–1265. doi:10.1016/J.VACUUM.2009.03.030.

[93] M. Evaristo, T. Polcar, A. Cavaleiro, Can W□Se□C Coatings Be Competitive to W□S□C Ones?, Plasma Process. Polym. 6 (2009) S92–S95. doi:10.1002/ppap.200930414.

[94] V.Y. Fominski, S.N. Grigoriev, J.P. Celis, R.I. Romanov, V.B. Oshurko, Structure and mechanical properties of W–Se–C/diamond-like carbon and W–Se/diamond-like carbon bi-layer coatings

prepared by pulsed laser deposition, Thin Solid Films. 520 (2012) 6476–6483. doi:10.1016/j.tsf.2012.06.085.

[95] S.N. Grigoriev, V.Y. Fominskii, R.I. Romanov, V.N. Nevolin, Tribological and mechanical properties of nanostructured solid lubricant W-Se-C coatings produced by laser deposition, Inorg. Mater. Appl. Res. 3 (2012) 347–355. doi:10.1134/S207511331205005X.

[96] S. Dominguez-Meister, A. Justo, J.C. Sanchez-Lopez, Synthesis and tribological properties of WSex films prepared by magnetron sputtering, Mater. Chem. Phys. 142 (2013) 186–194. doi:10.1016/J.MATCHEMPHYS.2013.07.004.

[97] S. Domínguez-Meister, M. Conte, A. Igartua, T.C. Rojas, J.C. Sánchez-López, Self-Lubricity of WSe_x Nanocomposite Coatings, ACS Appl. Mater. Interfaces. 7 (2015) 7979–7986. doi:10.1021/am508939s.

[98] H. Cao, J.T.M. De Hosson, Y. Pei, Effect of carbon concentration and argon flow rate on the microstructure and triboperformance of magnetron sputtered WS2/a-C coatings, Surf. Coatings Technol. 332 (2017) 142–152. doi:10.1016/J.SURFCOAT.2017.06.087.

[99] H. Cao, F. Wen, S. Kumar, P. Rudolf, J.T.M. De Hosson, Y. Pei, On the S/W stoichiometry and triboperformance of WSxC(H) coatings deposited by magnetron sputtering, Surf. Coatings Technol. (2018). doi:10.1016/J.SURFCOAT.2018.04.040.

[100] D.G. Teer, EP0521045B1 - Magnetron sputter ion plating, 1997.

[101] J.F. Ziegler, M.D. Ziegler, J.P. Biersack, SRIM – The stopping and range of ions in matter (2010), Nucl. Instruments Methods Phys. Res. Sect. B Beam Interact. with Mater. Atoms. 268 (2010) 1818–1823. doi:10.1016/J.NIMB.2010.02.091.

[102] K. Van Aeken, S. Mahieu, D. Depla, The metal flux from a rotating cylindrical magnetron: A Monte Carlo simulation, J. Phys. D. Appl. Phys. 41 (2008). doi:10.1088/0022-3727/41/20/205307.

[103] D. Nečas, P. Klapetek, Gwyddion: An open-source software for SPM data analysis, Cent. Eur. J. Phys. 10 (2012) 181–188. doi:10.2478/s11534-011-0096-2.

[104] A.C. Ferrari, J. Robertson, Interpretation of Raman spectra of disordered and amorphous carbon, Phys. Rev. B. 61 (2000) 14095–14107. doi:10.1103/PhysRevB.61.14095.

[105] W.C. Oliver, G.M. Pharr, An improved technique for determining hardness and elastic modulus

using load and displacement sensing indentation experiments, J. Mater. Res. 7 (1992) 1564–1583. doi:10.1557/JMR.1992.1564.

[106] ISO - ISO 20502:2005 - Fine ceramics (advanced ceramics, advanced technical ceramics) — Determination of adhesion of ceramic coatings by scratch testing, (n.d.).

[107] N. Vidakis, A. Antoniadis, N. Bilalis, The VDI 3198 indentation test evaluation of a reliable qualitative control for layered compounds, in: J. Mater. Process. Technol., 2003: pp. 481–485. doi:10.1016/S0924-0136(03)00300-5.

[108] ISO 19291:2016(en), Lubricants — Determination of tribological quantities for oils and greases — Tribological test in the translatory oscillation apparatus, n.d.

[109] J.A. Williams, Wear modelling: Analytical, computational and mapping: A continuum mechanics approach, Wear. 225–229 (1999) 1–17. doi:10.1016/S0043-1648(99)00060-5.

[110] E. Särhammar, E. Strandberg, J. Sundberg, H. Nyberg, T. Kubart, S. Jacobson, U. Jansson, T. Nyberg, Mechanisms for compositional variations of coatings sputtered from a WS2 target, Surf. Coatings Technol. 252 (2014) 186–190. doi:10.1016/j.surfcoat.2014.04.066.

[111] A. Nossa, A. Cavaleiro, Mechanical behaviour of W-S-N and W-S-C sputtered coatings deposited with a Ti interlayer, Surf. Coatings Technol. 163–164 (2003) 552–560. doi:10.1016/S0257-8972(02)00622-9.

[112] I. Petrov, P.B. Barna, L. Hultman, J.E. Greene, Microstructural evolution during film growth, J. Vac. Sci. Technol. A Vacuum, Surfaces, Film. 21 (2003) S117–S128. doi:10.1116/1.1601610.

[113] G. Weise, N. Mattern, H. Hermann, A. Teresiak, I. Ba, W. Bru, Preparation , structure and properties of MoS x films, 298 (1997) 98–106.

[114] A.A. Voevodin, J.P. O'Neill, S. V. Prasad, J.S. Zabinski, Nanocrystalline WC and WC/a-C composite coatings produced from intersected plasma fluxes at low deposition temperatures, J. Vac. Sci. Technol. A Vacuum, Surfaces, Film. 17 (1999) 986–992. doi:10.1116/1.581674.

[115] M.D. Abad, M.A. Muñoz-Márquez, S. El Mrabet, A. Justo, J.C. Sánchez-López, Tailored synthesis of nanostructured WC/a-C coatings by dual magnetron sputtering, Surf. Coatings Technol. 204 (2010) 3490–3500. doi:10.1016/J.SURFCOAT.2010.04.019.

[116] P. V. Krasovskii, O.S. Malinovskaya, A. V. Samokhin, Y. V. Blagoveshchenskiy, V.A. Kazakov, A.A.

Ashmarin, XPS study of surface chemistry of tungsten carbides nanopowders produced through DC thermal plasma/hydrogen annealing process, Appl. Surf. Sci. 339 (2015) 46–54. doi:10.1016/J.APSUSC.2015.02.152.

[117] A.A. Voevodin, J.P.O. Neill, S. V Prasad, J.S. Zabinski, A.A. Voevodin, J.P.O. Neill, S. V Prasad, J.S. Zabinski, Nanocrystalline WC and WC / a -C composite coatings produced from intersected plasma fluxes at low deposition temperatures, 986 (2008). doi:10.1116/1.581674.

[118] A. Nossa, A. Cavaleiro, Chemical and physical characterization of C(N)-doped W-S sputtered films, J. Mater. Res. 19 (2004) 2356–2365. doi:10.1557/JMR.2004.0293.

[119] J.F. Moulder, J. Chastain, Handbook of x-ray photoelectron spectroscopy : a reference book of standard spectra for identification and interpretation of XPS data, Physical Electronics Division, Perkin-Elmer Corp, 1992.

[120] D.J. Morgan, Core-level spectra of powdered tungsten disulfide, WS_2, Surf. Sci. Spectra. 25 (2018) 14002. doi:10.1116/1.5030093.

[121] I. Martin-Litas, P. Vinatier, A. Levasseur, J.. Dupin, D. Gonbeau, F. Weill, Characterisation of r.f. sputtered tungsten disulfide and oxysulfide thin films, Thin Solid Films. 416 (2002) 1–9. doi:10.1016/S0040-6090(02)00717-4.

[122] J.-C. Dupin, D. Gonbeau, P. Vinatier, A. Levasseur, Systematic XPS studies of metal oxides, hydroxides and peroxides, Phys. Chem. Chem. Phys. 2 (2000) 1319–1324. doi:10.1039/a908800h.

[123] J.. Bernède, About the preferential sputtering of chalcogen from transition metal dichalcogenide compounds and the determination of compound stoichiometry from XPS peak positions, Appl. Surf. Sci. 171 (2001) 15–20. doi:10.1016/S0169-4332(00)00535-3.

[124] S. Doniach, M. Sunjic, Many-electron singularity in X-ray photoemission and X-ray line spectra from metals, J. Phys. C Solid State Phys. 3 (1970) 285–291. doi:10.1088/0022-3719/3/2/010.

[125] S. Hüfner, Continuous Satellites and Plasmon Satellites: XPS Photoemission in Nearly Free Electron Systems, in: Springer, Berlin, Heidelberg, 2003: pp. 173–209. doi:10.1007/978-3-662-09280-4_4.

[126] N.J. Shevchik, PHYSICAL REVIEW LETTERS Local Density of States and Core-Hole Conduction-Electron Interactions in the X-Ray Photoemission Spectra of Pt and Ni, 1974. https://journals.aps.org/prl/pdf/10.1103/PhysRevLett.33.1336 (accessed January 25, 2019).

[127] A. Berkdemir, H.R. Gutiérrez, A.R. Botello-Méndez, N. Perea-López, A.L. Elías, C.-I. Chia, B. Wang, V.H. Crespi, F. López-Urías, J.-C. Charlier, H. Terrones, M. Terrones, Identification of individual and few layers of WS2 using Raman Spectroscopy, Sci. Rep. 3 (2013) 1755. doi:10.1038/srep01755.

[128] C. Donnet, A. Erdemir, Diamond-like carbon films: A historical overview, in: Tribol. Diamond-Like Carbon Film. Fundam. Appl., Springer US, 2008. doi:10.1007/978-0-387-49891-1.

[129] C.W. Moura e Silva, J.R.T. Branco, A. Cavaleiro, How can H content influence the tribological behaviour of W-containing DLC coatings, Solid State Sci. 11 (2009) 1778–1782. doi:10.1016/j.solidstatesciences.2009.01.001.

[130] J. Stallard, S. Poulat, D.G. Teer, The study of the adhesion of a TiN coating on steel and titanium alloy substrates using a multi-mode scratch tester, Tribol. Int. 39 (2006) 159–166. doi:10.1016/J.TRIBOINT.2005.04.011.

[131] L.E. Rumaner, T. Tazawa, F.S. Ohuchi, Compositional change of (0001) WS_2 surfaces induced by ion beam bombardment with energies between 100 and 1500 eV, J. Vac. Sci. Technol. A Vacuum, Surfaces, Film. 12 (1994) 2451–2456. doi:10.1116/1.579192.

[132] T. Polcar, A. Cavaleiro, Review on self-lubricant transition metal dichalcogenide nanocomposite coatings alloyed with carbon, Surf. Coatings Technol. 206 (2011) 686–695. doi:10.1016/J.SURFCOAT.2011.03.004.

[133] M. Evaristo, R. Azevedo, C. Palacio, A. Cavaleiro, Influence of the silicon and oxygen content on the properties of non-hydrogenated amorphous carbon coatings, Diam. Relat. Mater. 70 (2016) 201–210. doi:10.1016/J.DIAMOND.2016.10.024.

[134] T. Polcar, M. Evaristo, A. Cavaleiro, The tribological behavior of W–S–C films in pin-on-disk testing at elevated temperature, Vacuum. 81 (2007) 1439–1442. doi:10.1016/J.VACUUM.2007.04.010.

[135] A. Leyland, A. Matthews, On the significance of the H/E ratio in wear control: a nanocomposite coating approach to optimised tribological behaviour, Wear. 246 (2000) 1–11. doi:10.1016/S0043-1648(00)00488-9.

[136] J. Musil, F. Kunc, H. Zeman, H. Poláková, Relationships between hardness, Young's modulus and elastic recovery in hard nanocomposite coatings, Surf. Coatings Technol. 154 (2002) 304–313. doi:10.1016/S0257-8972(01)01714-5.

[137] K.J. Wahl, L.E. Seitzman, R.N. Bolster, I.L. Singer, Low-friction, high-endurance, ion-beam-deposited PbMoS coatings, Surf. Coatings Technol. 73 (1995) 152–159. doi:10.1016/0257-8972(94)02383-2.

[138] J.S. Zabinski, M.S. Donley, V.J. Dyhouse, N.T. McDevitt, Chemical and tribological characterization of PbOMoS2 films grown by pulsed laser deposition, Thin Solid Films. 214 (1992) 156–163. doi:10.1016/0040-6090(92)90764-3.

[139] A.K. Kohli, B. Prakash, Contact pressure dependency in frictional behavior of burnished molybdenum disulphide coatings, Tribol. Trans. 44 (2001) 147–151. doi:10.1080/10402000108982439.

[140] I.L. Singer, R.N. Bolster, J. Wegand, S. Fayeulle, B.C. Stupp, Hertzian stress contribution to low friction behavior of thin MoS 2 coatings, Appl. Phys. Lett. 57 (1990) 995–997. doi:10.1063/1.104276.

[141] P. Nicolini, R. Capozza, P. Restuccia, T. Polcar, Structural Ordering of Molybdenum Disulfide Studied via Reactive Molecular Dynamics Simulations, ACS Appl. Mater. Interfaces. 10 (2018) 8937–8946. doi:10.1021/acsami.7b17960.

[142] T. Polcar, M. Evaristo, A. Cavaleiro, The tribological behavior of W–S–C films in pin-on-disk testing at elevated temperature, Vacuum. 81 (2007) 1439–1442. doi:10.1016/J.VACUUM.2007.04.010.

[143] T. Krumpiegl, H. Meerkamm, W. Fruth, C. Schaufler, G. Erkens, H. Böhner, Amorphous carbon coatings and their tribological behaviour at high temperatures and in high vacuum, in: Surf. Coatings Technol., 1999: pp. 555–560. doi:10.1016/S0257-8972(99)00435-1.

[144] E. Konca, Y.T. Cheng, A.M. Weiner, J.M. Dasch, A.T. Alpas, Elevated temperature tribological behavior of non-hydrogenated diamond-like carbon coatings against 319 aluminum alloy, Surf. Coatings Technol. 200 (2006) 3996–4005. doi:10.1016/j.surfcoat.2005.02.202.

[145] J. Andersson, R.A. Erck, A. Erdemir, Friction of diamond-like carbon films in different atmospheres, Wear. 254 (2003) 1070–1075. doi:10.1016/S0043-1648(03)00336-3.

[146] K. Miyoshi, Considerations in vacuum tribology (adhesion, friction, wear, and solid lubrication in vacuum), Tribol. Int. 32 (1999) 605–616. doi:10.1016/S0301-679X(99)00093-6.

[147] G. Colas, A. Saulot, E. Regis, Y. Berthier, Investigation of crystalline and amorphous MoS2 based coatings: Towards developing new coatings for space applications, Wear. 330–331 (2015) 448–

460. doi:10.1016/j.wear.2015.01.011.

[148] F. Gustavsson, S. Jacobson, A. Cavaleiro, T. Polcar, Frictional behavior of self-adaptive nanostructural Mo-Se-C coatings in different sliding conditions, Wear. 303 (2013) 286–296. doi:10.1016/j.wear.2013.03.032.

[149] J. Sundberg, H. Nyberg, E. Särhammar, F. Gustavsson, T. Kubart, T. Nyberg, S. Jacobson, U. Jansson, Influence of Ti addition on the structure and properties of low-friction W–S–C coatings, Surf. Coatings Technol. 232 (2013) 340–348. doi:10.1016/J.SURFCOAT.2013.05.032.

[150] T. Polcar, F. Gustavsson, T. Thersleff, S. Jacobson, A. Cavaleiro, Complex frictional analysis of self-lubricant W-S-C/Cr coating, Faraday Discuss. 156 (2012) 383. doi:10.1039/c2fd00003b.

[151] Y. Kurahashi, H. Tanaka, M. Terayama, J. Sugimura, Effects of Environmental Gas and Trace Water on the Friction of DLC Sliding with Metals, Micromachines. 8 (2017) 217. doi:10.3390/mi8070217.

[152] G. Colas, A. Saulot, N. Bouscharain, C. Godeau, Y. Michel, Y. Berthier, How far does contamination help dry lubrication efficiency?, Tribol. Int. 65 (2013) 177–189. doi:10.1016/J.TRIBOINT.2012.12.011.

[153] M.N. Gardos, Anomalous wear behavior of MoS2 films in moderate vacuum and dry nitrogen, Tribol. Lett. 1 (1995) 67–85. doi:10.1007/BF00157977.

[154] W. Tillmann, N.F. Lopes Dias, D. Stangier, W. Maus-Friedrichs, R. Gustus, C.A. Thomann, H. Moldenhauer, J. Debus, Improved adhesion of a-C and a-C:H films with a CrC interlayer on 16MnCr5 by HiPIMS-pretreatment, Surf. Coatings Technol. 375 (2019) 877–887. doi:10.1016/j.surfcoat.2019.07.076.

[155] J. Schaufler, G. Yang, K. Durst, E. Spiecker, M. Göken, Microscopic study on the interfacial strength of hydrogenated amorphous carbon coating systems, Surf. Coatings Technol. 205 (2011) 3429–3433. doi:10.1016/j.surfcoat.2010.12.005.

[156] R. Jacobs, J. Meneve, G. Dyson, D.G. Teer, N.M. Jennett, P. Harris, J. von Stebut, C. Comte, P. Feuchter, A. Cavaleiro, H. Ronkainen, K. Holmberg, U. Beck, G. Reiners, C.D. Ingelbrecht, A certified reference material for the scratch test, Surf. Coatings Technol. 174–175 (2003) 1008–1013. doi:10.1016/S0257-8972(03)00470-5.

[157] D.L.A. de Faria, S. Venâncio Silva, M.T. de Oliveira, Raman microspectroscopy of some iron oxides

and oxyhydroxides, J. Raman Spectrosc. 28 (1997) 873–878. doi:10.1002/(SICI)1097-4555(199711)28:11<873::AID-JRS177>3.0.CO;2-B.

[158] M.F. Daniel, B. Desbat, J.C. Lassegues, B. Gerand, M. Figlarz, Infrared and Raman study of WO3 tungsten trioxides and WO3, xH2O tungsten trioxide tydrates, J. Solid State Chem. 67 (1987) 235–247. doi:10.1016/0022-4596(87)90359-8.

[159] T.W. Scharf, S. V Prasad, Solid lubricants: a review, J. Mater. Sci. 48 (2013) 511–531.

[160] A. Anders, A structure zone diagram including plasma-based deposition and ion etching, Thin Solid Films. 518 (2010) 4087–4090. doi:10.1016/j.tsf.2009.10.145.

[161] C. Muratore, A.A. Voevodin, Control of molybdenum disulfide basal plane orientation during coating growth in pulsed magnetron sputtering discharges, Thin Solid Films. 517 (2009) 5605–5610. doi:10.1016/j.tsf.2009.01.190.

[162] M. Regula, C. Ballif, J.H. Moser, F. Lévy, Structural, chemical, and electrical characterisation of reactively sputtered WSx thin films, Thin Solid Films. 280 (1996) 67–75. doi:10.1016/0040-6090(95)08206-9.

[163] D. Nam, J.U. Lee, H. Cheong, Excitation energy dependent Raman spectrum of MoSe2, Sci. Rep. 5 (2015) 1–6. doi:10.1038/srep17113.

[164] L. Seguin, M. Figlarz, R. Cavagnat, J.C. Lassègues, Infrared and Raman spectra of MoO3 molybdenum trioxides and MoO3 · xH2O molybdenum trioxide hydrates, Spectrochim. Acta Part A Mol. Biomol. Spectrosc. 51 (1995) 1323–1344. doi:10.1016/0584-8539(94)00247-9.

[165] M.R. Hilton, Fracture in MoS2 solid lubricant films, Surf. Coatings Technol. 68–69 (1994) 407–415. doi:10.1016/0257-8972(94)90194-5.

[166] M.R. Hilton, R. Bauer, P.D. Fleischauer, Tribological performance and deformation of sputter-deposited MoS2 solid lubricant films during sliding wear and indentation contact, Thin Solid Films. 188 (1990) 219–236. doi:10.1016/0040-6090(90)90285-L.

[167] G. Abadias, E. Chason, J. Keckes, M. Sebastiani, G.B. Thompson, E. Barthel, G.L. Doll, C.E. Murray, C.H. Stoessel, L. Martinu, Review Article: Stress in thin films and coatings: Current status, challenges, and prospects, J. Vac. Sci. Technol. A Vacuum, Surfaces, Film. 36 (2018) 20801. doi:10.1116/1.5011790.

[168] T. Polcar, M. Evaristo, M. Stueber, A. Cavaleiro, Mechanical and tribological properties of sputtered Mo–Se–C coatings, Wear. 266 (2009) 393–397. doi:10.1016/J.WEAR.2008.04.010.

[169] H.E. Sliney, Solid lubricant materials for high temperatures-a review, Tribol. Int. 15 (1982) 303–315. doi:10.1016/0301-679X(82)90089-5.